CAUSES AND CONSEQUENCES OF COUPLED CRYSTALLIZATION AND VESICULATION IN ASCENDING MAFIC MAGMAS

By

Amanda N. Lindoo, B.A.

A Dissertation Submitted in Partial Fulfillment of the Requirements

for the Degree of

Doctor of Philosophy

in

Geology

University of Alaska Fairbanks

August 2017

APPROVED:
  Jessica F. Larsen, Committee Chair
  Jeffery Freymueller, Committee member
  Pavel Izbekov, Committee member
  Tom Trainor, Committee member
  Paul McCarthy, Chair
    Department of Geosciences
  Paul Layer, Dean
    College of Natural Science and Mathematics
  Michael Castellini, *Dean of the Graduate School*

Abstract

Transitions in eruptive style and eruption intensity in mafic magmas are poorly understood. While silicic systems are the most researched and publicized due to their explosive character, mafic volcanoes remain the dominant form of volcanism on the earth. Eruptions are typically effusive, but changes in flow behavior can result in explosive, ash generating episodes. The efficiency of volatiles to degas from an ascending magma greatly influences eruption style. It is well known that volatile exsolution in magmas is a primary driving force for volcanic eruptions, however the roles vesicles and syn-eruptive crystallization play in eruption dynamics are poorly understood. Permeability development, which occurs when gas bubbles within a rising magma form connected pathways, has been suspected to influence eruption style and intensity. Numerous investigations on natural eruptive products, experimental samples, and analog experiments have extended the understanding of permeability development and fragmentation processes. However, these studies have focused on silicic, high viscosity, crystal-poor magmas. Little progress has been made in understanding fragmentation mechanisms in mafic or alkalic magmas. Mafic systems involve lower viscosity magmas that often form small crystals, also known as microlites, during ascent. Because the merging of bubbles in magma is mitigated by melt viscosity, it is predicted that permeability development in mafic magma will occur at lower bubble volume fractions than in silicic magma. However, no study has been performed on experimental samples to provide evidence for this hypothesis. Furthermore, it is unknown how microlites affect the degassing process in terms of facilitating or hindering permeability development. This thesis employs experimental petrology to: 1) experimentally observe how melt viscosity alone affects permeability development, 2) Understand the effects of syn-eruptive crystallization in vesiculating mafic magmas and synergizes these results to 3) relate experimental findings to the 2008 eruption of Kasatochi volcano.

Dedication

"If I have seen further, it is by standing on the shoulders of giants."

-Isaac Newton

A small part of me always knew I would live in Alaska at some point in my life. What I didn't know was how much I would learn about myself. Many people have supported and encouraged me over the past (almost) five years. This dedication would go on forever if I named everyone and how they impacted my journey. Assuming most of them won't read this, I will name only a special few.

First and foremost, I thank my advisor, Jessica Larsen, for accepting me as a Ph.D. student. Thank you for your patience, your enthusiasm, the pep talks, keeping me funded, sushi lab meetings, letting me play with your dogs, suggesting fantastic Belgian beers to try, and for sending me to Hawaii and Bristol, UK (twice)! I feel like I'll never be able to repay you for what you've done for me, but I know one way will be in published papers. Thank you for making a difference in my life.

Thank you, Mr. Schoen, my high school Earth Science, Astronomy, Natural Disasters, etc teacher. You supported my passion in science SO MUCH. Your additions of Astronomy and Natural Disasters to the high school curriculum helped me understand my niche in science – in that I should definitely stick with rocks and minerals!

Thank you Dr. Gramsch, my Research Experience for Undergraduates Advisor. You made me feel like I could be the best research scientist in the world if I put my mind to it. Carnegie was (is) a magical place. I never felt so confident and proud of myself in my life. I may have never gone to graduate school, if I had not been accepted into the REU. But it wasn't just the amazing program you oversaw; it was having you as my advisor that made all the difference. I'm so thankful for the opportunity, your generosity, your continued unwavering support and our AGU post-meeting babblings at the Irish pub.

Table of Contents

x

List of Figures

Chapter 2 An experimental study of permeability development as a function of crystal-free melt viscosity

Chapter 3 Crystal-controls on permeability development and degassing in basaltic andesite magma

Chapter 4 The influence of microlites and phenocrysts on eruption dynamics of the 2008 eruption of Kasatochi Island Volcano, Aleutian Islands, AK

List of Tables

List of Appendices

Chapter 1 Introduction

Transitions in eruptive style of mafic magmas are poorly understood. While silicic systems are the most researched and publicized due to their explosive character, mafic volcanoes remain the dominant form of volcanism on the earth. Mafic volcanoes display a wide range of eruption styles. Eruptions are typically effusive, but changes in flow dynamics can result in explosive, ash generating episodes (Houghton and Gonnermann, 2008). The efficiency of volatiles to degas from an ascending magma greatly influences this process. There are multiple ways magma can degas during ascent; examples being via permeable wall rocks, viscous shear along conduit walls, and/or through development of a permeable foam (Eichelberger et al., 1986; Jaupart, 1996; Gonnermann and Manga, 2007). This thesis focuses on the last mechanism, as few experimental studies have constrained what conditions lead to permeability development – especially in regard to mafic magmas.

It is well known that exsolution and expansion of gases from magma drives volcanic eruptions. Magmas are invariably rich in volatile species such as H_2O, CO_2, and SO_2. Water is commonly the most abundant volatile constituent with its solubility in the magma a function of pressure, temperature, and melt composition. As magma rises, volatiles become saturated in the melt due to decreasing solubility as a function of decreasing pressure. Gas exsolves and bubble nucleation, growth, and coalescence play a substantial role in magma ascent up the volcanic conduit. Individual bubbles may rise through the magma or interact with neighbors forming connected pathways that allow wholesale gas escape (permeability). The critical porosity at which permeability development occurs is defined as the percolation threshold. It has been suspected that differences in percolation threshold development may relate to overall eruption intensity and transitions in eruption style, e.g. strombolian to violent strombolian activity (Rust and Cashman, 2004; Pioli et al., 2008; Pioli et al., 2009; Rust and Cashman, 2011). Because the merging of bubbles in magma is mitigated by melt viscosity, the hypothesis stood that permeability development in mafic magma should occur at lower vesicularities than in silicic magma. Syn-eruptive crystallization further complicates this process, as it is unknown the extent at which microlites inhibit or promote bubble nucleation and coalescence. Microlites, crystals less than 100 microns in length, nucleate due to decompression-induced volatile loss. Exsolution of volatiles from the melt increases the liquidus temperature and encourages growth of

anhydrous crystal phases such as feldspar. Because nucleation requires the accretion of ions to form and grow crystals, decompression-induced crystallization occurs more readily in mafic, low viscosity magmas as ions diffuse more readily through less polymerized melts. Microlites provide sites for bubbles to form during decompression, however, substantial groundmass crystallization on ascent may also impede bubble growth, coalescence, or bubble migration (Oppenheimer et al., 2015; Pistone et al., 2015).

Numerous investigations on natural eruptive products, experimental samples, and analog experiments have extended the understanding of permeability development and fragmentation processes (Eichelberger et al., 1986; Klug and Cashman, 1996; Saar and Manga, 1999; Klug et al., 2002; Rust and Cashman, 2004; Mueller et al., 2005; Namiki and Manga, 2008; Okumura et al., 2009; Takeuchi et al., 2009; Oppenheimer et al., 2015; Pistone et al., 2015; Spina et al., 2016). Most have focused on a power-law trend describing the evolution of vesicularity as a function of permeability (Gonnermann and Manga, 2007). Studies on silicic pumice show a range in the percolation threshold between 56 and 78 vol.%, whereas mafic scoria appear to develop permeability around 25 to 30 vol.% - hence the concern for a compositional control on the percolation threshold (Eichelberger et al., 1986; Saar and Manga, 1999; Rust and Cashman, 2004; Mueller et al., 2005; Namiki and Manga, 2008; Takeuchi et al., 2009). Considerable scatter is seen in the data, suggesting that vesicularity alone cannot account for variations in permeability. The spread is usually explained by changes in degassing pathway morphology, a product of the degassing process itself and post-fragmentation processes. However, few studies have directly measured the varying complexities of flow paths within eruptive materials (Le Pennec et al., 2001; Bernard et al., 2007; Wright et al., 2009).

Experimental constraints are essential in order to understand the overall trends seen in the natural data. This dissertation is composed of three main chapters reflecting an overarching goal to constrain mechanisms of degassing in mafic magmas. In order to understand these three-phase systems (melt, bubbles, and crystals), it was necessary to first observe how permeability developed in a melt-bubble mixture. Prior to this work, no study had experimentally determined how melt viscosity alone impacts the percolation threshold. High temperature, high pressure experiments were conducted using silicic and mafic natural materials, to ensure the experimental methods employed produced results similar to previous work. The results of this effort provide evidence that melt viscosity does not affect permeability development. Furthermore, novel

experiments that produced decompression-induced microlites confirmed that crystals are responsible for lowering the percolation threshold. To better understand how this affects overall eruption style, the results of these experiments were applied to eruption products of the Kasatochi 2008 eruption. The electrical properties of the natural samples were also measured to provide a direct assessment of degassing pathway geometries. Key insights made from experiments aided in understanding how high crystallinties (> 50 vol.%) complicated gas migration in the Kasatochi system likely leading to the pulsatory nature of the eruption.

Two of the three main chapters of this thesis have been published in geoscience journals. The author of this thesis was responsible for running experiments and preparing the samples for data analysis. The author conducted all data analyses and writing of each manuscript.

Chapter 2 An experimental study of permeability development as a function of crystal-free melt viscosity[1]

2.1 Abstract

Permeability development in magmas controls gas escape and, as a consequence, modulates eruptive activity. To date, there are few experimental controls on bubble growth and permeability development, particularly in low viscosity melts. To address this knowledge gap, we have run controlled decompression experiments on crystal-free rhyolite (76 wt.% SiO_2), rhyodacite (70 wt.% SiO_2), K-phonolite (55 wt.% SiO_2) and basaltic andesite (54 wt.% SiO_2) melts. This suite of experiments allows us to examine controls on the critical porosity at which vesiculating melts become permeable. As starting materials we used both fine powders and solid slabs of pumice, obsidian and annealed starting materials with viscosities of $\sim 10^2$ to $\sim 10^6$ Pa s. We saturated the experiments with water at 900°C (rhyolite, rhyodacite, and phonolite) and 1025°C (basaltic andesite) at 150 MPa for 2–72 hrs and decompressed samples isothermally to final pressures of 125 to 10 MPa at rates of 0.25–4.11 MPa s^{-1}. Sample porosity was calculated from reflected light images of polished charges and permeability was measured using a bench-top gas permeameter and application of the Forchheimer equation to estimate both viscous (k_1) and inertial (k_2) permeabilities. Degassing conditions were assessed by measuring dissolved water contents using micro-Fourier-Transform Infrared (μ-FTIR) techniques. All experiment charges are impermeable below a critical porosity ($\mathit{\Phi_c}$) that varies among melt compositions. For experiments decompressed at 0.25 MPa s^{-1}, we find the percolation threshold for rhyolite is 68.3 ± 2.2 vol. %; for rhyodacite is 77.3 ± 3.8 vol.%; and for K-phonolite is 75.6 ± 1.9 vol.%. Rhyolite decompressed at 3–4 MPa s^{-1} has a percolation threshold of 74 ± 1.8 vol.%. These results are similar to previous experiments on silicic melts and to high permeability thresholds inferred for silicic pumice. All basaltic andesite melts decompressed at 0.25 MPa s^{-1}, in contrast, have permeabilities below the detection limit ($\sim 10{-}15$ m^2), and a maximum porosity of 63 vol.%. Additionally, although the measured porosities of basaltic andesite experiments are $\sim 10{-}35$ vol.% lower than calculated equilibrium porosities, μ-FTIR analyses confirm the basaltic

andesite melts remained in equilibrium during degassing. We show that the low porosities and permeabilities are a consequence of short melt relaxation timescales during syn- and post-decompression degassing. Our results suggest that basaltic andesite melts reached Φ_c >63 vol.% and subsequently degassed; loss of internal bubble pressure caused the bubbles to shrink and their connecting apertures to seal before quench, closing the connected pathways between bubbles. Our results challenge the hypothesis that low viscosity melts have a permeability threshold of ~30 vol.%, and instead support the high permeability thresholds observed in analogue experiments on low viscosity materials. Importantly, however, these low viscosity melts are unable to maintain high porosities once the percolation threshold is exceeded because of rapid outgassing and collapse of the permeable network. We conclude, therefore, that melt viscosity has little effect on percolation threshold development, but does influence outgassing.

2.2 Introduction

Vesiculation of ascending magmas drives volcanic eruptions. The explosivity of an eruption is modulated by the physical state of the conduit (Jaupart, 1996) and the degassing efficiency of the magma, which may proceed either through permeable bubble networks (Rust and Cashman, 2004) or magma fracture along conduit walls (Gonnermann and Manga, 2007). In silicic melts, degassing via permeable networks has been studied through analysis of eruptive products and decompression experiments on natural and analog materials. However, few studies have attempted to quantify and describe permeability development in low viscosity melts, and no experimental studies have been conducted. To address this gap, we extend decompression experiments to mafic and alkalic compositions. By comparing these results with those of their silicic counterparts, we address the role of melt viscosity in modulating the degassing process.

Magmas become permeable via one or both of two processes: connection of bubbles via coalescence to form permeable networks (e.g., Wright et al., 2009) or magma fracture (Castro et al., 2012a). Here we focus on development of permeable bubble networks, which is more likely than magma fracture to facilitate wholesale magma degassing in the conduit. As magma ascends, decreasing pressure causes the melt to become supersaturated with H_2O (e.g., Stolper, 1982), which triggers bubble nucleation and growth via diffusion and expansion. Vesiculation and bubble expansion can generate high vesicularities (>70 vol.%) and form magmatic foams, as observed in natural pumice clasts (e.g., Klug and Cashman, 1996; Wright et al., 2009). Once the

magmatic foam expands sufficiently to allow bubbles to impinge on one another, melt films separating neighboring bubbles thin and rupture to form apertures between bubbles. Extensive coalescence can create a connected network of bubbles that acts as a passageway for volatiles to quickly exit the system. The vesicularity at which magma becomes permeable (critical porosity, Φ_c) is termed the percolation threshold (Blower, 2001).

Bubble coalescence is primarily controlled by melt viscosity. In order for neighboring bubbles to coalesce, the melt films separating them must rupture; this is assumed to occur at a critical thickness (Proussevitch et al., 1993; Castro et al., 2012b). The timescales required to thin or stretch interstitial melt-films are controlled by melt viscosity and surface tension (Rust and Cashman, 2011). For this reason, coalescence occurs much more readily in lower viscosity melts; therefore, it has been assumed that the onset of permeability in mafic melts occurs at a lower porosity than in silicic melts. Once degassing commences, bubbles may deform or shrink while still maintaining a permeable pathway. This results in a hysteresis effect where vesicularity decreases as a result of deformation and reduced overpressure, while connected bubble networks maintain streamlined passageways for permeable outgassing (Saar and Manga, 1999; Rust and Cashman, 2004; 2011). Effusive products typically exhibit this hysteresis effect (e.g. Mueller et al., 2008), implying they achieved permeability and degassed. The extent to which permeability networks are modified during explosive eruptions is unknown.

Previous work examining critical porosities in phenocryst- poor, natural and experimental silicic (rhyolite and rhyodacite) pumice suggest percolation thresholds between 56 and 78 vol.% (Eichelberger et al., 1986; Klug and Cashman, 1996; Takeuchi et al., 2009). Theoretical models based on packing geometry of spheres (Blower, 2001), in contrast, predict permeability at porosities ≥ 30 vol.%. These predictions appear to be supported by analysis of phenocryst-poor, basaltic scoriae (Saar and Manga, 1999), where measurements at high porosities were fit by a curve calculated using percolation theory (Blower, 2001). Crystal-poor melts in Hawaii, in contrast, commonly produce pyroclasts with vesicularities $\Phi_c \approx 70$ vol.% (Rust and Cashman, 2011); these data are more consistent with an analog study that found permeability development to be delayed until $\Phi_c \approx 70$ vol.% in low viscosity corn syrup (Namiki and Manga, 2008). This percolation threshold is significantly higher than the $\Phi_c \sim 30$ vol.% proposed by percolation theory and more in line with results for natural and experimental crystal-free, high viscosity, silicic melts. One possible explanation for this discrepancy lies in the high micro-crystallinity of

most analyzed scoria samples, and the potential role of crystals in reducing the percolation threshold (Rust and Cashman, 2011), although decompression experiments have yet to confirm this hypothesis (Okumura et al., 2012). Alternatively, the discrepancy between theoretical and observed percolation thresholds may reflect limitations in the models, which do not account for either bulk volume expansion or the time required to thin films that separate individual bubbles (Rust and Cashman, 2011). To better understand this problem, we use high pressure and temperature decompression experiments to constrain critical porosities in phenocryst-free melts. The experiments employ rhyolite, rhyodacite, K-rich phonolite, and basaltic andesite starting materials to observe bubble exsolution and permeability development over melt viscosities that vary over four orders of magnitude (10^2 to $10^{6.2}$ Pa s). The initial starting conditions approximate water-saturated, supra-liquidus magma that is stored at approximately 6km depth in the crust and ascends rapidly (~10 to 300 m s^{-1}). The resulting permeabilities are measured with a bench-top permeameter constructed for small experimental samples. We find that percolation thresholds are similar for all melt compositions, but that melt viscosity exerts a profound influence on degassing and subsequent permeability development. We use these results to explore the role of magma viscosity in controlling syn-eruptive degassing and consequences for eruption styles

2.3 Experimental and Analytical Methods

2.3.1 Experimental methods

Decompression experiments employed both continuous and step-wise decompression pathways. Sample materials included powders and solid slabs of glassy rhyolite, rhyodacite, K-rich phonolite, and basaltic andesite from (Table 2.1): rhyolite (Mono Craters, CA; 76.32 wt.% SiO_2), rhyodacite (Aniakchak; 70.57 wt.% SiO_2; Larsen, 2006), K-phonolite (79 AD Vesuvius; 55.41 wt.% SiO_2; Shea et al., 2010a), and basaltic andesite (Okmok; 54.82 wt.% SiO_2; Wong and Larsen, 2009). These melt compositions were selected to encompass a wide range of estimated melt viscosities, and because the phase equilibria are known from previous experiments.

Initially all experiments were conducted using powders from natural pumice (Aniakchak rhyodacite, 79 AD Vesuvius phonolite), obsidian (Mono Craters rhyolite), or twice fused glassy lava (Okmok vitreous basaltic andesite). Using finely ground powders allows the initial diffusion timescale to be short, alleviating hydrogen loss through the capsules in the Ar pressurized TZM/MHC runs. It also mitigates the potential for Fe-loss to the capsule. Because it is known

8

that powdered starting materials contain an inherited set of large "hydration" bubbles (Larsen and Gardner, 2000), a second set of experiments were run for the Mono Craters rhyolite and Okmok basaltic andesite compositions using solid slabs as the starting materials. These experiments allow us to correct for "hydration bubbles" in the powder samples (e.g., Gardner et al., 1999; Larsen and Gardner, 2000).

Experiments were conducted using TZM (titanium–zirconium– molybdenum alloy) and MHC (molybdenum–hafnium–carbide alloy) vessels pressurized with ultra-high purity Ar gas, with ~2.5 bars CH_4 added to mitigate H diffusion. The charges were compressed with the Ar–CH_4 mixture to an initial pressure of 150 MPa, lowered into a Deltech furnace and heated to 900 °C (rhyolite, rhyodacite, phonolite) or 1025 °C (basaltic andesite). Pressure was monitored using a Heise pressure gauge accurate to ±1MPa, according to the manufacturer specifications. Experimental capsules were held first at 150 MPa for 2 to 72 hrs, with the hold times determined by calculating water diffusivities as a function of the average powder grain sizes or slab dimensions, to ensure that the experimental melts were H_2O-saturated before decompression (see Appendix A). Samples were isothermally decompressed continuously or using step-wise pathways for rates between 0.25–6 MPa s^{-1}. Once final pressures of 125, 100, 75, 50, 35, 25, 15, or 10 MPa were reached (see Appendix A, Table A-1), the vessel was pulled from the furnace and inverted, dropping the capsule against the water–cooled jacket surrounding the pressure connection to quench within a few seconds.

2.3.2 Permeability measurement

Samples were extracted as whole, unbroken slugs from their capsules using a razor blade and wire cutters. The samples were then wrapped in high viscosity Crystalbond 509 to seal the outside surface, and then submerged in 30 mL cups filled with Hillquist epoxy. After curing overnight, the samples were separated from the plastic cups for cutting and polishing (after Takeuchi et al., 2008). Cross-sectional areas of the experiments were exposed by polishing down the top and bottom of the plugs until the surfaces were parallel and no thinner than 10× the largest bubble diameter (Blower, 2001).

A gas permeameter was built at University of Alaska Fairbanks following the design of Takeuchi et al. (2008) to measure permeabilities of small experimental samples (see Appendix A). The experimental samples were measured at a range of gas flow rates and upstream air

pressures to create a curve that could be fitted using a modified version of Darcy's Law, the Forchheimer equation, to solve for viscous (k_1) and inertial permeabilities (k_2; Rust and Cashman, 2004).

$$\frac{P_2^2 - P_1^2}{2P_0L} = \frac{\mu}{k_1}v + \frac{\rho}{k_2}v^2 \tag{2.1}$$

The Forchheimer equation is preferred for vesiculated silicic samples because it accounts for energy loss through inertial effects as flow rate increases (Rust and Cashman, 2004). The k_1 and k_2 permeabilities can be calculated from the data by fitting a second order polynomial to the calculated modified pressure gradient and gas volume flux derived from permeability measurements (e.g., Rust and Cashman, 2004; Takeuchi et al., 2008). Each experiment was measured three times over the full range of gas flow rates to determine reproducibility. These repeat measurements produced standard deviations that are typically 0.1 log units (k_1) and 0.27 log units (k_2). The fitting error of the second order polynomial for all samples was $R^2 \geq 0.998$ (see Appendix A, Fig. A-1).

2.3.3 Vesicularity

To determine total vesicularity, reflected light images were taken of sample cross-sections exposed for permeameter measurements. The photomicrographs were processed in Adobe Photoshop to be converted to binary images (see Appendix A). Errors in vesicularity were determined by averaging measurements obtained from multiple regions of interest and calculating the standard deviation about the mean. In samples comprising a single image, errors were determined by reprocessing and analyzing the same image three times. These images were then input into a Matlab-based program (FOAMs, Shea et al., 2010b), to quantify bubble size and number.

2.3.4 FTIR analyses

Dissolved water contents were measured using a Thermo Fisher Scientific 6700 Fourier Transform Infrared Spectrometer coupled with a continuum microscope with two MCT-A detectors, one standard and one 50 μm for higher resolution analyses from smaller apertures (see

Appendix A). A purge collar was used to minimize the interference of atmospheric water and CO_2 on the analyses. Samples were placed on a NaCl disk for transmission analyses. Analyses were acquired over a wavenumber range of $\tilde{\nu}$ = 6500 - 650 cm^{-1} with the aperture set to 20 x 20 μm. Background spectra were collected before each analysis through the NaCl disk adjacent to the sample. Water concentrations were measured from 3 to 4 spots on each sample, with each spectra consisting of 512 scans at a resolution of 4 cm^{-1}.

2.4 Results

2.4.1. Experimental porosities

All experiments yielded crystal-free, vesicular glasses. Large vesicles (72 to 280 μm in diameter) present at high final pressures (P$_f$=125 MPa) in the experiments employing powdered starting materials and quenched at high final pressures (P$_f$ =125 MPa) most likely represent hydration bubbles (e.g., Gardner et al., 1999; Larsen and Gardner, 2000). The porosities of all experimental series systematically increase as a function of decreasing final pressure (Fig. 2.1a).

Experimental porosities in runs that used rhyolitic or phonolitic powdered starting materials (see Appendix A, Table A-2.1) are consistently higher than equilibrium calculated from solubility curves (Moore et al., 1998) (Fig. 2.1b; Equation 2.2), and are probably the result of hydration bubbles. In contrast, experiments using basaltic andesite starting compositions, either powdered and solid slab, produce experimental porosities that are systematically less than predicted by equilibrium. The former can be explained by hydration bubbles that occur in experiments employing starting powders (e.g., Gardner et al., 1999); the latter indicate gas loss during decompression.

A comparison of calculated equilibrium porosities with measured porosities determined from photomicrographs as a function of final pressures (Fig. 2.1b) confirms the role of hydration bubbles, as determined using the analysis of Gardner et al. (1999):

$$\phi M = \left[\frac{\frac{\rho_m}{Z} \underline{V}_w (\omega_o - \omega_F)}{1 + (\frac{\rho_M}{Z} \underline{V}_w (\omega_o - \omega_F))} \right] \qquad (2.2)$$

11

where ρ_m is the melt density, Z is the molecular weight of water, V_w is the molar volume of water at final pressure, and ω_0 and ω_F the weight fractions of dissolved water at initial and final pressure, respectively.

2.4.2. Water concentrations in the experimental glasses

The extent to which degassing occurred at equilibrium can be determined using micro-FTIR transmission spectroscopy methods and predicted solubility curves (Fig. 2.2; Moore et al., 1998). The rhyolite glasses using powdered starting material decompressed step-wise at 0.25 MPa s^{-1} have water contents (H_2O_{tot}) ranging from 3.80 ± 0.03 to 2.34 ± 0.02 wt.% at $P_F = 75$ and 15 MPa, respectively (see Appendix A). Total water concentrations analyzed in the K-phonolite glasses from powdered starting materials range from 4.37 ± 0.05 wt.% to 2.41 ± 0.02 wt.% at $P_F = 150$ and 50 MPa, respectively. The basaltic andesite experimental glasses have H_2O_{tot} from 2.18 ± 0.18 wt.% to 1.18 ± 0.06 wt.% at $P_F = 45$ and 15 MPa final pressures. Rhyolite glasses from powdered starting material decompressed step-wise at 0.25 MPa s^{-1} in our experiments are H_2O oversaturated by 0.09 to 2wt.% water at $P_F = 75$ to 15. K-phonolite and basaltic andesite experimental glasses have H_2O concentrations that are in agreement with their respective solubility curves. Our rhyolite data are comparable to experiments by Gardner et al. (1999), who found that rhyolite glasses decompressed to $P_F = 140$ to 100 MPa at 0.25 MPa s^{-1} were enriched in H_2O_{tot} by 0.33 to 1 wt.% relative to the predicted solubility curve.

2.4.3. Experimental permeabilities

Permeabilities of all experiments are below the detection limit of our permeameter ($\sim 10^{-15}$ m^2) until they reach a critical porosity (Φ_c; Fig. 2.3) at which their permeabilities become measurable. The Darcian (viscous) permeability (k_1) of rhyolite melts decompressed continuously between 2.5 and 4.11 MPa s^{-1} becomes measurable at $\Phi_c = 74$ vol.%, while rhyolitic melts decompressed step-wise at 0.25 MPa s^{-1} become permeable at Φ_c between 65 - 80 vol.% porosity. Rhyodacite decompressed step-wise at 0.25 MPa s^{-1} is permeable at $\Phi_c \sim 64$ vol.% and K-phonolite decompressed step-wise at 0.25 MPa s^{-1} at 76 vol.%. In contrast, the basaltic andesite experiments decompressed continuously at 0.25 MPa s^{-1} remain below the permeameter detection limit to pressures as low as 10 MPa, with porosity = 63 vol.%.

Non-Darcian (inertial) permeability (k_2) of rhyolite melts decompressed continuously between 2.5 and 4.11 MPa s^{-1} is measurable within a range of 74-78 vol.% porosity (Fig. 2.4). Decompressed step-wise at 0.25 MPa s^{-1}, rhyolite inertial permeabilities increase between 61.5 and 83.2 vol.% porosity. Rhyodacite decompressed step-wise at the same rate reaches log k_2 = -7.79 (0.08) m at $\Phi_c \sim$ 60 vol.% porosity. K-phonolite decompressed step-wise at 0.25 MPa s^{-1} reaches log k_2 = -8.81 (0.01) m at ~76 vol.% porosity. Inertial permeabilities of basaltic andesite melts decompressed continuously are below the detection limit of the permeameter.

2.5 Discussion

2.5.1. Permeability development in rhyolite, rhyodacite and K-phonolite melts

The permeabilities of silicic samples measured in this investigation compare well with available data on rhyolite experimental melts from Takeuchi et al. (2009). Our experiments predict percolation thresholds that are generally consistent with, but slightly lower than the experimental studies of Takeuchi et al. (2009) and higher than those of Westrich and Eichelberger (1994). We found a marked increase in permeability at a critical porosity below which permeabilities were not detectable ($k_1 <$ log k_1=10^{-15} m^2). If the lowest porosity at which a sample becomes measurably permeable is taken as the percolation threshold, percolation thresholds for the various compositions and decompression patterns would be as follows: when decompressed at 0.25 MPa s^{-1} the percolation threshold for rhyolite is 68.3 ± 2.2 vol.%; for rhyodacite is 77.3 ± 3.8 vol.%; and for K-phonolite is 75.6 ± 1.9 vol.% (Fig. 2.3). Rhyolite decompressed at 3-4 MPa s^{-1} has a percolation threshold of 74 ± 1.8 vol.%.

Our percolation thresholds are lower than the 80 vol.% defined by Takeuchi et al. (2009). It is difficult to explain the modest yet statistically significant differences in percolation thresholds between the three studies, despite similar melt compositions. The most obvious difference is the decompression rate. Slower decompression rates leave more time for coalescence processes such as melt film thinning and rupture, the receding of bubble walls and widening of bubble apertures (Rust and Cashman, 2004; Burgisser and Gardner, 2004; Mueller et al., 2008; Okumura et al., 2009; Takeuchi et al., 2009; Kobayashi et al., 2010; Castro et al., 2012; Nguyen et al., 2013). Although it has been shown that the degree of bubble coalescence is dependent on decompression rate (e.g. Burgisser and Gardner, 2004), a rate dependence of permeability development has not yet been observed. Takeuchi et al. (2009) found no rate

dependence with decompression rates similar to those expected during effusive lava dome forming eruptions (0.002, 0.005 and 0.05 MPa s^{-1}). Thus, we cannot explain the differences in percolation thresholds between the studies by decompression rate alone. More data is needed to determine whether percolation threshold development is rate dependent, although the results of rhyolitic experiments imply it is a possibility.

The difference in percolation thresholds may be due to experimental methods. Although both Takeuchi et al. (2009) and this study use powdered starting materials, Takeuchi et al. (2009) held the samples for one day before decompression. Hydration bubbles were likely able to rise out of the sample during that time period (see section 2.4.3.). Although hydration bubbles do not appear to affect the percolation threshold, they will affect the bubble size distribution. Vesicle size distributions of the four melt compositions (Fig. 2.5a, b, c, d and e) illustrate the resulting vesicle size distributions when hydration bubbles form. Experiments from powdered starting material feature vesicle sizes that are generally greater than 18 μm diameter, while solid slab starting materials include vesicles below that threshold. The abundance of larger bubbles in the powdered experiments would have encouraged bubble-bubble interaction, resulting in permeability development at lower supersaturations than hydration bubble-free melts.

Recent efforts also examine sample permeability using lattice Boltzmann models on X-ray computed microtomography (XRCT) images (Bai et al., 2010; Polacci et al., 2012). Those studies indicate permeability development in experimentally decompressed melts occurs at porosities as low as 49 vol.% in rhyolites and 29 vol.% in basaltic melts (Bai et al., 2010; Martel and Iacono-Marziano, 2015). The calculated permeabilities are consistently higher for a given porosity than from direct measurements on bulk samples using a permeameter. Although XRCT allows 3D visualization of the internal structure of natural and experimental products, thin bubble walls (≤1 micron, Klug et al., 2002) cannot be resolved due to constraints on voxel resolution (cubic voxel edge length ~1.85-9 μm) (Bai et al., 2010; Polacci et al., 2012). Consequently, bubble walls that are thinner than the image resolution appear to be connected in the XRCT images and are treated as pore apertures in lattice Boltzmann calculations. This results in calculated permeability measurements up to an order of magnitude higher or lower than measured permeabilities (Wright et al., 2006; Bai et al., 2010; Polacci et al., 2012). Therefore, although the method is difficult and requires extremely careful handling of the fragile experimental samples, direct measurements of permeability on experimental charges is possibly

more accurate because it captures permeability resulting from all pore apertures, regardless of bubble wall thicknesses.

We also observed a decrease in porosity with increasing permeability in our rhyolite experimental samples. We interpret this observation to reflect the degassing process. Once an aperture has formed between two coalescing bubbles, overpressure within the bubbles decreases (Kobayashi et al., 2010; Namiki and Kagoshima, 2014). The pressure loss within a bubble due to aperture formation can be approximated as (Kobayashi et al., 2010; Namiki and Manga, 2014):

$$p = p_o \exp\left[\frac{\pi P_a r_o^2}{\rho_g c_g V}\frac{\eta e}{2\sigma}\left\{1 - \exp\left(\frac{2t\sigma}{\eta e}\right)\right\}\right] \tag{2.3}$$

where p_o is the internal bubble pressure estimated using the Rayleigh-Plesset equation (Sparks, 1978), P_a is atmospheric pressure (10^5 Pa), r is the initial aperture radius, η and σ are the viscosity and surface tension of the melt. To model bubble pressure loss, the film thickness (e) was calculated using the relationship found by Namiki and Kagoshima (2014), such that $e \propto \eta^{-0.62}$. We used values determined by Kobayashi et al. (2010) for a supercritical gas of density (ρ_g) 0.16 kg m^{-3} and sound velocity (c_g) of 870 m s^{-1}. We found aperture growth is slower in high viscosity magma for bubbles of 25 μm and 0.1 m radii within rhyolite ($\eta = 10^{5.5}$ Pa s, $\eta = 0.11$ N m^{-1}), phonolite ($\eta = 10^{4.3}$ Pa s, $\sigma = 0.063$ N m^{-1}), and basaltic andesite ($\eta = 10^2$ Pa s, $\sigma = 0.09$ N m^{-1}) melt at approximately 800 m depth; therefore a longer time is required to relieve overpressure. As pressure decreases in the bubble, the aperture retracts until tensional force is lost due to pressure release (Kobayashi et al., 2010). Depending on the stability of the bubbly melt, gas loss may result in melt deformation and some degree of bubble shrinkage (Burgisser and Gardner, 2004; Mongrain et al., 2008). Alternatively, external pressure acting on the melt may cause bubbles to be partially or completely resorbed (Eichelberger et al., 1986; Martel and Iacono-Marziano, 2015) It is likely that the relatively higher external pressure of the melt would have influenced the porosities of this study had we allowed a longer holding time at final quench pressures. However, samples were quenched approximately 15 seconds after final pressures were reached. This short hold time and fast quench time (~2.2 s) would not have allowed bubbles in the silicic experiments to relax, with the exception of the basaltic andesite melts. Therefore, the permeable network achieved in the silicic melts would have persisted until quench.

2.5.2. Degassing in rhyolite, rhyodacite and K-phonolite melts

We found it important to confirm the degassing histories of the silicic experiments using FTIR methods, because the presence of hydration bubbles affected the interpretation of porosity measurements. All of the rhyolitic samples are supersaturated, which indicates disequilibrium degassing (Fig. 2.2). Oversaturation is not unusual for rhyolitic melts, as it is difficult for silica-rich melts to degas efficiently at fast decompression rates (>0.25 MPa s^{-1}; Gardner et al., 1999; Burgisser and Gardner, 2004). Gardner et al. (1999) also observed disequilibrium degassing in rhyolite samples at the same decompression rate (0.25 MPa s^{-1}), however the degree of that we measure is generally lower. This may be due to the higher experimental temperature employed in our study (900°C vs. 825°C), which should enhance water diffusivity and lower melt viscosity. The rhyodacite and K-phonolite samples, however, are in good agreement with equilibrium solubilities. Previous studies by Larsen and Gardner (2000) and Mongrain et al. (2008) also concluded that K-phonolite could degas efficiently even at high decompression rates (0.25 MPa s^{-1}).

2.5.3. Degassing in basaltic andesite melts

By comparison with the silicic samples, basaltic andesite samples from both powdered and solid slab experiments behave very differently during decompression. Although they vesiculate and achieve a porosity of 63 vol.% at final pressures of 10 MPa, none of the basaltic andesite samples had measurable permeabilities (Fig. 2.3). In order to understand the cause of the apparent impermeability, it is important to note that the basaltic andesite porosities are systematically lower than predicted for equilibrium exsolution using equation 2.2. We consider three possible explanations for the low porosities, which will be addressed throughout the remainder of this section: 1) disequilibrium exsolution 2) bubble rise out of the sample during decompression or 3) development of permeable pathways leading to melt degassing, porosity reduction, and rapid re-annealing of pore throats between connected bubbles due to fast melt relaxation timescales.

Disequilibrium H_2O exsolution, as observed in rhyolites (e.g., Gardner et al., 1999), is unlikely in basaltic andesite melts, as water can diffuse 30 to 50 times faster than in rhyolites (Zhang, 1999). Indeed, the micro-FTIR data plotted in Figure 2.2 show the quenched basaltic andesite glasses from our decompression experiments have dissolved water concentrations that

agree very well with the solubility curve calculated using the model of Moore et al. (1998). This rules out disequilibrium exsolution as the explanation for the systematically low porosities and lack of permeability development.

Because the basaltic andesite melts have calculated melt viscosities of 10^2 to 10^3 Pa s, compared with $10^{4.2}$ to $10^{6.2}$ Pa s for the rhyolite melts, it is possible that the low porosities could be the result of bubble rise out of the sample into the capsule headspace. We tested this hypothesis by determining the rise velocity (v) for a spherical bubble using Stokes Law:

$$v = \frac{2}{9\eta} (r^2 g(\rho_b - \rho_m)) \qquad (2.4)$$

where η is the viscosity of the melt, r is the bubble radius, g is the gravitational constant, ρ_b and ρ_m are the densities of the gas and melt, respectively. At 900°C and 150 MPa, the estimated water content of Okmok basaltic andesite is 4.36 wt. % (Moore et al., 1998), and the melt viscosity under these conditions is 10^2 Pa s according to the model of Giordano et al. (2008). For a melt density of 2650 kg m^{-3} and an average bubble radius of 24 μm, equation 2.4 predicts a bubble rise rate of 1.67 x 10^{-5} mm/s. During decompression, even as the bubbles grow larger, this rate would have slowed as the melt became more viscous during water exsolution (Fig. 2.6). Given that the average length of the experimental charges is 10 mm and the longest decompression timescale is 9.5 minutes, this suggests that small bubbles would not be able to escape from the melt. However, some hydration bubbles ($r \approx 50 \ \mu m$) would have been able to rise out (~0.5 mm/hr) of the melt during the average initial holding time of 2.25 hrs (8100 s). Bubble loss to the headspace at the top of the capsule would explain why using a powdered starting material for basaltic andesite runs does not inflate the measured porosity. In contrast, bubble rise in our silicic experiments is negligible. For example, a bubble 24 μm in diameter in a rhyolite melt with log η (Pa s) of 4.16 and density of 2300 kg m^{-3} has a rise velocity of 1.83x10^{-7} mm/s. We conclude that the resulting porosities in all experiments, even the low viscosity basaltic andesite runs, were not affected by bubble rise during decompression except for possible loss of hydration bubbles from the more mafic melts (Fig. 2.6).

Our preferred hypothesis to explain the lower than equilibrium porosities and apparent lack of permeability development in the basaltic andesites is syn- and post-decompression

degassing. Even though we employed rapid quench methods and expect the sample cooled within a few seconds at most to the glass transition temperature (Gardner et al., 1999), the short melt relaxation timescales facilitated melt drainage into, or collapse of, the bubble walls that could have re-sealed pore throats resulting in lower observed porosities and permeabilities. We can test this hypothesis by calculating the melt relaxation timescale of our basaltic andesite melt and compare it to the quench time. The timescale for a bubble to return to a relaxed, spherical shape can be calculated after Toramaru (1988):

$$\tau_r \approx \eta a / \sigma \tag{2.5}$$

where η is the melt viscosity, a is the bubble radius and σ is the surface tension. Using the calculated viscosity (10^3) of basaltic andesite at the lowest final pressure (15 MPa) and a surface tension of 0.09 N m^{-1} (Khitarov et al., 1979), we find a relaxation timescale is 0.3 seconds for a bubble with a radius of 30 μm (Fig. 2.6). Therefore, the relaxation timescale is much faster than the cooling time of the quenched charge (~2.2 – 6.5 s; Gardner et al., 1999; Giordano et al., 2008; Castro et al., 2012). Because water content decreases melt viscosity, relaxation would occur faster at higher final pressures (e.g. 125 MPa) when more water resides in the melt (Fig. 2.6). The surface tension of basaltic andesite is not well constrained, but increasing surface tension only shortens the resulting timescale. For example, using the value of 0.25 N m^{-1} (Murase and McBirney, 1973) reduces the relaxation timescale to 0.1 seconds. Therefore, it is difficult to preserve the structure of the basaltic andesite samples as they vesiculate during decompression, without significant modifications in the very short timescale between decompression and quenching. We conclude that it is likely our experiments did achieve permeability during decompression, but given limitations inherent to the cold-seal hydrothermal experimental apparatus and design, it is very difficult to constrain the percolation threshold in mafic melts. The issues encountered with the basaltic andesite experiments as described above make it difficult to directly compare with the silicic experiments (Fig. 2.3).

The simplest explanation for the observed lack of measurable permeability is that the samples became permeable, degassed, and then relaxed to a less porous and impermeable state before quenching. For samples decompressed to 10 MPa, this requires that the percolation threshold was reached at a vesicularity greater than 63 vol.%. This suggests that the basaltic

andesite melts also required high porosities for permeability to develop. Once permeability is achieved, however, they are able to outgas much more quickly than high viscosity melts. Film rupture timescales provide the greatest control on this process, as inter-bubble melt films (IBFs) must rupture to form an aperture through which gas can move. This can occur via mechanisms such as capillary drainage, stretching via expansion, or dimpling (Castro et al., 2012). We have calculated the time (τ_f) required for melt to drain from an initial thickness (δ_f) to a critical thickness (δ_{cr}) from the binary coalescence model of Proussevitch et al. (1993):

$$\tau_f = \frac{3\eta R^3}{4\sigma}\left(\frac{1}{\delta_{cr}^2} - \frac{1}{\delta_f^2}\right) \tag{2.6}$$

We use our experimental viscosity range of 10^2–$10^{6.2}$ Pas, surface tensions defined above, an initial thickness of 10 μm and critical rupture thicknesses between 0.1–1 μm (Klug et al., 2002; Castro et al., 2012). The uncertainty linked with initial and critical thicknesses results in the large range of thinning timescales (Fig. 6). We obtain similar timescales as reported in Castro et al. (2012) in that low viscosity melts (10^2 Pa s) will thin to critical thicknesses within 100 s. As seen in Fig. 2.6, the basaltic andesite melts could have coalesced via melt-film drainage over the course of the decompression time (570 s). However, IBFs in high viscosity melts take orders of magnitude longer to thin (10^3–10^7 s). The K-phonolite, rhyodacite, and rhyolite melts would not be able to coalesce by melt-film thinning alone, but instead would require faster film rupture mechanisms, such as IBF stretching due to bubble growth or dimpling (Castro et al., 2012). A percolation threshold in excess of 63 vol.% for the low viscosity melts is consistent with the percolation threshold >65 vol.% observed by Namiki and Manga (2008) for low viscosity analog materials. The evidence we have discussed in the following section demonstrates that it is likely our experiments achieved permeability during decompression, but given limitations inherent to the cold-seal hydrothermal experimental apparatus and design, it is very difficult to constrain the percolation threshold in mafic melts, and make it difficult to compare the results directly with the silicic experiments (Fig. 2.3).

2.5.4. Melt viscosity and its control on percolation threshold

To assess the control of melt viscosity on permeability development, we calculated viscosities of the silicic experimental melts at the determined percolation thresholds. We determined the melt viscosities of rhyolite, rhyodacite, and k-phonolite to be $10^{5.5}$, 10^5, and $10^{4.6}$ at critical porosities of 68.3 (2.2), 77.3 (0.4) and 75.6 (1.9) vol.%, respectively. As described above, the basaltic andesite samples likely became permeable at porosities greater than 63 vol.% at viscosity of about 10^3 Pa s (Fig. 2.8). If we interpret 63 vol.% as a lower bound for permeability development, our data suggests melt viscosity does not greatly influence the percolation threshold.

The consistency in percolation thresholds of high viscosity melts implies large vesicularities are required in order for silicic, crystal-free systems to become permeable. However, our findings also suggest low viscosity melts may also call for similar porosities for permeability development. Although the fast melt relaxation timescales we observed in our experiments hindered our ability to capture the percolation threshold, our results in combination with those from analog material (~70 vol.%, Namiki and Manga, 2008) support this hypothesis. In crystal-free melts, permeability development is dependent on bubble coalescence (Blower, 2001). In order for coalescence to occur enough bubbles must exist in the melt to "see" and do mechanical work on each other resulting in interstitial melt thinning to the point of rupture. Because the drainage time is a function of melt viscosity, aperture formation, and thus outgassing rates will be delayed in high viscosity melts (Proussevitch et al., 1993; Gonnermann and Manga, 2007; Nguyen et al., 2013). In rhyolites, the slower aperture growth velocity and the longer timescale required to reduce overpressure in high viscosity melts effectively hinders permeability development and outgassing (Kobayashi et al., 2010; Namiki and Kagoshima, 2014). Although mafic melts may require high vesicularities for degassing to commence, they are not bound by the same kinetic limitations as silicic melts. Consequently, they are able to relieve overpressure more rapidly, as demonstrated by the experiments.

2.5.5 Potential effects of viscosity on eruptive style

In silicic magma, where bubble nucleation, growth and coalescence is often delayed (e.g., Mangan and Sisson, 2000), the vesicularity needed for permeability development may not be achieved until the magma reaches shallow depths. For this reason, degassing efficiency is

strongly controlled by the timescales of decompression (Martel and Iacono-Marziano, 2015). Rhyolite magmas ascending at the fast rates studied here would not outgas fast enough to relieve overpressure, and therefore would culminate in an explosive eruption. Bubble coalescence is expected to be faster in lower viscosity melts. Our experiments support this: although high vesicularities are required for permeability to develop, the mafic melts outgas rapidly, followed by collapse of the permeable networks. This hysteresis effect, where vesicularity decreases during outgassing, is typically observed in effusive products (e.g., Rust and Cashman, 2004; Mueller et al., 2008). Our experiments show that, in contrast, mafic magmas could experience this effect even with the fast ascent that characterizes explosive eruptions.

This raises a final question, which relates to controls on magma explosivity. The decompression rates employed here are rapid, and faster than inferred for most conditions of magma ascent, and reflecting instead conditions achieved by rapid downward-propagating decompression waves. Efficient syn-decompression degassing under these conditions underlines the difficulty in generating explosive eruptions from low viscosity and low crystallinity magma. One suggested mechanism of retaining gas pressure in mafic melts is to increase the viscosity by microlite crystallization driven by degassing during magma ascent (e.g., Houghton and Gonnermann, 2008). Importantly, this mechanism requires both gas exsolution from the melt and then sufficient time for crystals to nucleate and grow. Our experiments support those of Szramek et al. (2006) and observations of Wright et al. (2012), which suggest that decompression-driven crystallization of water-saturated basaltic andesite requires decompression rates of <10 MPa/s. Interestingly, explosively erupted mafic samples with high crystallinities commonly also have low preserved vesicularities (Pioli et al., 2008; Vinkler et al., 2012). These observations support our interpretation of the degassing efficiency of mafic magma, as well as the role of ΔP (difference between magma pressure and the surface) in driving explosive mafic eruptions (Cashman and Giordano, 2014).

2.6 Summary

This study constrains the onset of permeability development in crystal-free rhyolite, rhyodacite, K-phonolite, and basaltic andesite melts using high pressure and temperature, isothermal decompression experiments. Bubbles in rhyolite, rhyodacite, and K-phonolite melts underwent extensive coalescence culminating in permeability development at vesicularities of

~70–75 vol.%. Internal pressures within bubbles are subsequently reduced following gas loss, which causes porosities to decrease slightly, although permeability is still maintained. Quenched silicic experimental products record viscous permeability values similar to previous experimental studies of silicic melts (e.g., Takeuchi et al., 2009) and measurements of silicic pumice (Klug and Cashman, 1996; Rust and Cashman, 2011).

Basaltic andesite samples are not measurably permeable but show evidence of melt degassing, in that measured water contents agree with calculated water solubility but measured porosities are consistently lower than calculated equilibrium values. Stokes velocities negate the possibility of degassing via bubble rise over the short experimental timescale. Therefore we assume the basaltic andesite melts degassed. Estimated film rupture timescales are shorter than experimental timescales, which shows that degassing of the basaltic melts is possible. The degassing resulted in porosity reduction and closure of bubble apertures, which consequently sealed off degassing pathways and substantially reduced permeability. Although we cannot constrain the percolation threshold for basaltic andesite melts due to extremely fast melt relaxation times (<0.3 s at a viscosity less than 10^3 Pa s), we assume that the percolation threshold is higher than the maximum porosity measured (63 vol.%).

The similarity between silicic and mafic percolation thresholds observed experimentally in this study indicates melt viscosity has no effect on the percolation threshold. However, it is clear from our experiments that melt viscosity does influence outgassing behavior. Contrary to predictions, we do not see a significant increase in percolation threshold vesicularity between melt viscosities of 10^3 and $10^{4.6}$ Pa s. The coherence of silicic and mafic percolation thresholds (Fig. 7) implies that under conditions of rapid decompression, permeability can develop in crystal-free melts only at high melt vesicularities (>60 vol.%). Permeability at lower vesicularities in such magmas requires another (hysteretic) mechanism, such as the presence of crystals, magma shearing, micro-cracks, or post-fragmentation processes.

2.7 Figures

a.

b.
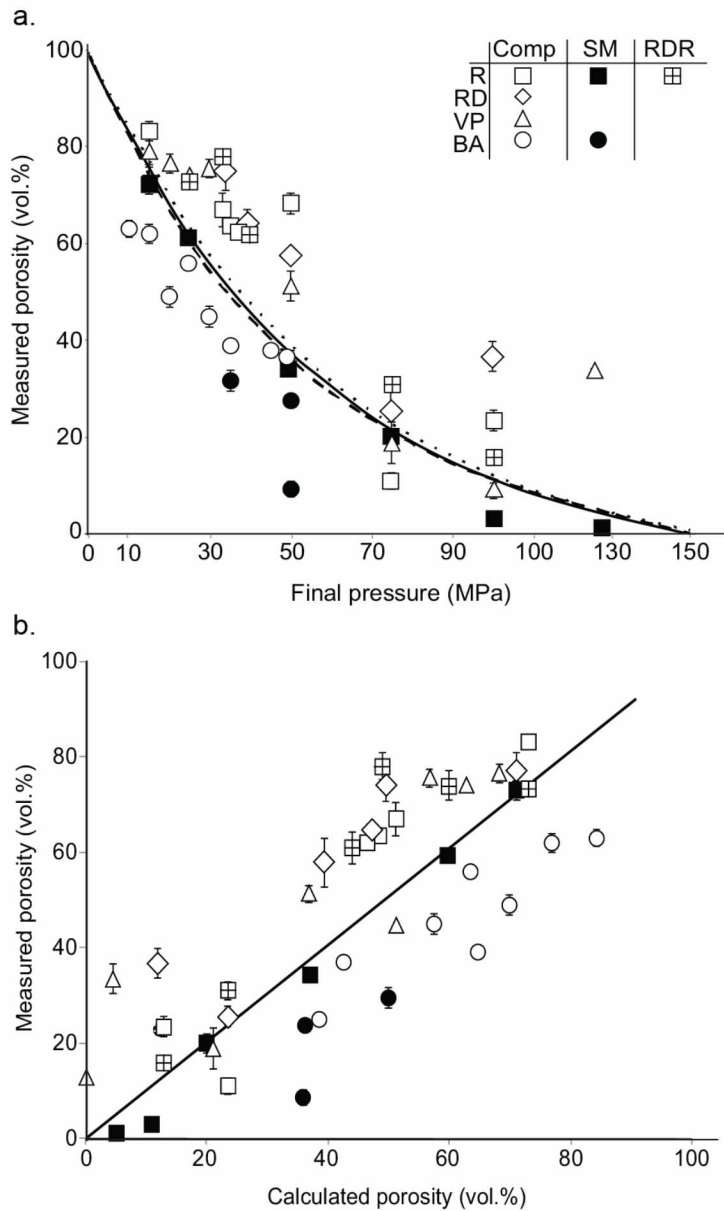
Figure 2.1a: Measured porosity as a function of final quench pressure. The dashed, solid, and dotted lines represent equilibrium rhyolite, K-phonolite, and basaltic andesite porosities. Legend: sample compositions (COMP) are denoted by open squares (rhyolite), diamonds (rhyodacite), triangles (K-phonolite) and circles (basaltic andesite). Samples using solid slab starting materials (SM) are indicated by filled in symbols. Rhyolite samples that underwent rapid decompression rates (RDR) are marked with an internal cross. Silicic samples with powdered starting material are in general in agreement or above calculated equilibrium porosities. Samples with solid slab (SS) starting material track calculated equilibrium porosities. Basaltic andesite samples using solid slab and powdered starting materials all have porosities lower than expected at equilibrium.
Figure 2.1b: A comparison of measured porosities determined from photomicrographs to

equilibrium porosities calculated using equation (2.2). Error bars denote standard deviation (σ) of replicate porosity measurements.
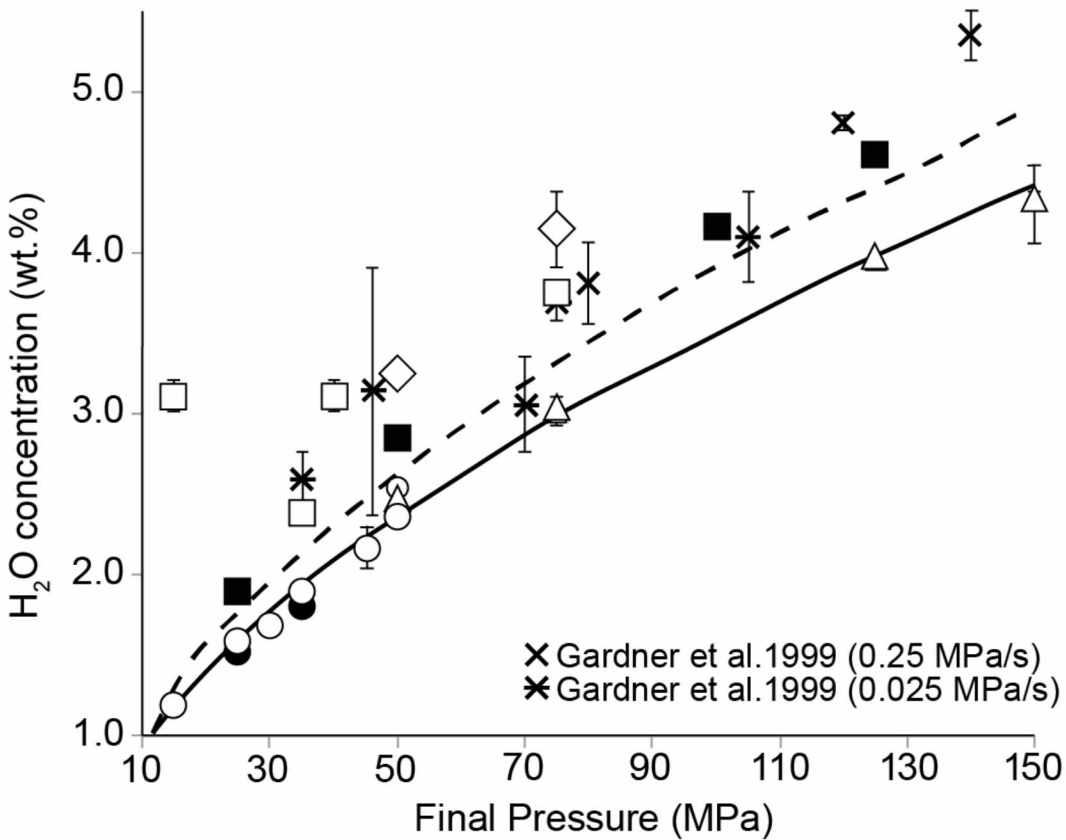
Figure 2.2: Total water content in experimental samples measured using FTIR. We use the same symbols as figure 1 with the exception of those represented in the legend. The dashed curve represents predicted equilibrium water concentrations for rhyolite and rhyodacite melt compositions (Moore et al., 1998). The solid line represents equilibrium water concentrations in K-phonolite and basaltic andesite melts (Moore et al., 1998). Rhyolite and rhyodacite water concentrations are typically similar to or above equilibrium concentrations, while K-phonolite and basaltic andesite melts show water concentrations in agreement with equilibrium. A previous study by Gardner et al. (1999) is plotted to compare water oversaturation seen in rhyolites decompressed at similar rates.
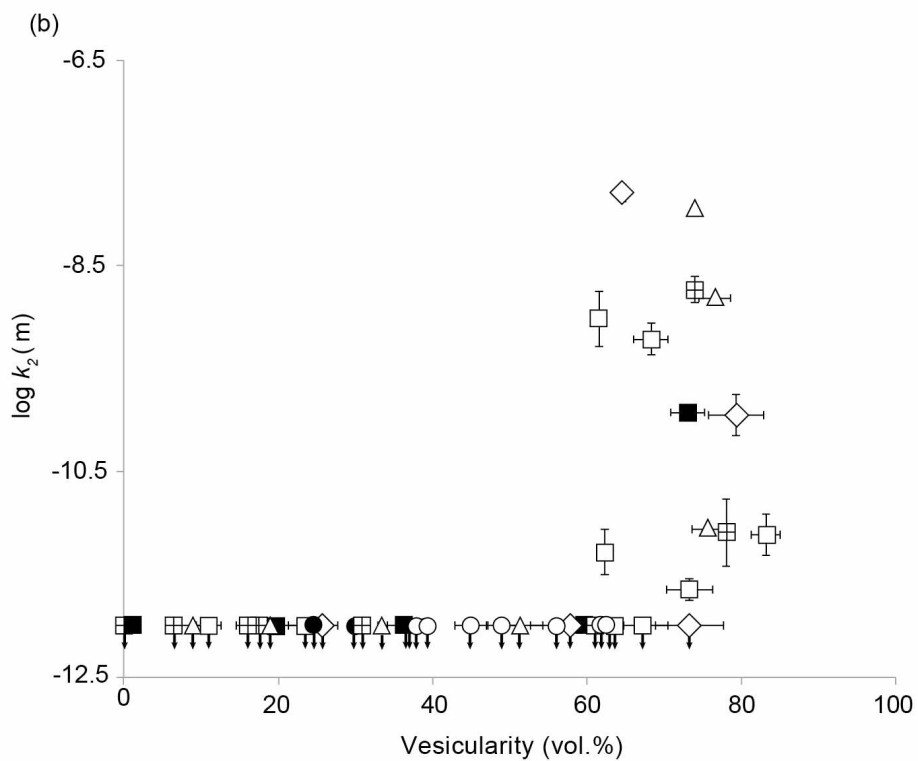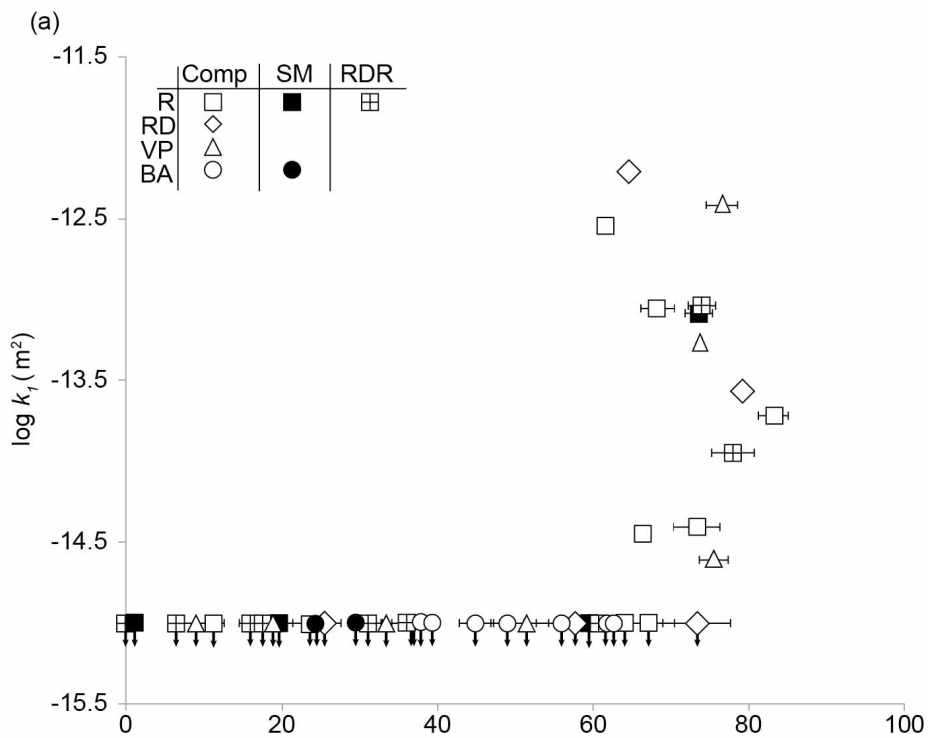
Figure 2.3a: Relationship between vesicularity and viscous (k_1) permeability. **Figure 2.3b:** Inertial permeability as a function of vesicularity. Symbols are the same as figures 1 and 2. Down arrows indicate the detection limit of the permeameter, therefore permeabilities are lower than the plotted values. Standard deviations are smaller than symbols unless otherwise noted.
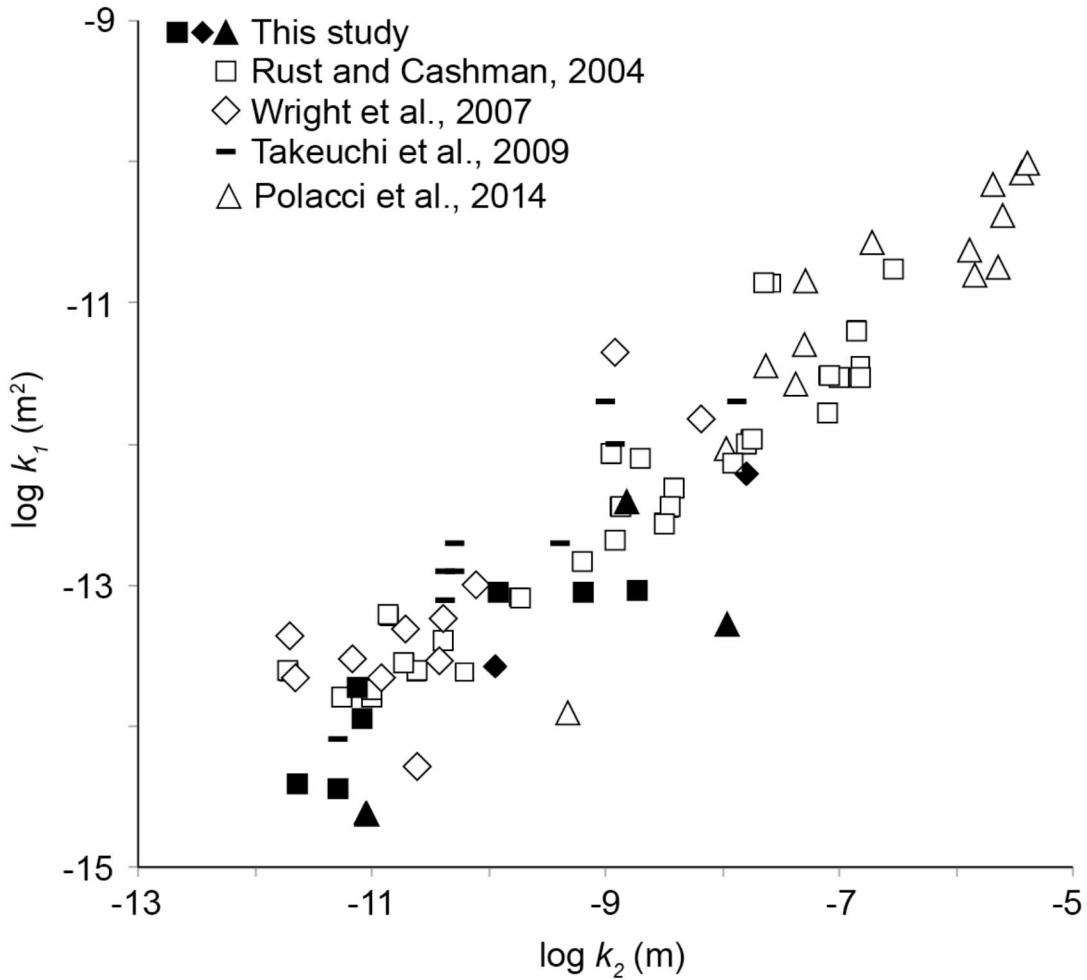
Figure 2.4: Viscous (k_1) vs. inertial permeability (k_2). The shapes of the symbols indicate sample composition following the labeling strategy as previous figures. This study as well as another experimental study, Takeuchi et al. (2009), are marked by black symbols. Studies on pumice are indicated with open or light gray symbols.
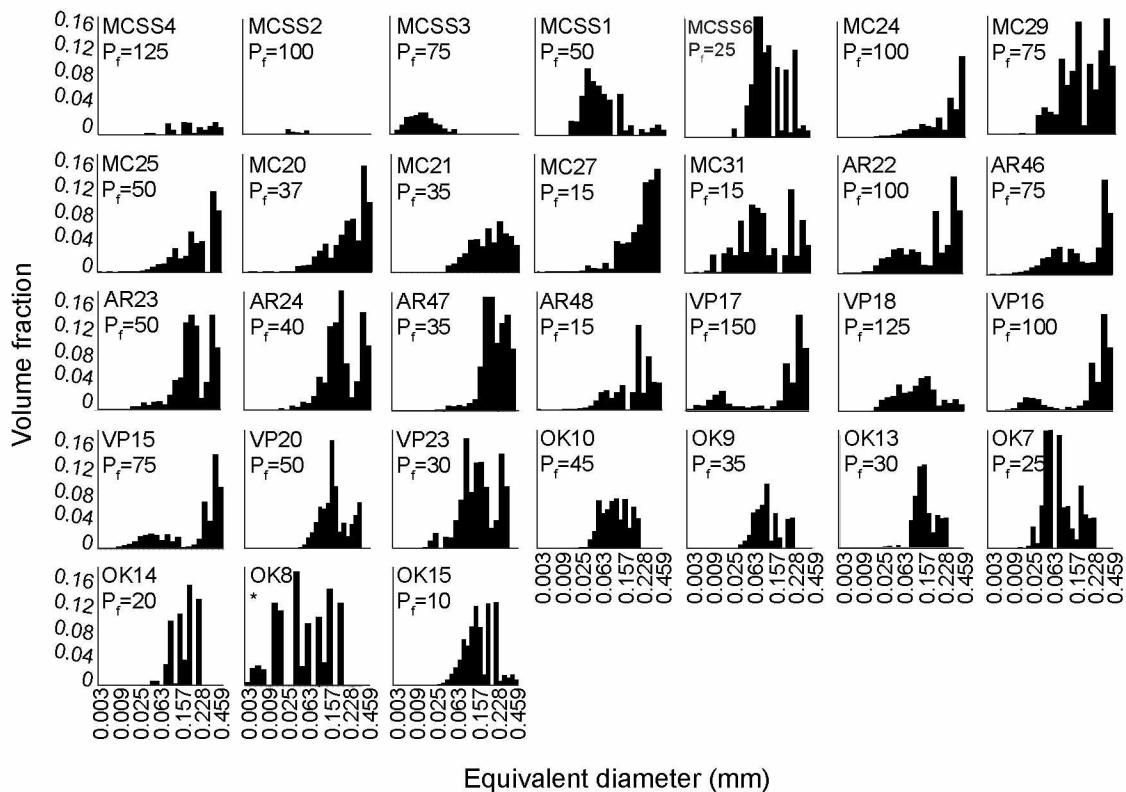
Figure 2.5: Bubble size distributions measured from rhyolite (MCSS and MC), rhyodacite (AR), K-phonolite (VP), and basaltic andesite (BA) samples. Volume fractions sum to vesicularity for each sample. * = 10 MPa.
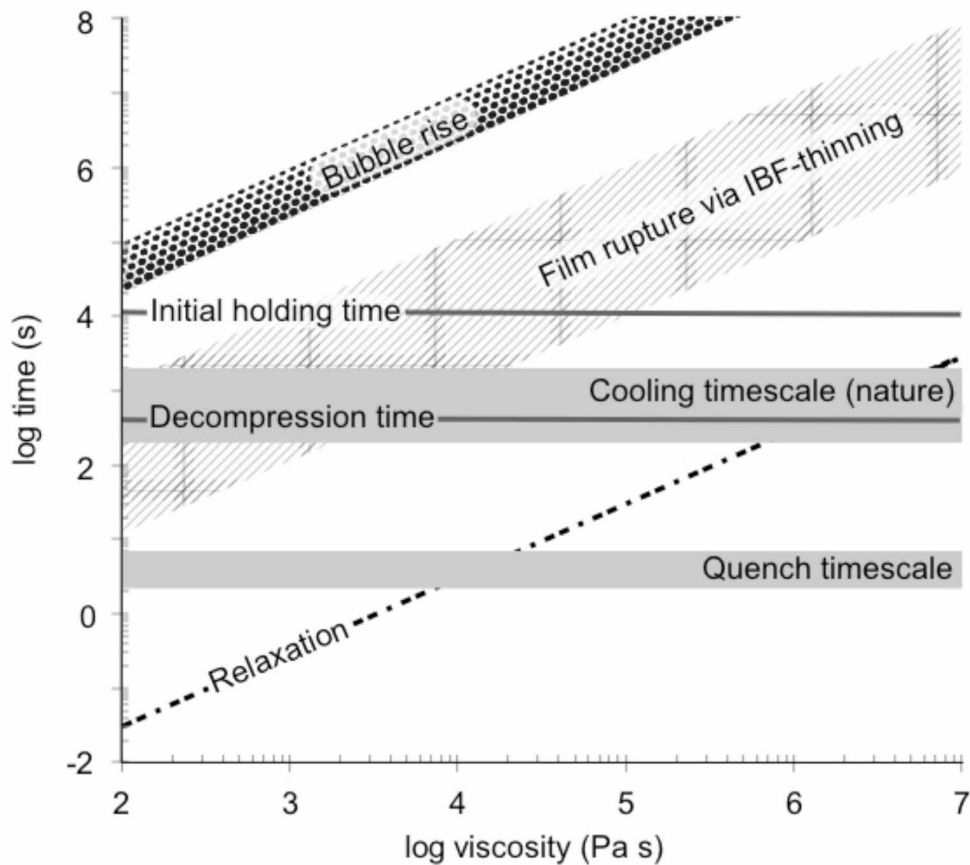
Figure 2.6: Compilation of possible factors influencing recorded vesicularities and permeabilities in our experiments including: bubble rise velocities, melt relaxation timescale, film rupture via film thinning, as well as quench and cooling timescales all as a function of melt viscosity. A range of bubble rise velocities was estimated using hydration and decompression bubble average radii (see Discussion section 2.4.3). The velocities were then used to approximate the amount of time required for a bubble to escape the upper 1/3 of the capsule. Film rupture timescales were calculated using different values for critical film thicknesses. The top gray bar represents the cooling timescale of natural pyroclasts (Szramek et al., 2010). The bottom gray bar represents the estimated quench timescale (2.2-6.5 s) of experiments. The initial holding time and maximum decompression time are marked with lines. Note the basaltic andesite relaxation timescale is faster than the quench timescale. Basaltic andesite, K-phonolite and rhyolite relaxation timescales are generally faster than natural cooling rates, with the exception of rhyolite melts at low final pressures (high melt viscosity).

28
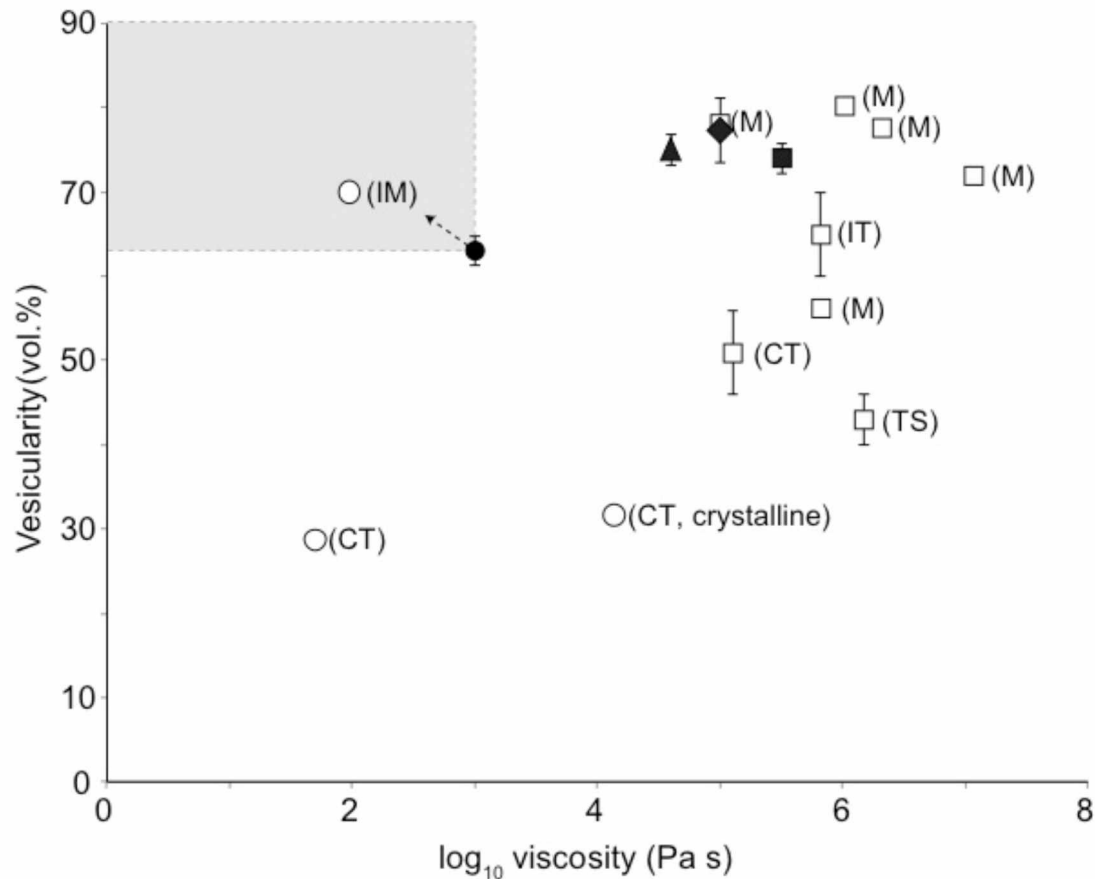
Figure 2.7: Comparison of percolation thresholds as a function of melt viscosity between this study (black square, diamond, triangle and circle corresponding to the same compositions as previous labels) and previous studies of permeability development in natural and experimental systems (open squares and circles based on composition)(Eichelberger et al., 1986; Westrich and Eichelberger, 1994; Klug and Cashman, 1996; Burgisser and Gardner, 2004; Namiki and Manga, 2008; Nakamura et al., 2008; Takeuchi et al., 2009, Bouvet de Maisonneuve et al., 2009; Bai et al., 2010, 2011; Martel and Iacono-Marziano, 2015) . Notes next to data points refer to how permeability was estimated (M = permeameter measurement, CT = X-ray Computed Tomography, TS = inferred from thin-section analysis, IT = inferred from isotopic tracer, IM = indirectly measured via density, mass and height measurements). Measured porosities of silicic systems group above 70 vol.% for high melt viscosities, while calculated or lattice Boltzmann simulations produce lower vesicularities for comparable viscosities. We predict the percolation threshold for crystal-free basaltic andesite lies within the shaded region.

2.8 Tables

Table 2.1: Major oxide compositions of starting materials

Oxide	MC[1]	AnRd[2]	VP[3]	OK52A[4]
SiO_2	76.32(0.29)	70.57	55.41(0.38)	54.82(0.51)
TiO_2	0.21(0.17)	0.53	0.26(0.11)	2.55(0.5)
Al_2O_3	13.02(0.06)	15.31	21.97(0.45)	14.49(0.2)
FeO*	1.03(0.08)	2.69	2.90(0.38)	11.03(0.23)
MnO	-	0.16	0.24(0.12)	0.18(0.06)
MgO	0.04(0.02)	0.61	0.65(0.07)	3.38(0.09)
CaO	0.53(0.03)	2	3.69(0.25)	7.36(0.47)
Na_2O	3.93(0.11)	5.38	5.32(0.21)	4.16(0.26)
K_2O	4.73(0.10)	2.97	9.17(0.39)	1.28(0.1)
Cl	-	-	0.26(0.14)	-
P_2O_5	-	0.11	0.12(0.05)	-
Total	100	99.6	99.76(0.58)	99.25
n[5]	4	1	19	4

[1]Mono Craters rhyolite. EPMA analysis.
[2]Aniakchak rhyodacite. XRF analysis (Larsen, 2006)
[3]EU2 Vesuvius 79AD k-phonolite. EPMA analysis (Shea et al., 2010a)
[4]Okmok basaltic andesite. EPMA analysis (Wong and Larsen, 2009).
[5]Number of analyses

2.9 Appendix A

2.9.1 Experimental methods

The starting materials were loaded into 5-mm-diameter Ag (T=900 $^{\circ}$C) or Au (T=1025 $^{\circ}$C) capsules. The powders were loaded with sufficient de-ionized water for saturation at the initial pressure and welded shut using a PUK 3 professional arc welder. To produce a relatively large sample size for permeability measurements, 0.1 to 0.14 grams of powder were loaded into capsules containing 0.004 to 0.013 grams of water to achieve 3.7 to 9.4% weight percent water. Early experiments encountered difficulties with the samples expanding and cracking before extraction from the capsule, which rendered them useless for the permeability measurements. Thus, experiments were subsequently designed to include 25 mm long sample chamber and an extra 10 mm "headspace" to accommodate the exsolved and expanding gases in each experiment. This method was successful and preserved the physical integrity of the experiments. Each capsule was weighed before and after welding and then again after sitting on a hot plate at >100 $^{\circ}$C for 1 hour to check for leaks. Leaking capsules were discarded, unused. Each capsule was then loaded into a pressure vessel with the crimped, headspace end oriented upward. Following completion of the run, samples were weighed a third time to confirm no water was lost over the duration of the experiment.

Experiments were conducted using TZM (titanium-zirconium-molybdenum alloy) and MHC (molybdenum-hafnium-carbide alloy) vessels pressurized with ultra high purity Ar gas, with ~2.5 bars CH_4 added to help prevent hydrogen loss out of the experimental capsules. Because the research focus is on bubbles only, the experiments were not fO_2 buffered or monitored. The charges were compressed with the Ar-CH_4 mixture to an initial pressure of 150 MPa, lowered into a Deltech furnace and heated to 900°C (rhyolite, rhyodacite, phonolite) or 1025°C (basaltic andesite). Pressure was monitored using a Heise pressure gauge accurate to ± 1MPa, according to the manufacturer specifications for the UAF gauge. The multi-step decompressions were employed by bleeding pressure from a relief valve in 5 MPa increment steps followed by a holding period of 20 seconds, repeating each 5 MPa step until the final pressure was reached. The choice to use both continuous and step-wise decompression pathways stemmed from differences in decompression rate and the observed and anticipated response time of the material studied. The powdered rhyolite samples underwent continuous decompression at 2.5 – 4.1 MPa s^{-1} and step-wise decompression at 0.25 MPa s^{-1} (5 MPa/20 s; Table A-1). The

33

solid slab rhyolite runs underwent step-wise decompression at 0.25 MPa s^{-1}. The Aniakchak rhyodacite and Vesuvius K-phonolite powdered pumice samples were decompressed step-wise at 0.25 MPa s^{-1}, consistent with the rhyolite decompression rate. The basaltic andesite samples also comprised both powdered and solid, crystal-free, glassy chunks to examine whether the hydration bubbles influenced the results in the low viscosity samples. Both powdered and solid slab basaltic andesite experiments were decompressed continuously at 0.25 MPa s^{-1}. The basaltic andesite runs responded very quickly to decompression and so they were decompressed continuously at a rate of 0.25 MPa s^{-1}. Those runs were decompressed by cracking the bleed valve open very slightly, with the decompression rate measured by timing the pressure release on the Hiese Gause with a stopwatch.

2.9.2 Permeameter setup and testing

Samples were placed into the permeameter sample holder between two O-rings to achieve an airtight tight seal. Compressed air, regulated with a CKD pressure regulator to between 0.005 and 0.1 MPa, was passed through the sample to create a pressure gradient up and downstream of the sample in its holder. The differential pressure across the sample was measured using a Testo 526 digital manometer to between -50 to -980 hPa. Gas flow rates between 5 and 500 mL/min were measured using KOFLOC float-type flow meters with precision needle valves or by a digital mass flow meter (Omega FMA-4100/4300). Flow rates of $\leq$ 5 mL/min were measured using a flow-rate converter, which converts gas flow to water flow. Water expelled from the converter was collected in a glass beaker atop an Acculab VIC612 digital scale and the weight of displaced water with time was converted to gas flow rates (e.g., Takeuchi et al., 2008). The accuracy of the permeameter was verified using glass capillary tubes of known diameter (0.1, 0.3, and 0.5 mm) embedded in epoxy and the gas volume flux versus modified pressure gradient was compared with Poiseuille flow to ensure proper instrument operation (e.g., Rust and Cashman, 2004; Takeuchi et al., 2008). After this test, two natural pumice samples, AsFg1L and Ska Para, whose permeabilities were measured on the permeameter built by Takeuchi et al. (2008), were also measured on the UAF permeameter. The measurements agree closely with published values, differing by at most 0.1 log units (k_1) and 0.48 log units (k_2). An example of fitting a second-order polynomial to permeameter data can be found in Fig. A-1.

2.9.3 Image processing and analysis of experimental samples

The samples were polished while in the epoxy plugs to minimize damage. Ideally, the bulk density of the samples would be determined to calculate bulk vesicularity using Archimedes principle (Houghton and Wilson, 1989). However, the small size of the experimental charges required estimation of total porosity by stereology (Underwood, 1970) using photomicrographs of each sample. Reflected-light images were collected using a Nikon DS-Fi1 camera attached to an Ortholux II POL-BK petrographic microscope. One to fifteen images of each sample were collected at 5x, 10x, or 20x magnification. Both the number of images and magnification varied with the size of the sample and individual bubbles, with more images required for larger samples or those with complex bubble textures. Artifacts such as bubbles visible beneath the polished surface and heterogeneities in bubble digital numbers were manually removed. Cleaned images were converted to binary images and analyzed using NIH Image J. Total vesicularity was found by summing the bubble areas and dividing by the total area of the cross-section.

FTIR measurements

Small glass chunks from each of the experiments were extracted and doubly polished for micro-Fourier Transform Infrared Spectroscopy (FTIR) to determine dissolved water concentrations in the glasses after decompression. If the entire experimental charge was used for permeability analysis, the permeameter puck was submerged in acetone to dissolve the Crystalbond surrounding the sample after permeability measurements were completed. The exposed samples were re-mounted in Crystalbond and polished on both sides to create thin (~30-75 μm) wafers for transmission FTIR analyses of their water concentrations.

Water contents we calculated using the Beer-lambert law for the combined OH and H_2O peak at 3550 cm^{-1} for basaltic andesite and the overtones at 4520 and 5230 for rhyolite and 4470 and 5210 for phonolite (Table A-2.2):

$$C = \frac{18.01A}{\rho t \varepsilon} \qquad (2.7)$$

35

where C, is the concentration of water calculated by multiplying the molecular weight of water by the height of the absorbance peak (A) then dividing by the product of the glass density (ρ), glass thickness (t) of the measurement area and the compositionally dependent molar absorptivity (ε). Different values for ε were used depending on the composition of the glass and vibrational band used and can be found in Table A-2.3. Glass densities were calculated following Lange and Carmichael (1987) based on major element concentrations from electron microprobe analyses from the starting materials and experimental temperature.

To determine wafer thicknesses for each analytical area, samples were moved from the NaCl disk to a gold-coated mirror for reflectance measurements (Tamic et al., 2001; Nichols and Wysoczanski, 2007). The transparent samples produce interference fringes in the reflectance spectra that have a wavelength proportional to the sample thickness (e.g., Nichols and Wysoczanski, 2007). By counting the number of interference fringes (m) between a given wavenumber interval (v_2-v_1) and accounting for the refractive index of the glass (n), it is possible to determine the thickness of the sample:

$$t = \frac{\lambda}{2n(v_2 - v_1)} \qquad (2.8)$$

Reflectance spectra of 512 scans at a resolution of 4 cm^{-1} were collected and referenced against the surface of the gold-coated mirror. Interference fringes were counted over the wavenumber interval 2700 cm^{-1} to 2100 cm^{-1}. This interval was chosen because wavelength is found to increase at higher wavenumbers. However, wavenumbers near 2000 cm^{-1} are within error of thickness measurements determined by a micrometer (Wysoczanski and Tani, 2006).

2.10 Appendix A Figures
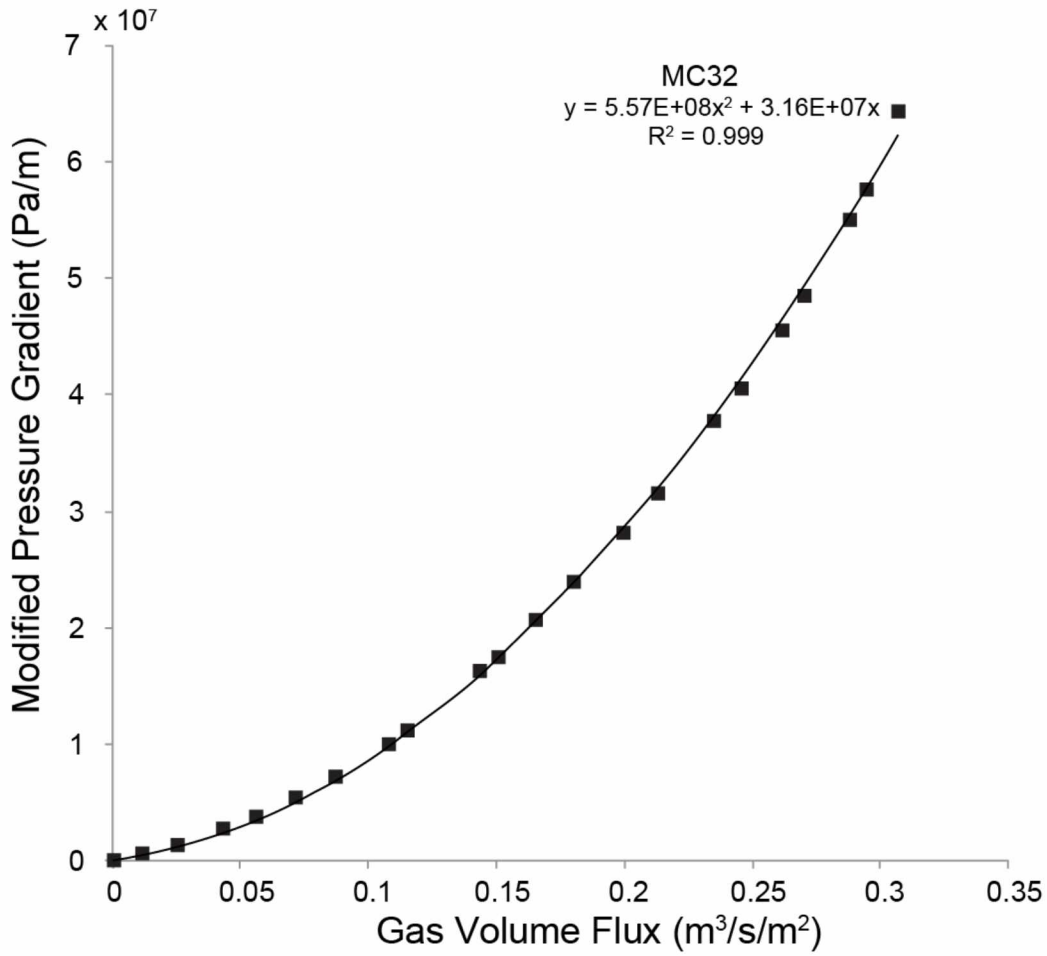
Figure A-1: Modified pressure gradient vs. gas flow and differential pressure measurements.

2.11 Appendix A Tables

Table A-1: Experimental run conditions

Run	[a]P_f (MPa)	[e]Decompression style	[b]dP/dt (MPa s^{-1})	[c]Φ_c (vol.%)	[d]k_1 (m^2)	[d]k_2 (m^2)
Mono Craters rhyolite - [i]solid slab (900°C)						
MCSS-4	125	Step-wise	0.25	1.3 (0.1)	n.d.	n.d.
MCSS-2	100	Step-wise	0.25	3.1 (0.1)	n.d.	n.d.
MCSS-3	75	Step-wise	0.25	20.4 (2.6)	n.d.	n.d.
MCSS-1	50	Step-wise	0.25	34.5 (2.1)	n.d.	n.d.
MCSS-6	25	Step-wise	0.25	59.5 (0.7)	n.d.	n.d.
MCSS-7	15	Step-wise	0.25	73.2 (2.1)	-13.06(0.03)	-9.93(0)
Mono Craters rhyolite - powder (900°C)						
MC-1	125	Continuous	2.5	0 (0)	n.d.	n.d.
MC-2-4	100	Continuous	8.3	6.5 (0.7)	n.d	n.d.
MC-P2	100	Continuous	2.5	16 (0.5)	n.d.	n.d.
MC-7	100	Continuous	6.2	17.4(1.4)	n.d.	n.d.
MC-3-2	75	Continuous	3.4	31 (2.0)	n.d.	n.d.
MC-6	50	Continuous	2.9	49 (1.4)	n.d.	n.d.
MC-8	40	Continuous	3.67	61 (3.4)	n.d.	n.d.
MC-4	35	Continuous	4.11	78 (2.8)	-13.95(0.05)	-11.09(0.33)
MC-5	25	Continuous	3.05	74 (1.8)	-13.04(0.01)	-8.73(0.13)
MC-24	100	Step-wise	0.25	23.5 (2.1)	n.d.	n.d.
MC-29	75	Step-wise	0.25	11.0 (1.7)	n.d.	n.d.
MC-25	50	Step-wise	0.25	68.3 (2.2)	-13.06(0.01)	-9.21(0.16)
MC-20	37	Step-wise	0.25	66.0 (0.7)	-14.43(0.03)	-11.29(0.22)
MC-21	35	Step-wise	0.25	63.5 (0.7)	n.d.	n.d.
MC-37	33	Step-wise	0.25	67.0 (3.5)	n.d.	n.d.
MC-31	15	Step-wise	0.25	73.3 (3.1)	-14.41(0.04)	-11.65(0.11)
MC-27	15	Step-wise	0.25	83.2 (0.7)	-13.72(0.01)	-11.12(0.20)
Aniakchak rhyodacite - powder (900°C)						
AnRd-22	100	Step-wise	0.25	36.7 (3.1)	n.d.	n.d.
AR-46-2	75	Step-wise	0.25	25.6 (2.1)	n.d.	n.d.
AnRd-23	50	Step-wise	0.25	57.8 (5.1)	n.d.	n.d.
AnRd-24	40	Step-wise	0.25	64.5 (0.7)	-12.21(0.04)	-7.79(0.08)
AR-47	35	Step-wise	0.25	75.0(4.4)	n.d.	n.d.
AR-48	15	Step-wise	0.25	77.3(3.6)	-13.57(0.01)	-9.95(0.20)
Vesuvius K-phonolite – powder (900°C)						
VP-17	150	Step-wise	0.25	12.5 (0.3)	n.d.	n.d.
VP-18	125	Step-wise	0.25	33.5 (0.7)	n.d.	n.d.
VP-16	100	Step-wise	0.25	9.0 (1.7)	n.d.	n.d.
VP-15	75	Step-wise	0.25	18.8 (4.3)	n.d.	n.d.
VP-12	50	Step-wise	0.25	51.2 (3.1)	n.d.	n.d.
VP-23	30	Step-wise	0.25	75.6 (1.9)	-14.61(0.07)	-11.06(0.81)
VP-24	25	Step-wise	0.25	73.9 (0.2)	-13.26(0.03)	-7.95(0.20)
VP-25	20	Step-wise	0.25	76.6 (2.0)	-12.42(0.01)	-8.81(0.01)

Table A-1 continued.

Okmok basaltic andesite – solid slab (1025°C)						
BASS-6	50	Continuous	0.25	23.8 (0.7)	n.d.	n.d.
BASS-2	50	Continuous	0.25	6.8 (1.7)	n.d.	n.d.
BASS-3	35	Continuous	0.25	29.7 (2.2)	n.d.	n.d.
BASS-5	15	Continuous	0.25	-[h]	n.d.	n.d.

Okmok basaltic andesite – powder (1025°C)						
OK52A-11	50	Continuous	0.25	37.0 (1.0)	n.d.	n.d.
OK52A-10	45	Continuous	0.25	38.0 (1.0)	n.d.	n.d.
OK52A-9	35	Continuous	0.25	39.0 (1.0)	n.d.	n.d.
OK52A-13	30	Continuous	0.25	45.0 (2.2)	n.d.	n.d.
OK52A-7	25	Continuous	0.25	56.0 (0.7)	n.d.	n.d.
OK52A-14	20	Continuous	0.25	49.0 (2.1)	n.d.	n.d.
OK52A-8	15	Continuous	0.25	62.0 (1.9)	n.d.	n.d.
OK52A-15	10	Continuous	0.25	63.0 (1.7)	n.d.	n.d.

[a] Final experimental pressure

[b] Decompression rate

[c] Average vesicularity determined from area measurements of photomicrographs. 1s standard deviation of all measurements are given in parentheses.

[d] Average viscous (k_1) and inertial (k_2) values from repeated permeability measurements.

[e] Experiment was either decompressed continuously by opening the bleed valve slightly and timing the pressure release on the Hiese gauge with a stopwatch or decompressed in step-wise fashion by releasing 5 MPa using the bleed valve and holding for a period of 20 seconds. This procedure was repeated until the desired final pressure was released.

[g] Permeability below detection limit of permeameter. ($\log k_1 \sim -15.5$)

[h] Sample was destroyed during polishing process, therefore porosity was not measured. However, permeability was measured before this occurred.

[i] Form of starting material.

Table A-2: FTIR analyses

[a]Run	[b]r	[cj]t (μm)	[d]Abs_{4500}	[e]OH_{4500}	[i]Abs_{5200}	[fi]H_2O_{5200}	[i]Abs_{3550}	[gi]H_2O_{total}
[h]Mono Craters rhyolite								
MCSS1_1	2345	87.6(0.8)	0.014(2)	0.82(2)	0.071(1)	2.02(2)	-	2.84(2)
MCSS1_2	2345	89.9(5.3)	0.023(2)	1.38(3)	0.031(1)	1.53(1)	-	2.92(3)
MCSS2_1	2354	67.3(1.2)	0.026(2)	2.10(2)	0.032(1)	2.07(2)	-	4.16(3)
MCSS2_2	2354	80.7(1.9)	0.039(2)	2.59(4)	0.029(1)	1.57(1)	-	4.17(4)
MCSS4_2	2359	66.6(1.1)	0.016(6)	1.30(8)	0.050(1)	3.25(2)	-	4.56(9)
MCSS4_3	2359	56.6(0.1)	0.022(3)	2.09(6)	0.034(1)	2.65(2)	-	4.74(6)
MCSS6_1	2341	94.7(2.5)	0.014(2)	0.81(2)	0.024(1)	1.12(1)	-	1.94(2)
MCSS6_2	2341	90.7(1.4)	0.013(2)	0.77(2)	0.024(3)	1.16(3)	-	1.93(4)
MC29_2	2383	103.6(0.9)	0.014(2)	2.95(2)	0.071(5)	0.71(8)	-	3.66(9)
MC29_3	2383	96.8(2.7)	0.023(1)	2.43(1)	0.054(2)	1.32(3)	-	3.80(3)
MC38_3	2377	83.5(0.7)	0.024(3)	1.56(4)	0.028(1)	1.45(2)	-	3.01(5)
MC38_5	2377	62.7(1.1)	0.025(6)	2.18(11)	0.012(3)	1.05(1)	-	3.23(11)
MC21_2	2377	87.2(6.5)	0.024(1)	1.47(2)	0.026(1)	0.98(2)	-	2.45(2)
MC21_5	2377	90.9(0.4)	0.018(1)	1.05(1)	0.027(1)	1.29(1)	-	2.34(2)
MC27_2	2373	84.4(1.1)	0.011(4)	0.70(4)	0.046(4)	2.40(3)	-	3.09(5)
MC27_3	2373	97.3(2.5)	0.029(2)	1.59(3)	0.036(3)	1.60(4)	-	3.19(5)
Aniakchak rhyodacite								
AR46_1	2446	104.6(1.0)	0.025(1)	1.40(1)	0.0514(2)	2.85(3)	-	4.22(4)
AR46_2	2446	111.3(1.6)	0.021(3)	1.14(3)	0.066(2)	3.03(3)	-	4.17(4)
AR46_3	2446	103.2(2.1)	0.024(1)	1.45(1)	0.058(2)	2.51(3)	-	3.97(3)
AR23	2442	103.4(0.7)	0.026(1)	1.52(1)	0.034(3)	1.68(4)	-	3.20(4)
Vesuvius K-phonolite								
VP12_1	2521	103.8(1.6)	0.018(1)	1.11(1)	0.023(3)	1.38(3)	-	2.49(4)
VP12_2	2521	102.5(1.5)	0.019(1)	1.19(1)	0.022(2)	1.30(2)	-	2.49(3)
VP12_3	2521	102.8(0.5)	0.020(1)	1.22(1)	0.020(2)	1.19(2)	-	2.41(2)
VP15_2	2525	64.2(0.3)	0.010(2)	1.01(1)	0.020(1)	2.03(5)	-	3.04(3)
VP15_3	2525	94.6(1.3)	0.011(2)	0.74(2)	0.034(1)	2.18(2)	-	2.92(2)
VP15_4	2525	80.7(2.2)	0.009(2)	0.71(2)	0.032(1)	2.38(2)	-	3.09(3)
VP17_2	2537	95.5(6.6)	0.018(1)	1.21(1)	0.049(5)	3.09(9)	-	4.30(9)
VP17_3	2537	109.8(0.8)	0.013(2)	1.30(2)	0.055(3)	3.06(5)	-	4.37(5)

41

Table A-2 continued

VP18_1	2533	139.5(4.6)	0.030(1)	1.36(1)	0.015(6)	2.58(8)	-	3.94(8)
VP18_3	2533	120.3(1.6)	0.020(2)	1.05(4)	0.058(4)	2.95(6)	-	3.99(7)

Okmok basaltic andesite

OK10_1	2671	66.9(1.3)	-	-	-	-	1.353(4)	2.18(7)
OK10_2	2671	63.3(0.5)	-	-	-	-	1.256(7)	2.13(13)
OK10_4	2671	68.2(1.6)	-	-	-	-	1.387(1)	2.18(18)
OK9_1	2670	45.7(3.2)	-	-	-	-	0.807(3)	1.89(6)
OK9_3	2670	66.6(2.8)	-	-	-	-	1.186(12)	1.91(20)
OK9_4	2670	58.5(1.8)	-	-	-	-	1.050(18)	1.92(33)
OK13_1	2669	49.2(0.9)	-	-	-	-	0.769(6)	1.68(11)
OK13_2	2669	51.1(2.4)	-	-	-	-	0.832(6)	1.75(11)
OK13_3	2669	52.8(0.9)	-	-	-	-	0.813(6)	1.64(11)
OK7_1	2668	42.2(2.1)	-	-	-	-	0.630(4)	1.60(7)
OK7_2	2668	49.4(0.5)	-	-	-	-	0.722(4)	1.58(7)
OK7_3	2668	44.7(5.0)	-	-	-	-	0.682(7)	1.62(15)
OK8_1	2666	59.4(2.3)	-	-	-	-	0.656(4)	1.18(6)
OK8_2	2666	69.7(1.4)	-	-	-	-	0.787(6)	1.20(8)
OK8_3	2666	80.2(1.2)	-	-	-	-	0.917(5)	1.23(6)

[a] Sample name and analysis number

[b] Glass densities were calculated following Lange and Carmichael (1987) based on major element concentrations from electron microprobe analyses from the starting materials and experimental temperature.

[c] Thickness measurements were estimated following Tamic et al. (2001) and Nichols and Wysoczanski (2007). The refractive index for each composition was calculated following Church and Johnson (1980) from electron microprobe analyses, as follows: rhyolite, 1.49; rhyodacite, 1.53; K-phonolite, 1.54; and basaltic andesite, 1.58.

[d] Absorbance peak heights (Abs) from 4500 cm^{-1}, 5200 cm^{-1} or 3550 cm^{-1} bands

[e] OH (wt.%) determined by 4500 cm^{-1} absorbance peak using molar absorptivity of 1.73 L/mol/cm^{-1}, rhyolite (Newman et al., 1986); 1.50 L/mol/cm^{-1}, rhyodacite (Ihinger 1994); 1.14 L/mol/cm^{-1}, K-phonolite (Iacono Marziano et al. 2007)

[f] H_2O (wt.%) determined by 5200 cm-^{1} absorbance peak using molar absorptivity 1.61 L/mol/cm^{-1}, rhyolite (Newman et al., 1986); 1.86 L/mol/cm^{-1}, rhyodacite (Ihinger 1994); 1.18 L/mol/cm^{-1}, K-phonolite (Iacono Marziano et al., 2007).

[g] H_2O_{total} = OH + H_2O 3550 cm^{-1} absorbance band or combined 4500 +5200 cm^{-1} OH and H_2O concentrations. Total H_2O concentration of 3550 absorbance peak using molar absorptivity 63 L/mol/cm^{-1} (Dixon et al., 1995), for basaltic andesite.

[h] Mono Craters Rhyolite data is for runs using powder starting materials only

[i] Numbers in parentheses are 1σ error corresponding to the last significant digit

[j] Numbers in parentheses are 1σ error.

Table A-3: Molar absorption coefficients used for calculating water concentrations.

Composition	Absorption band (cm^{-1})	Molar absorptivity (ε) ($L/mol/cm^{-1}$)	Source
Rhyolite	4500	1.42 ± 0.12	Okumura and Nakashima (2005)
	5200	1.75 ± 0.08	
Rhyodacite	4500	1.23 ± 0.06	Ohlhorst et al. (2001)
	5200	1.44 ± 0.06	
Phonolite	4470	1.14 ± 0.09	Iacono-Marziano, et al. (2007)
	5210	1.18 ± 0.11	
Basaltic Andesite	3550	63 ± 3	Dixon et al. (1995)

Chapter 3 Crystal-controls on permeability development and degassing in basaltic andesite magma[1]

3.1 ABSTRACT

Understanding degassing of mafic magmas is important for modeling eruptions and examining controls on eruption style. We conducted high-pressure-high-temperature, isothermal decompression experiments to investigate the effects of decompression–induced crystallization on permeability development and magma degassing. Experiments were performed on hydrous basaltic andesite (54 wt.% SiO_2) and decompression rates equivalent to magma ascent velocities of ~1 – 3 m s^{-1}. We measured the gas flux of the quenched samples using a bench-top permeameter and calculated the Darcian (k_1) and inertial (k_2) permeabilities using the Forchheimer equation. The experimental samples developed permeability at a critical vesicularity (Φ_c) of 56.4 vol% ± 2.7 (at 0.125 MPa s^{-1}) and 50.76 ± 5.6 vol% (at 0.083 MPa s^{-1}), considerably lower than the $\Phi_c > 63$ vol% permeability threshold determined for crystal-free basaltic andesite melts. The percolation threshold decrease is observed when the microlites comprise ≥ ~20 vol% and can be explained by the onset of yield strength, which occurs when the crystals form a loosely packed, touching framework.

3.2 INTRODUCTION

It has long been recognized that volcanic eruption styles are linked to magma composition. Mafic magmas erupt less explosively than silicic magmas possibly because of their low melt viscosity. Within the suite of mafic magmas, there are clear differences in eruption style between water-poor (e.g., Hawaii, USA) and water-rich (e.g., Mount Spurr, Alaska, USA) magmas. H_2O-rich magmas undergo rapid syn-ascent crystallization driven by H_2O loss during decompression, specifically plagioclase, because it is particularly sensitive to the amount of H_2O within the melt (Hammer and Rutherford 2002). The greater explosivity of these magmas has been attributed to rheological changes in the melt caused by crystallization (Mader et al., 2013). However, the effect of crystals on the distribution of the gas phase within the crystal-melt suspension, specifically the role of crystallinity in controlling permeability development, has yet

---

[1] Lindoo, A., Larsen, J.F., Cashman, K.V., Oppenheimer, J., Crystal-controls on permeability development and degassing in basaltic andesite magma: Accepted for publication in Geology.

to be assessed. We address this question experimentally, and demonstrate that crystals both lower the percolation threshold and stabilize permeable pathways.

3.3 BACKGROUND

Volatile exsolution from ascending magma and subsequent expansion is the largest driving force for magma acceleration, ascent and eruption (Mueller et al., 2008; Rust and Cashman, 2011). Permeability develops during vesiculation through bubble coalescence, which allows efficient volatile transport through connected pathways and relieves overpressure. Studies of natural samples have inferred that the onset of permeability may affect eruption style but have not fully examined the relative importance of ascent rate, melt viscosity, the presence of crystals, or the amount of shear stress on degassing efficiency (Mueller et al., 2008; Rust and Cashman, 2011). The critical porosity at which magma becomes permeable is termed the percolation threshold. Mafic pyroclasts record apparent percolation thresholds near 30 vol% bubbles, followed by a gradual increase in permeability as vesicularity increases (Mueller et al., 2008). Crystal-free silicic pumice samples, in contrast, have a percolation threshold of 70 - >80 vol% (Mueller et al., 2008; Wright et al., 2009). Experiments further show that permeability increases rapidly over a short vesicularity interval (Takeuchi et al., 2009; Lindoo et al., 2016). The compositional difference in apparent permeability thresholds can be explained by bubble collapse accompanying gas loss (hysteresis) that reduces porosity while permeability is maintained or increased because of simplified pathway geometries (Saar et al., 2001; Rust and Cashman, 2004).

The role of syn-ascent crystallization, which is common in mafic pyroclasts formed from hydrous (> 2–3% dissolved H_2O) magma, is not considered in most permeability studies. The rheological and mechanical effects of crystals and bubbles can affect magma outgassing (Parmigiani et al., 2011; Oppenheimer et al., 2015; Spina et al., 2016). Experimental and numerical studies show that both particle (crystal) volume fraction and shape control rheology (Saar et al., 2001; Walsh and Saar, 2008; Mader et al., 2013). Specifically, two remarkably stable particle concentration thresholds affect magma rheology: (1) the onset of apparent yield strength and (2) attainment of random close packing (e.g., Mueller et al., 2009). The former occurs once the volume fraction of particles forms a loosely touching network (Kerr and Lister, 1991) and the latter occurs at a particle concentration sufficiently high to prevent particle movement (Mueller

et al., 2009). However, the thresholds are dependent on particle aspect ratios, where higher aspect ratios decrease the thresholds (Saar et al., 2001; Walsh and Saar, 2008; Mueller et al., 2009; Spina et al., 2016). Pervasive crystal networks also deform bubbles and therefore enhance outgassing (Oppenheimer et al., 2015). The lowest particle fraction for network formation is 22% for cubes and lower for prisms (Saar et al., 2001). Therefore, we hypothesize that crystals should start to affect the behavior of the exsolved volatile phase when they approach 20 vol%. Here we use decompression experiments to test this hypothesis and to explore the role of decompression crystallization in mafic eruption dynamics.

3.4 METHODS

3.4.1 Starting materials and decompression experiments

Three sets of isothermal decompression experiments were performed using powdered basaltic andesite from Westdahl volcano, AK ("BA"; Rader and Larsen, 2013), with Okmok basaltic andesite used as a crystal-free comparison (Table 1; Rader and Larsen, 2013). We follow the methods of Lindoo et al. (2016) by compressing samples to an initial pressure of 100 MPa and lowering them into a DelTech vertical tube furnace. The samples were then heated to 989°, 1000° or 1025 °C for 24 h, after which they were decompressed continuously at 0.125 or 0.083 MPa s^{-1} to pressures between 75 and 10 MPa (Appendix Table B-1). After quenching, sample preparation and permeability measurements were performed as described in Lindoo et al. (2016).

The key parameters used to monitor the evolution of degassing in our samples were bubble vol% (vesicularity), crystal vol% (crystallinity), crystal aspect ratios, and sample permeability. To measure these variables, a section of each experimental slug was cut and mounted on a glass slide with Crystalbond 509. We collected 22 Back-Scattered Electron (BSE) images per sample using the University of Alaska Fairbanks Advanced Instrumentation Laboratory (AIL) JEOL JXA-8530F electron microprobe at 15 keV and with a 10 nA scanning beam. The BSE images were segmented in Adobe Photoshop (www.adobe.com/Photoshop) and then vesicularity was measured by calculating the area fraction of vesicles using NIH ImageJ (http://imagej.nih.gov/ij/) and correcting for melt volume. We applied an additional correction to our melt-referenced vesicularities to account for bubble shrinkage during quenching (Marxer et al., 2015). ImageJ was also used to measure the vesicle-free crystallinity as well as crystal area, size and aspect ratio. The measurements were input into CSDSlice (v.5; Morgan and Jerram

47

2006) to determine their best-fit crystal habits. To view the vesicle structure in three dimensions, we obtained scans of six experiments from the High-Resolution X-ray Computed Tomography Facility at the University of Texas at Austin (USA), with spatial resolution of 5 μm voxel size (Table B-1). The scans were uploaded into iMorph (http://imorph.sourceforge.net/) three dimensional (3-D) image analysis software, and segmented into two phases, glass and crystals, to render a qualitative comparison between relatively crystal-rich and crystal-poor samples.

3.4.2 Permeability measurement

Permeability was measured using a bench-top permeameter built at the University of Alaska Fairbanks after Takeuchi et al. (2008). The permeameter design allows measurements of small experimental samples by forcing gas orthogonally through the sample and measuring the differential pressure upstream and downstream over a range of gas flow rates. Samples were no thinner than 10x the largest bubble diameter. The Forchheimer equation, a modified version of Darcy's Law that accommodates inertial effects, was used to calculate Darcian (k_1) and inertial (k_2) permeabilities of the samples (Rust and Cashman, 2004; Takeuchi et al., 2008; Lindoo et al., 2016). Permeability of each sample was measured three times and yielded standard deviations of 0.03 - 0.20 log units (k_1) and 0.02 - 0.63 log units (k_2).

3.5 RESULTS

3.5.1 Bubble textures

Vesicularities of all experiments are lower than equilibrium values calculated from solubility curves (Moore et al., 1998) using melt compositions derived from MELTS (http://melts.ofm-research.org). This is also the case in crystal-free control experiments, and is consistent with observations of Lindoo et al. (2016) for a similar composition (Fig. B-1a). Low vesicularities are in part due to bubble shrinkage during quench and were corrected (Marxer et al., 2015; Fig. B-1b). We confirmed this interpretation through Fourier transform infrared spectroscopy analyses, which verify that equilibrium dissolved water concentrations were maintained in all the samples (Fig. B-2, Table B-2). Melt-corrected vesicularities derived from BSE images increased as a function of decreasing final pressure (P_f), from 7.6 (at P_f = 85 MPa) to 68.3 vol% (P_f = 10 MPa) in experiments decompressed at dP/dt = 0.125 MPa s^{-1}(t = time; Table B-1). The vesicularities increased from 15.2 (at P_f = 75 MPa) to 87.7 vol% (P_f = 25 MPa) in those decompressed at dP/dt = 0.083 MPa s^{-1} (for measurement errors, see Table B-1).

With the exception of crystal-free experiments OK17 and OK19, all bubble shapes are irregular (Fig. 3.2, 3.3 and B-4). At high final pressures (low crystallinities), bubbles are nearly spherical but with dented or concave walls. At intermediate pressures (ΔP ~50 MPa), vesicles start to deform as they skirt the crystal margins (Fig. B-4A). At final pressures ≤ 25 MPa, bubbles form finger-like networks throughout the melt (Fig. B-4B and B-4C). Unfortunately, we could not accurately quantify the connectivity of the bubble networks due to the voxel resolution of our micro- X-ray computed tomography images. However, visual inspection of the samples suggests a positive correlation between crystal content and bubble connectivity (Fig. 3.2).

3.5.2 Crystal textures

Crystallinities decrease from 24.6 vol% at their holding pressure of 100 MPa to 14.2 vol% at 50 MPa before rising to 26.3 - 31.5 (0.125 MPa s^{-1}) and 18.6 – 33.1 (0.083 MPa s^{-1}) vol% at final quench pressures below 40 MPa (Table B-1). The change in crystallinity with pressure reflects the crystallization history of pyroxene and plagioclase crystals. At initial pressures the crystals comprise relict phenocrysts from the starting material, as evidenced by resorption rims. At lower pressures they can still be found in the interiors of some crystals, encapsulated by euhedral rims from decompression growth. Pyroxene crystals maintain blocky, euhedral shapes throughout the experiments, while plagioclase crystals are prismatic and tabular in shape regardless of decreasing final pressures (Fig. B-4). For this reason, plagioclase crystals have high aspect ratios of 2.3 – 8. Crystal clustering is minor (Fig. B-5). When comparing samples where all experimental parameters are the same, the slow decompression experiments crystallized more extensively.

3.5.3 Permeability measurement

Permeability was not measurable in crystal-free samples, consistent with the results of Lindoo et al. (2016; Fig. 3.1A). For crystal-rich samples (>20 vol% microlites), in contrast, permeability developed at final pressures of 25-30 MPa (Fig. 3.1A, Table B-1). Moreover, our experiments show that the presence of crystals > 20% microlites increases bubble connectivity (Fig. 3.2), as measured by permeability, which increases abruptly at vesicularities of 46–55 vol% (Fig. 3.1B). Additionally, the vesicularity necessary for permeability development appears to decrease with increasing crystal content (gray line, Fig. 1B). For example, samples with initial temperature T_{init} = 1000°C and decompressed at 0.125 MPa s^{-1} to 25 MPa have ≥ 26% microlites and become permeable at a vesicularity of 54 vol%. In contrast, samples decompressed at 0.083

49

MPa s^{-1} under the same conditions have, on average, ~ 22% microlites and become permeable at a vesicularity of 60 vol% (Fig. 1B, Table B-1). Both permeability and vesicularity continue to increase to k_1 ~10^{-10} m^2 at vesicularities ~80%. Although the experimental samples are much smaller (~5 mm diameter, ~5-10 mm long) than juvenile pyroclasts in both overall size and bubble size, their Darcian and inertial permeabilities are quite similar (Fig. B-7).

3.6 DISCUSSION
3.6.1 Reduction of the percolation threshold

Our experiments show that the presence of > 20% microlites has a profound effect on permeability development during decompression, with the vesicularity of permeability onset reduced from > 63% to ≤ 56% across the crystallinity threshold. Moreover, decompression rate matters: slower decompression allows more time for degassing-induced crystallization, which lowers the vesicularity at which bubbles connect (the suspension becomes permeable)(Fig. 3.1B). Additionally, the final (low pressure) permeabilities are 1–2 orders of magnitude greater than those measured in crystal-free experiments and more silicic experiments quenched at similar pressures (Fig. 3.1A; Lindoo et al., 2016).

Mechanical effects imposed by crystals result in reduction of the percolation threshold, as previous experiments show melt viscosity does not have a control on the percolation threshold (Lindoo et al., 2016). Chemical changes occurring within the basaltic andesite melts during decompression are insignificant, with less than 10% increase in SiO_2 content estimated (See data repository, Rader and Larsen, 2013). Using a model based on the Vogel-Fulcher-Tammann equation (Giordano et al.,2008), the most evolved melt composition in our experiments would have a viscosity of approximately log η (Pa s) = 3.66 ± 0.18. This is significantly lower than the log η (Pa s) = 4 relaxation threshold (Lindoo et al., 2016) and thus rules out permeability preservation to be the result of increasing melt viscosity alone.

It is compelling that a critical crystallinity of ~20% for permeability reduction corresponds roughly to estimates of the crystal volume fraction at which prismatic crystals start to interact (e.g. Saar et al., 2001). These interactions cause the bulk suspension to show yield strength behavior at similar crystallinities (Philpotts, 1998; Saar et al., 2001; Hoover et al., 2001; Mueller et al., 2011; Picard et al., 2013; Fig. 3.3). This behavioral threshold depends on both

particle shape and degree of randomness in particle orientation. For this reason, the critical crystallinity will depend on the crystal aspect ratio (Fig. 3.3) and deformation history.

Both 2D and 3D images show that microlites affect vesicle shapes and appear to increase vesicle connectivity (Fig. 3.2, B-4). More evidence of a connected crystal framework is provided by the observation that the samples remain permeable after quenching, in contrast to experiments on crystal-free basaltic andesites, where the melt relaxes (and pathways close) during quenching (Lindoo et al., 2016). Maintenance of permeable pathways in crystal-bearing experiments may reflect the presence of a loose crystal "scaffolding" that maintains the structure of the pathways (Philpotts, 1998; Hoover et al., 2001; Parmigiani et al., 2016).

3.6.2 Degassing in crystal-free versus crystal-rich magmas

Degassing styles differ greatly in crystal-free versus crystal-rich experiments. In crystal-free samples (OK17 and OK19), permeabilities increase rapidly once the percolation threshold has been reached, and efficient degassing prevents bubble volumes from expanding past the percolation threshold (~63–80 vol%; Fig. 3.1 trend b); Rust and Cashman, 2011; Lindoo et al., 2016). The samples readily foam to high vesicularities (>63%), become permeable and degas (Fig. B-3). The presence of crystals, in contrast, allows permeability to develop at lower vesicularities. Additionally, in these samples permeability increases steadily with increasing vesicularity, and to very high values (Fig. 3.1 trend a). We propose that this pattern of permeability development may record creation of finger-like pathways that gradually penetrate through the sample, as illustrated by the extent of bubble connectivity exhibited by high crystallinity samples (Fig. 3.2B). It is important that crystal networks limit bubble growth and expansion; as a result, expanding bubbles deform around the crystal network, which enhances coalescence and bubble connectivity (e.g., Okumura et al.,2009). The deformed bubbles create paths for gas escape, resulting in efficient degassing (Parmigiani et al., 2016). The high final permeabilities of the crystal-rich samples likely reflect widening of bubble apertures (Wright et al., 2009), as predicted by the Kozeny-Carman relationship:

$$k_1 = \frac{\phi a^2}{C} \qquad (3.1)$$

where k_1 is permeability, ϕ is vesicularity, a the radius of the aperture connecting the bubbles, and C a constant based on pore geometry (Klug et al., 2002). Note that in this formulation, permeability is most sensitive to changes in a, thus enlargement and stabilization of pore radii alone will increase permeability without increasing (Parmigiani et al., 2016), or even reducing (Rust and Cashman, 2004), vesicularity.

3.7 CONCLUSIONS

In summary, we demonstrate that decompression-driven crystallization of mafic magmas during ascent not only changes the bulk rheology, but can also affect degassing efficiency. This observation has important implications for controls on mafic eruption styles. Most importantly, the processes that enhance gas loss can either (1) reduce the potential of explosive eruptions or (2) promote the formation of dense conduit plugs (which could increase the possibility of Vulcanian explosions). Defining threshold conditions required to anticipate transitions from effusive to explosive eruptions is critical for improved volcano hazard assessment. Our data provide some initial constraints for such an approach. For example, we show that decreasing the decompression rate from 0.125 MPa s^{-1} to 0.083 MPa s^{-1} also decreases the percolation threshold for onset of permeability (and, therefore, degassing). This simple observation may explain the common pattern of lava effusion following explosive eruptions, as the average mass eruption rate decreases. We expect that this pattern should apply to other magma compositions and decompression rates, although a full parameterization of decompression, crystallization and degassing is not yet possible given the limited experimental database, particularly for mafic compositions.

3.8 Figures
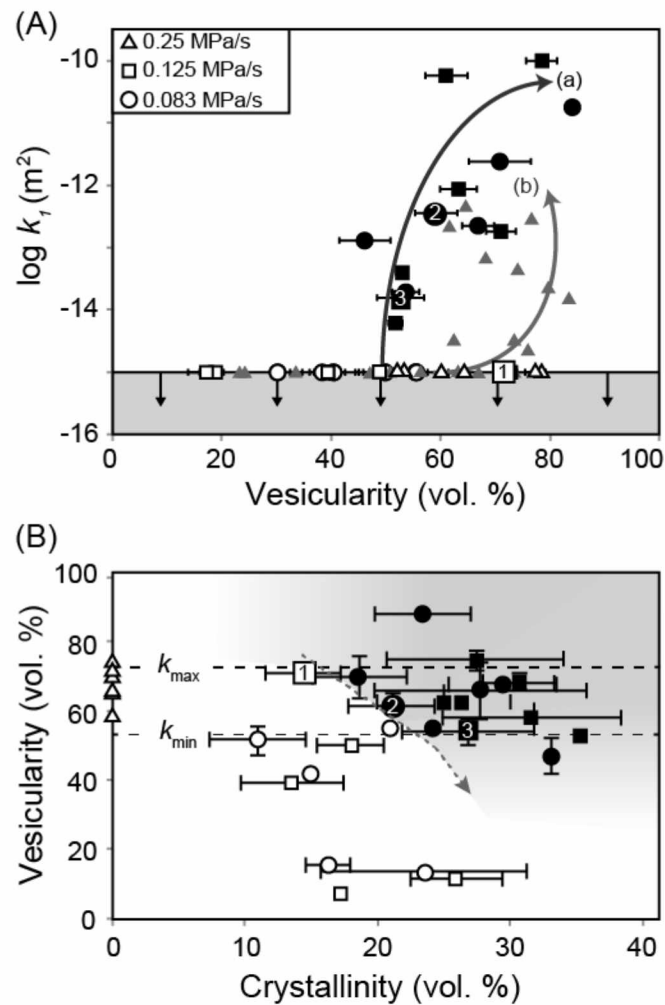
Figure 3.1. (A) Relationship between Darcian permeability as a function of quench-corrected vesicularity (Marxer et al., 2015). Open and closed symbols represent impermeable and permeable samples, respectively. Squares and circles represent experiments decompressed at 0.125 and 0.083 MPa s^{-1}. For comparison, triangle symbols represent basaltic andesite crystal-free experiments of Lindoo et al. (2016). Grey symbols are silicic crystal-free experiments of Lindoo et al. (2016). The data follow two trends: (a) gradual increase in permeability with increasing vesicularity and (b) abrupt development of permeability at high vesicularity without progressive increase in vesicularity. **(B)** The minimum vesicularity at which permeability is measureable (k_{min}) and the vesicularity where maximum permeability is observed (k_{max}) as a function of crystal content. The bubble content necessary for permeability development decreases with increasing crystal content (dashed grey line). Numbers 1-3 refer to binary images in figure 3.
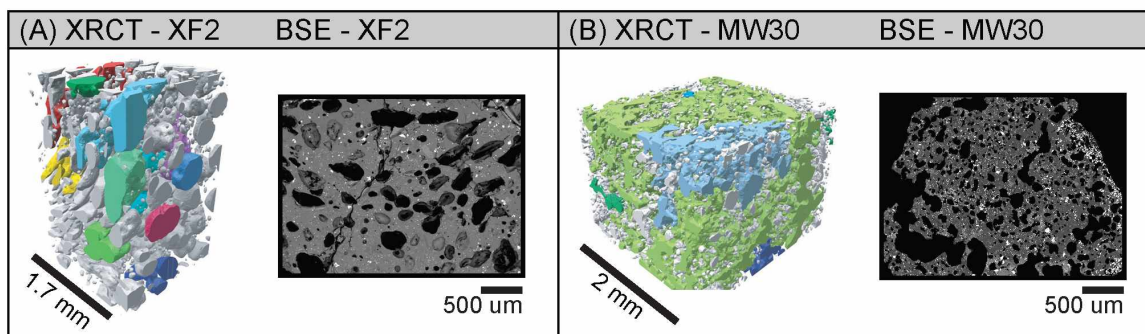
Figure 3.2. Sections of u-CT images from crystal-free (A) and crystalline (B) experiments with corresponding BSE images of the entire samples. Selections of individual bubbles and bubble networks have been highlighted with colors.
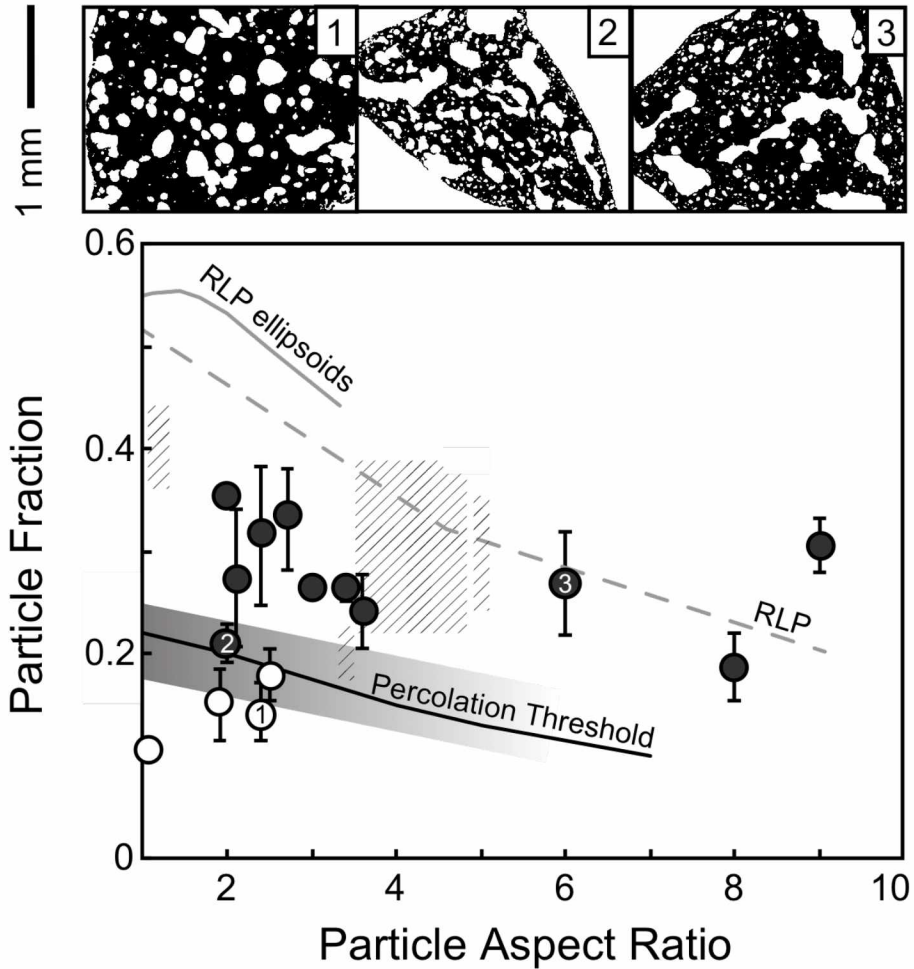
Figure 3.3. Rheological and packing thresholds from experimental and numerical studies. The lines mark numerical models for the onset of percolation threshold (Saar et al., 2001) and random loose packing of ellipsoids (Delany et al., 2011) as well as analog experiments for random loose packing (RLP, Mueller et al., 2008). The crosshatched regions represent the onset of yield strengths in experimental investigations (Philpotts et al., 1998; Hoover et al., 2001; Picard et al., 2013). The grey gradient highlights the formation of a particle framework we determined from our data. Binary images of (1) XF6, (2) MW24, and (3) MW25 are displayed.

3.8 Appendix B

3.8.1 Bubble and crystal texture results

Bubble rise out of the sample and into the headspace of the capsule could possibly influence experimental porosities (Lindoo et al., 2016). However, bubble rise is not expected to occur over the timescales of their decompression pathway (0.083-0.25 MPa s^{-1}; Lindoo et al., 2016). Using Stokes Law, bubble rise is negligible at ~ 2 x 10^{-4} mm over the course of the longest decompression timescale (18 mins.) and lowest melt viscosity (log η (Pa s) = 2.73 ± 0.14), and further slowed by the presence of crystals. Furthermore, FTIR data show equilibrium water concentrations (Fig. B-2, Table B-2; Marxer et al., 2015; Kennedy et al., 2016; Lindoo et al., 2016). Therefore, we fully attribute below-equilibrium vesicularities to degassing through permeable pathways and loss of internal bubble pressures and/or bubble shrinkage during quench. Shortly after decompression, vesicles begin to form elongate shapes as they skirt the margins of crystals (Fig. B-4A). At final pressures of 25 MPa and lower, bubbles form finger-like networks through the melt (Fig. S4B and C). This behavior occurs in experiments decompressed at both 0.125 MPa s^{-1} and 0.083 MPa s^{-1} (Fig. B-4D-F).

The bubbles in the crystal-free samples are abruptly different from crystal-rich samples (Fig. B-3). The bubbles in OK17 are small, spherical, and isolated, only making up <3 vol% of the sample. Decompressed at 0.083 MPa s^{-1}, OK19 appears to contain 3 populations of bubbles. Two populations (based on size) are large and spherical and appear to have nucleated during decompression. A possible third set of slightly irregularly shaped bubbles, some of which appear to have coalesced with neighboring bubbles, may have been affected by quench crystallization.

Spatial statistics were calculated on 2D images to quantify the extent of crystal clustering or regularity after Mongrain and Larsen (2009), who quantified the spatial distribution of bubbles within decompression experiments. However, there was no correlation between the spatial arrangements of crystals (i.e. clustered versus regular arrangement) in permeable versus impermeable samples (Fig B-5). The solidity and convexity of all bubbles were also calculated using a shape analysis macro for ImageJ, but no clear trends were found (Fig. B-6; Liu et al., 2015).

3.8.2 Permeability results

Initial Darcian permeabilities (k_1) are measurable at $\log k_1 = -14.21 \pm 0.06$ m^2 (0.125 MPa s^{-1}) and -13.71 ± 0.1 m^2 (0.083 MPa s^{-1}) and progressively rise with increasing vesicularity and decreasing quench pressure to maximum permeabilities of $\log k_1 = -10.02 \pm 0.23$ m^2 (0.125 MPa s^{-1}) and -10.71 ± 0.06 m^2 (0.083 MPa s^{-1}) (Fig. 3.3A, Table B-1). Inertial (k_2) permeabilities are measurable at $\log k_2 = -10.94 \pm 0.14$ m (0.125 MPa s^{-1}) and -10.52 ± 0.10 m (0.083 MPa s^{-1}) and from there increase with vesicularity and decreasing quench pressure to -7.03 ± 0.05 m (0.125 MPa s^{-1}) and -7.00 ± 0.07 m (0.083 MPa s^{-1}) (Fig. 3.3B).

3.8.3 Reduction of the percolation threshold

Lindoo et al. (2016) attributed their apparently impermeable samples to melt relaxation with subsequent closure of permeable pathways via relaxation of bubble apertures (Kennedy et al., 2016). If preservation of permeable pathways is solely dependent on melt viscosity, it would need to exceed $\sim \log \eta$ (Pa s)= 4 (Lindoo et al., 2016). A sufficient increase in melt viscosity past this threshold would make it impossible for the melt to relax within the quench timescale. We used MELTS to model the evolution of the initial composition (Table 1) as the solid fraction increased as a result of undercooling, assuming an initial pressure of 100 MPa and fO_2 at Ni-NiO. The results of the model were also compared to measured melt compositions from phase equilibria experiments of Rader and Larsen (2013), which were performed on the same starting material. We find the most evolved melt viscosity estimated with the model of Giordano et al. (2008) and using the MELTS model to be $\log \eta$ (Pa s)= 3.66 (SiO$_2$ = 58.9 wt. %) and compare this with $\log \eta$ (Pa s)= 3.29 (SiO$_2$ = 59.6 wt. %), which is the melt viscosity of an experiment from Rader and Larsen, (2013) with similar solid fraction as our most crystalline samples. Both melt viscosities are less than the relaxation threshold value of $\log \eta$ (Pa s)= 4 and therefore we cannot attribute permeability preservation to be the result of increasing melt viscosity alone.

3.9 Appendix B Figures
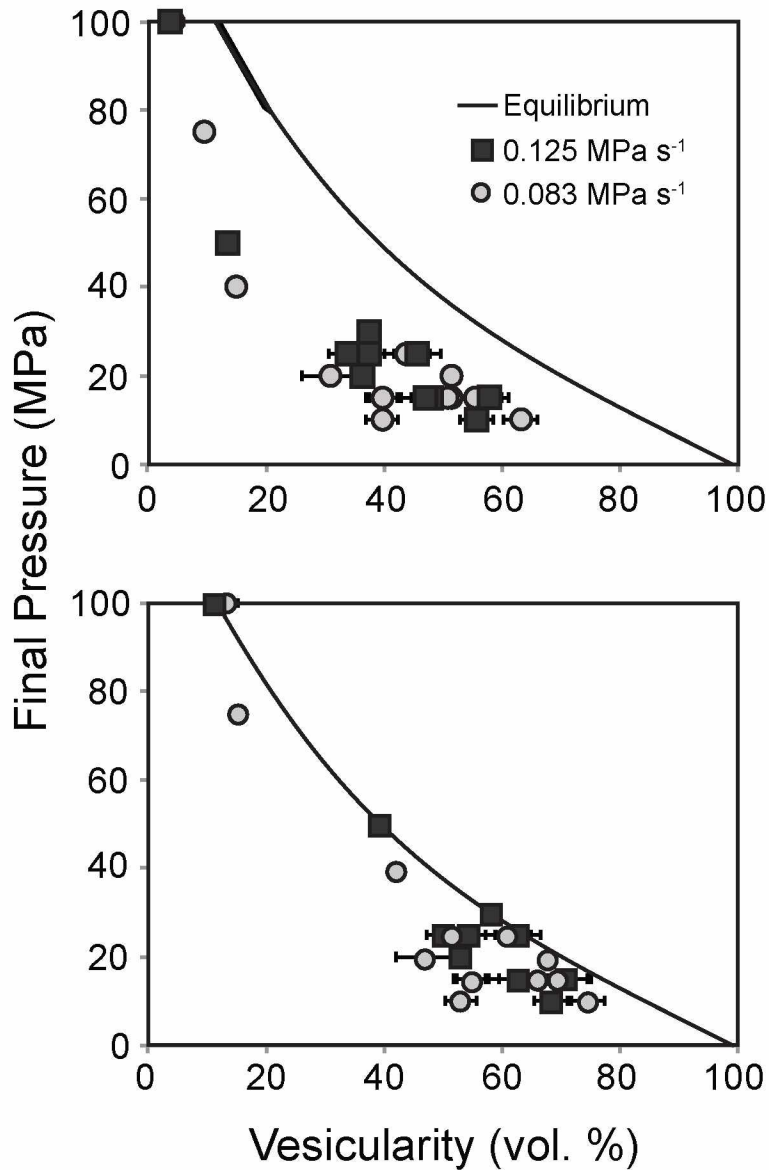
Figure B-1. (A) Melt-corrected vesicularities of experiments decompressed at 0.125 (squares) and 0.083 (circles) MPa s^{-1}. Equilibrium porosities were calculated using the method of Gardner et al., (1999). **(B)** Quench corrected vesicularities of experiments after the method of Marxer et al. (2015).
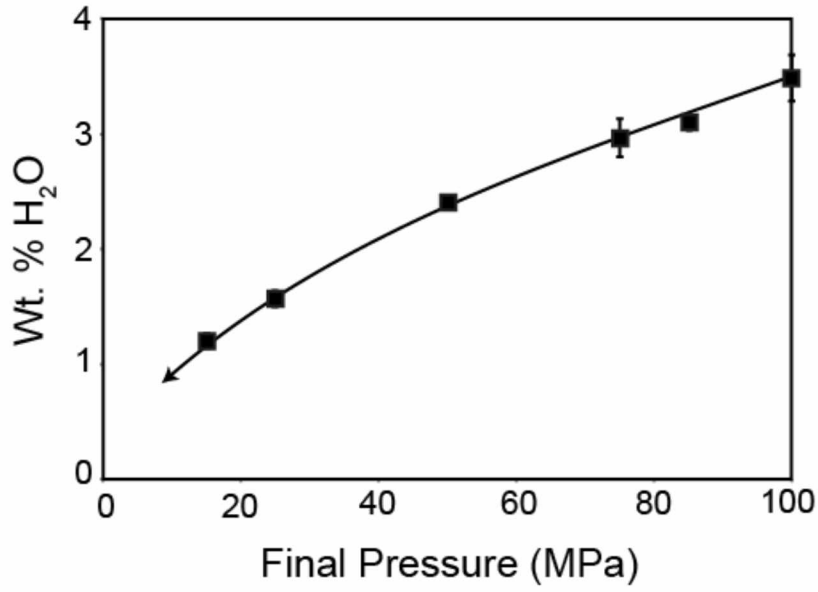
Figure B-2. Total water content in experimental samples measured using FTIR. The solid line represents equilibrium water concentrations in basaltic andesite melts (Moore et al., 1998). All samples track equilibrium solubility.
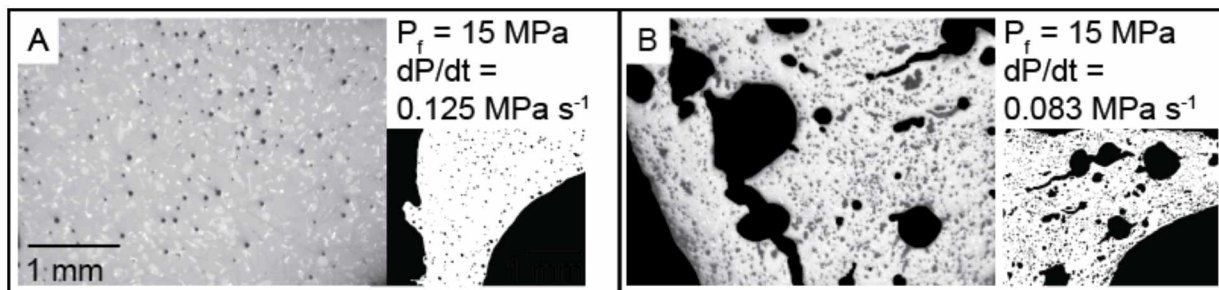
Figure B-3. Photomicrographs of crystal-free experiments (A) OK17 and (B) OK19.
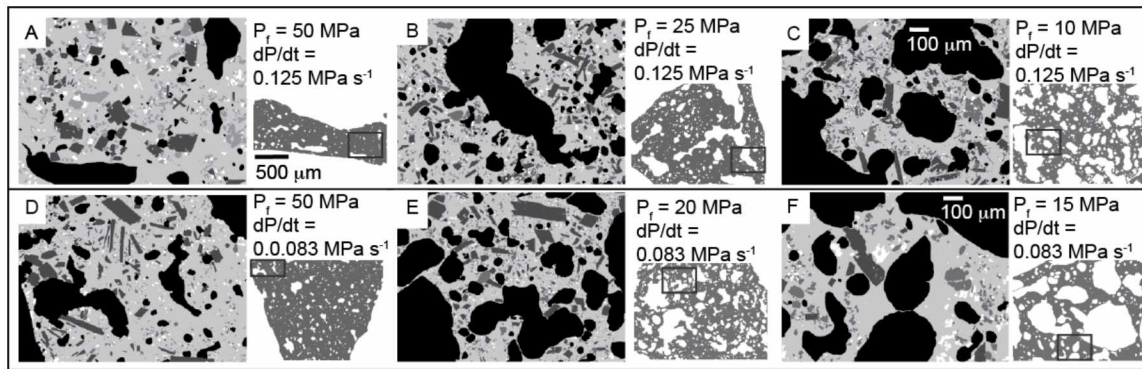
Figure B-4. Adobe Photoshop processed back-scattered electron (BSE) images of basaltic andesite samples (A) MW16, (B) MW24, (C) MW32, (D) MW22, (E) MW31, and (F) MW28. Images A-C are samples decompressed at 0.125 MPa s^{-1} and D-F were decompressed at 0.083 MPa s^{-1}. Samples are ordered by decreasing final pressure within their respective decompression rates.
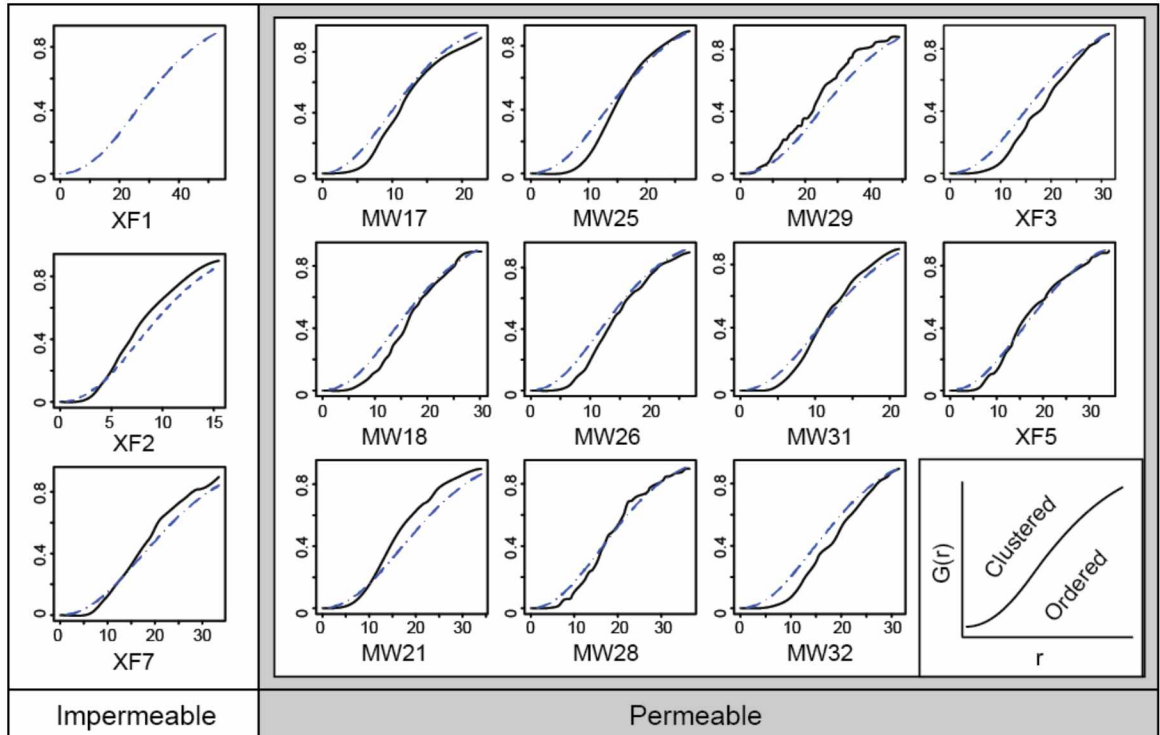
Figure B-5. The spatial homogeneity of the crystals was determined using the Nearest Neighbor Distribution function, which calculates distances from crystal centers to those of their nearest neighbors. This outputs a cumulative distribution, $G(r)$, at a radius r, which is compared to complete spatial randomness (Poisson Point Process).
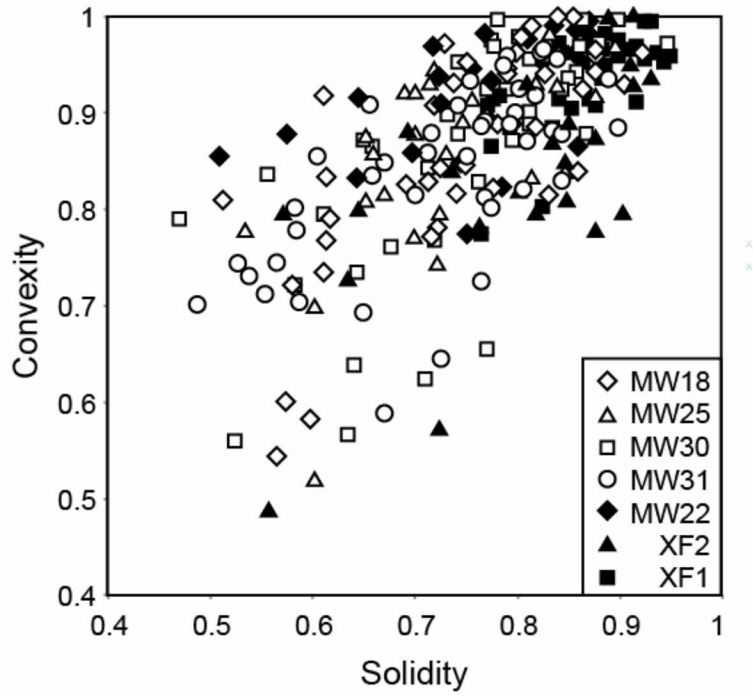
Figure B-6. The solidity and convexity of all bubbles in crystalline (closed symbols) and crystal-poor (open)

3.10 Appendix B Tables

Table B-1

Sample	T (°C)	P_f* (MPa)	Φ_b† (%)	Φ_{bcorr}§ (%)	Φ_x# (%)	$\log k_1$** (m^2)	$\log k_2$†† (m)
dP/dt = 0.125 MPa s^{-1}							
MW13	1000	85	1.9 (0.2)	7.68	17.2 (1.9)	N.D.##	N.D.
MW14	1000	100	3.5 (1.6)	11.37	25.9 (3.5)	N.D.	N.D.
MW16	1000	50	24.1 (0.3)	39.22	13.5 (3.9)	N.D.	N.D.
MW17	1000	25	45.7 (3.9)	62.75	26.3 (1.2)	-10.25	-6.93
MW18	1000	15	48.0 (3.4)	62.79	26.4 (0.7)	-12.06	-8.27
MW24	1000	25	37.4 (4.4)	54.44	26.8 (5.0)	-13.80	-10.52
MW26***	1000	30	37.6 (1.0)	58.30	31.5 (6.8)	-13.40	-10.03
MW32	989	10	55.7 (5.7)	68.30	30.6 (2.7)	-12.74	-7.97
MWXF1***	1014	25	33.6 (1.1)	50.23	17.9 (2.5)	N.D.	N.D.
MWXF6	1025	15	57.1 (1.5)	70.88	14.3 (2.8)	N.D.	N.D.
MWXF8	1025	20	36.4 (1.3)	52.98	35.3 (0.9)	-14.21	-10.34
MWXF10	1025	10	63.2 (2.8)	74.63	27.3 (6.7)	-10.02	-7.03

Table B-1 continued.

dP/dt = 0.083 MPa s^{-1}

MW19	1000	75	9.5 (0.8)	15.21	16.2 (1.7)	N.D.	N.D.
MW20	1000	100	23.0 (1.9)	13.35	23.4 (7.8)	N.D.	N.D.
MW21	1000	25	63.0 (1.0)	87.77	23.4 (3.5)	-10.71	-7.00
MW22	1000	40	14.9 (1.0)	42.16	15.0 (1.9)	N.D.	N.D.
MW25	1000	25	43.9 (3.9)	60.97	21.0 (3.3)	-12.44	-8.71
MW28[***]	989	15	55.5 (5.7)	69.54	18.6 (3.6)	-11.62	-8.64
MW29	989	15	39.8 (2.4)	54.73	24.1 (0.1)	-13.71	-10.94
MW30[***]	989	20	30.9 (4.7)	46.78	33.1 (0.5)	-12.88	-9.38
MW31	989	20	51.5 (3.0)	67.66	29.4 (4.1)	-12.65	-8.00
MWXF2[***]	1014	25	34.6 (4.0)	51.33	10.9 (3.7)	N.D.	N.D.
MWXF7	1025	15	39.7 (2.8)	54.63	21.0 (0.2)	N.D.	N.D.
MWXF9	1025	10	39.7 (2.4)	52.94	33.5 (1.8)	N.D.	N.D.
OK17	1025	15	2.9 (1.1)	5.17	Q[§§]	N.D.	N.D.
OK19	1025	15	21.2 (1.9)	32.96	Q	N.D.	N.D.

[*] Final quench pressure.

[†] Volume percent bubbles.

[§] Corrected volume percent bubbles (Marxer et al., 2015).

[#] Volume percent microlites.

[**] Darcian permeability: maximum standard deviation of 0.2 log units.

[††] Non-darcian permeability: maximum standard deviation of 0.6 log units.

[§§] Experiments are crystal free with the exception of quench crystals.

[##] Permeability is below the detection limit of the permeameter (log k_1 = -15).

[***] High-resolution X-ray Computed microtomography scans.

Chapter 4 The influence of microlites and phenocrysts on eruption dynamics of the 2008 eruption of Kasatochi Island Volcano, Aleutian Islands, AK[1]

4.1 Abstract

The 7-8 August 2008 eruption of Kasatochi Volcano produced voluminous pyroclastic flows that blanketed and expanded the area of the island. These pyroclastic flows also contained juvenile pumiceous clasts with a wide variety of both compositions and textures. Three lithologies represent the clasts: andesite (58-62 wt. %), basaltic andesite (52-56 wt. %) and a mixture of both (banded) (Neill 2013). The three lithologies have connected vesicularities that span from $17 - 70.4$ vol.%. Andesite clasts exhibit relatively higher vesicularities (45.5-70.4 vol.%) within this range, while basaltic andesites make up the lower portion (30.0-50.7 vol.%). Despite having varying connected vesicularities, Darcian permeabilities of the clasts are fairly similar between $\log k_1 = -13.1 \pm 1$ m^2 to -10.9 ± 1 m^2. Microlite crystallinities range from <1 vol.% to 45.8 ± 6 vol.% and phenocryst crystallinities from 1 vol.% to 30 vol.%. The presence of both microlites and phenocrysts has a measured effect on permeability primarily due to increased pore sizes. Permeabilities are lower in samples with less than ~25 vol.% microlites and/or ~10 vol.% phenocrysts. Tortuosity measurements range between $\tau = 7.5 - 24.9$, formation factors between $F = 13.2$-60.4, and Archie's exponents between $m = 2.9$-22.7. Vesiculartiy, permeability, and electrical properties reveal overall trends that are unaffected by magma composition. Darcian permeability decreases as a function of increasing tortuosity. Archie's exponent increases with increasing vesicularity. Regardless of magma composition, the cause for these trends is due to the presence of crystals. We propose Kasatochi magmas were above random close packing and capable of causing the magma to "lock". The first three explosions were caused by brittle failure due to the large overpressures generated within the locked magma. Alternatively, stratification of crystal-poor and crystal-rich magmas within the conduit may have prevented gas migration and degassing, which would also generate large overpressures to fuel the explosive eruptions. The continuous phase of the eruption was due to outgassing via the gas-fracture regime.

---

[1] Lindoo, A., Tasa, K., Larsen, J.F., Neill, O.K., The influence of microlites and phenocrysts on eruption dynamics of the 2008 eruption of Kasatochi Island Volcano, Aleutian Islands, AK: prepared for submission to Bulletin of Volcanology.

4.2 Introduction

On August 7th and 8th 2008, Kasatochi Volcano, an island stratovolcano located in the Central Aleutian Islands, erupted explosively and unexpectedly (Fig. 4.1). This was the first historically documented eruption from Kasatochi, and caused far-reaching effects including a sulfur dioxide cloud that travelled as far east as Siberia over the course of a week (Krotkov et al. 2010). The eruption consisted of three major explosive events and two smaller events over the course of a day, producing a bulk eruptive volume and ash cloud height consistent with VEI = 4 (Waythomas et al., 2010). An earthquake swarm and resultant faulting around the edifice provided pathways for magma ascent (Ruppert et al., 2011). Pyroclastic flows buried the island, extending its 3 km diameter by ~30%. Waythomas et al. (2010) recognized four major units in the stratigraphic sequence: (1) A thin and muddy tephra deposit, (2) pumiceous pyroclastic flow deposits containing un-charred vegetation in lower layers, (3) lithic-rich pyroclastic flow, fall, and surge deposits, and (4) pyroclastic surge and fall deposits. The units also contained both compositionally and texturally diverse juvenile clasts, ranging from basaltic andesite (52-56 wt. %) to andesite (58-62 wt. %), with some clasts containing a banded mix of both end members. Basaltic andesite clasts have higher bulk densities (36.2-59.7 vol.% vesicularity), while more andesite clasts are more vesicular (50.9-81.7 vol.%). The basaltic andesites are more crystal-rich (21.4 – 77.3 vol.% total crystallinities) than the andesites (6.3-60.6 vol.%), especially in terms of groundmass crystallinity; groundmasses of andesite clasts may be nearly crystal-free, unlike the microlite-rich groundmasses of the basaltic andesite clasts (18.4-47.8 vol.%). Furthermore, proportions of dense and vesicular material vary throughout the eruption (Neill, 2013). The textural and lithological heterogeneity observed over the course of this eruption provides a unique opportunity to correlate with eruption styles.

In this study, we focus on variations between andesite and basaltic andesite juvenile clasts that may provide information about transitions in eruptive style. We quantitatively compare the vesicle and crystal textures, permeabilities, and electrical tortuosities between the two endmember lithologies erupted from Kasatochi to provide a better understanding of coupled processes of crystallization and vesiculation during magma ascent. We present one of the first studies to combine direct bulk measurements of connected vesicularity, permeability, and tortuosity paired with calculations of phenocryst and microlite crystallinities to examine whether differences in magma compositions and/or textural components influenced permeability

development and degassing efficiency. Finally, we compare our observations with experimental, analog and numerical datasets to describe the mechanisms behind changes in intensity during the 2008 eruption of Kasatochi volcano.

4.3 Background

Transition between effusive and explosive activity has been explained through myriad mechanisms including changes in ascent rate, which ultimately controls time allotted for gas segregation (i.e. Pioli et al., 2009) and/or the ability of magmas to develop permeable pathways (i.e. Polacci et al., 2008; Polacci et al., 2009). Volatile exsolution in magmas is the primary driving force for magma ascent. Magmas are invariably enriched in gases, such as H_2O, CO_2, and SO_2. The amount of each gas dissolved in the melt (solubility) is dependent on the melt composition, pressure and temperature. For H_2O, solubility decreases as a function of decreasing pressure. Therefore, when magma ascends, H_2O exsolves from the melt in the form of bubbles. The bubbles grow by diffusion of H_2O molecules to the melt-bubble interface along with decompression growth caused by hydrostatic changes in pressure during ascent (Sparks, 1978; Proussevitch et al., 1993). As the vesicularity of the melt increases, bubbles interact with each other. Melt films between bubbles and their neighbors thin during expansion and ultimately rupture, connecting bubbles via a small pore aperture. Myriad bubbles may connect (coalesce) together and form long chains of bubble networks that can extend through large portions of the magma. This marks the development of a permeable network by which the magma may degas. Previous studies propose that the development of permeability within rising magma results in effusive or less intense eruptions (e.g., Eichelberger et al., 1986, Westrich and Eichelberger, 1994, Klug and Cashman, 2002, Rust and Cashman, 2004, Takeuchi et al., 2009; Wright et al., 2009). In order for Plinian eruptions to occur, high gas overpressures must develop within the magma; resulting in brittle fragmentation (Houghton and Gonnermann, 2008; Sable et al., 2009).

Previous studies focused on crystal-free analog and decompression experiments have determined the percolation threshold, the vesicularity at which magma becomes permeable, to occur at approximately 70 vol.% vesicularity (Namiki and Manga, 2008; Takeuchi et al., 2009; Lindoo et al., 2016). However, in crystalline magmas the percolation threshold may be much lower, ≤ 45 vol.% (Saar and Manga, 1999; Mueller et al., 2005; Chapter 2). Studies have also relied mostly on indirect measurements from 2D images to infer geometries of pore pathways.

The porosity-permeability relationships reported show larger scatter between the different datasets, due to the fact the porosity (vesicularity) is not a main controlling factor for permeability development. Instead, pore size, shape, and roughness as well as hydraulic radii connecting different pores primarily controls magma permeability (Bernard et al., 2007; Wright et al., 2006; 2009). Some studies have incorporated the use of 3D X-ray microtomography to produce essentially CT scans of eruptive materials (Polacci et al., 2008; Bai et al., 2010; Degruyter et al., 2010; Bai et al., 2011). However, the large voxel resolutions (~13 μm^3) of these images prevent accurate determination of small pore pathways or pore apertures. Hence, tortuosity measurements are an invaluable addition to this particular data set. Many studies have analyzed porosity-permeability relationships within natural samples; however, few also report crystallinities, especially microlite contents. Recent experimental data has highlighted the influence of microlites on permeability development (Lindoo et al., 2017). In crystalline experiments, permeability occurs after ~20 vol.% crystals are present. The crystals lower the percolation threshold of the magma by promoting bubble deformation likely via particle-particle interactions, which initiate the onset of yield strength in the magma (Lindoo et al., 2017). Therefore, it is essential that crystallinities be incorporated into degassing and eruption models.

Crystallinities observed in Kasatochi andesite and basaltic andesite can exceed ~50 vol.% At such high crystallinities, magmas begin to approach random closest packing (RCP). At RCP crystals are capable of jamming and forming a rigid network capable of transmitting stress (Oppenheimer et al., 2015; Pistone et al., 2015). At this threshold, two gas migration regimes may occur: gas-induced fracturing or gas-driven filter pressing. Both require a delicate rheological balance within the magma. It must not be too deformable or too rigid, a condition that ultimately depends on the amount of melt left in the suspension (Pistone et al., 2015). Regardless of the regime, the transition crystallinity also depends on aspect ratio and crystal size. Smaller crystals tend to favor bubble deformation and/or the gas-fracture regime even at high crystallinities (Mueller et al., 2011; Oppenheimer et al., 2015; Spina et al.,2016; Lindoo et al., 2017).

4.4 Methods

Subsets of 32 juvenile clasts, selected from 1016 samples collected from the 2008 Kasatochi eruption, were examined to quantitatively compare erupted lithologies (Table 1). The

key parameters used to understand mechanisms of degassing within the andesite, basaltic andesite and banded clasts were bubble volume percent (vesicularity), crystal volume percent (crystallinity), permeability and tortuosity.

4.4.1 Clast densities and vesicularity measurements

Bulk clast densities and vesicularities were measured using the method of Houghton and Wilson (1989), which employs Archimedes principle. Dry clasts were weighed in air then wrapped in two sheets of Parafilm and weighed while submerged in water. The specific gravities of each clast, ratio of weight in air versus its weight in water, were used to calculate bulk densities (open and closed pores). The bulk densities were then compared with the Dense Rock Equivalent (DRE) to determine vesicularity. Connected vesicularities were derived from skeletal density measurements made with a HumiPyc II He pycnometer at the University of Alaska Fairbanks Experimental Petrology lab. The pycnometer operates by exploiting the ideal gas law, $PV=nRT$. The measurements were conducted under constant pressure with no net loss or gain of gas molecules (nRT=constant). The pycnometer consists of two chambers of known volumes that are connected by a valve. Each clast was placed within the sample chamber and the gas pycnometer detected pressure changes resulting from the displacement of gas by the object. Three repeat measurements were performed on each clast to determine precisions of $\pm$ 2% and $\pm$ 1% for bulk density and connected vesicularity measurements, respectively.

4.4.2 Analytical techniques

Back-Scattered Electron (BSE) images were collected from carbon-coated thin sections of 20 clasts using the University of Alaska Fairbanks Advanced Instrumentation Laboratory (AIL) JEOL JXA-8530F electron microprobe. A 15 KeV and 10 nA scanning beam was used to collect 25 BSE images per thin section. Image magnifications were based on a 15-image nest strategy outlined in Shea et al. (2010b). Each set of BSE images includes 1,3,6, and 12 images at the following magnifications: 40x, 150x, 300x and 500x, respectively. The magnification range was chosen based on the largest and smallest vesicles observed in the natural samples. Three extra images per sample were captured at 1000x magnification to resolve microlite contents and textures.

4.4.3 Crystallinity

Image processing techniques were performed on all of the BSE images according to the image segmentation guide included with FOAMs, a Matlab-based algorithm for bubble texture analysis (Shea et al., 2010b). Three phases (crystals, bubbles, and glass) were thresholded, segmented and converted into uniform gray-scale colors in Adobe Photoshop. Plagioclase microlites had similar mean atomic numbers as the surrounding glass and therefore had to be manually traced. The images were then input into NIH-ImageJ program to measure crystallinity calculated on a vesicle-free basis along with crystal aspect ratio using a best-fit ellipsoid method. From this information we calculated N_a, microlite number density (mm^{-2}), by dividing the total number of crystals in a region of interest by the area of the groundmass in that region. Aspect ratios were calculated by determining the major and minor axis from a best-fit ellipse. The values were input into an excel spreadsheet, CSDSlice (Morgan and Jerram, 2006), which compares the major/minor axes to a database to determine the best fit aspect ratio for the overall crystal population. Phenocryst vesicularity was determined through point counting (1000 points per slide) and error determined using the Van der Plas and Tobi equation (1965).

4.4.4 Permeability measurement

In order to quantify the ability of gas to flow through bubble networks, we measured permeability using a bench-top gas permeameter built at University of Alaska Fairbanks following the design of Takeuchi et al. (2008). The clasts were shaped into cylindrical cores (approximately 20 mm in diameter and no longer than 20 mm) to fit into a core holder. Airflow was controlled through the sample using a CKD pressure regulator to between 0.005 and 0.1 MPa to create a pressure gradient upstream and downstream of the sample holder. The resulting pressure differential was measured with a Testo 526 digital manometer to between -1 to -980 hPa. Gas flow rates between 1 and 625 mL/min were measured with a digital mass flow meter (Omega FMA-4100/4300).

Conventionally, permeability is measured using Darcy's law, which relates the fluid velocity through a medium to its permeability and pressure (Ruth and Ma, 1992):

$$Q = kA \frac{\Delta P}{l} \tag{4.1}$$

Where (Q) is the flow rate, (k) is the permeability, (A) the cross-sectional area, and (ΔP) the pressure differential over length (l). Darcy's law is best applied to low velocity systems that exhibit laminar flow. At low Reynolds number flow (Re <1), the fluid flow rate varies proportionally with the pressure gradient. At high Reynolds number flow (Re > 1), inertial forces become dominant over laminar forces resulting in turbulence. Inertial effects cause viscous dissipation as flow rate increases resulting in a non-linear relationship between fluid velocity and the pressure gradient (Jaupart and Allegre, 1991; Rust and Cashman, 2004). The transition of laminar to turbulent flow is dependent on the gas viscosity, velocity, and pathway size through which it travels. In pumices, the flow pathway is dictated by bubble aperture diameters. Because bubble pathways in pyroclasts are typically tortuous, consideration of turbulent flow is required. Therefore we use the Forchheimer equation to describe the Darcian (k_1) and inertial (k_2) permeabilities of our samples (Rust and Cashman, 2004):

$$\frac{P_2^2 - P_1^2}{2P_0 l} = \frac{\mu}{k_1} v + \frac{\rho}{k_2} v^2 \tag{4.2}$$

Where P_2 and P_1 are the pressures upstream and downstream of the sample and P_0 the pressure where gas volume flux (v) is measured. l is the length of the sample, μ the viscosity and ρ, the density of air. Permeabilities (k_1 and k_2) were determined by fitting a second order polynomial to the calculated modified pressure gradient and gas volume flux derived from permeability measurements (Fig. 4.2, Rust and Cashman, 2004; Takeuchi et al., 2008). At least three analyses were performed on each sample to determine reproducibility. The repeat measurement produced standard deviations no larger than 0.17 log units (k_1) and 0.28 log units (k_2).

4.4.5 Tortuosity measurement

Electrical conductivity is a measurement of how well a medium transports an electrical charge (Wright et al., 2009). By exploiting the fact that rocks are pore conductors, the conductivity of fluid forced into pore space can be measured. Tortuosity (τ) provides a quantitative description of the structure of porous media (Le Pennec et al., 2001; Wright et al., 2009). The connected pathways that enable permeability development vary depending on bubble

73

shapes and pore throat sizes. Electrical tortuosity is essentially the average path length for electrical flow divided by the straight-line length. Tortuosity can be inferred by measuring the resistivity of a material as a product of its connected vesicularity (Φ) and formation factor (F) (Ghanbarian et al., 2013): $\tau = \Phi F$. The dimensionless formation factor is the quotient of the conductivity of a saturating fluid and the bulk electrical conductivity of the sample. The formation factor alone can be used to describe a porous medium with the relationship (Archie, 1942):

$$F = \Phi^{-m} \tag{4.3}$$

With Archie's exponent (m) varying depending on pore shape, size and roughness. The relationship between formation factor and permeability,

$$k_1 = lF^{-n} \tag{4.4}$$

can be used to describe the geometry of an interconnected channel with the exponent of n (Walsh and Brace, 1984; Wright et al., 2009). When flow paths are relatively straight (i.e. tube pumice), n approaches 1. Alternatively, n will reach values of 2 or 3 when pathway geometry is more complex. Furthermore, pore diameter size of the largest percolating pathway can also be estimated using the relationship of permeability and formation factor (Kats and Thompson, 1986):

$$k_1 = \frac{l_c^2}{c_2 F} \tag{4.5}$$

Electrical conductivity was measured on 21 out of 32 cores by saturating the samples in 5 NaCl brines of increasing salinity over the course of approximately 8 hours. The samples were soaked under vacuum in de-ionized water for 24 hours before placing the cores into an air pressurized sample holder (Fig. 4.3). A pump circulated solutions of increasing salinity through the samples over the time period. After each addition of NaCl to the solution, we measured the sample resistivity using an Instek 821 LCR meter after approximately 1-2 hours of stabilization

time. The conductivity of the solution was measured using an Oakton Acorn 6 conductivity meter and at each time and salinity step sample resistivity was measured (Fig. 4.4). The amount of time in between each addition of NaCl was dependent on the permeability of the sample. Samples that were less permeable took much longer for the NaCl solution to saturate the sample and therefore a longer equilibration time before more NaCl could be added. Tortuosity on some samples with relatively low permeability could not be measured due to the long equilibration time required. If left for long periods of time to equilibrate, the solution would begin to evaporate and errors in the measurements increase (Wright et al., 2009). We conducted two repeat measurements on three samples from the subset and found the precision to be ± 10% of the tortuosity value.

4.5 Results

In hand sample, the basaltic andesite clasts appear denser, while andesite clasts are more vesicular. Bulk clast density (measured by Owen Neill after Houghton and Wilson, 1989) varies widely and shows a bimodal distribution with respect to silica content (Fig. 4.5). Basaltic andesites have higher bulk densities (1700 - 2600 kg m^{-3}), and andesite clasts have lower bulk densities (650 -1700 kg m^{-3}), with banded samples falling in between (Fig. 4.5). Basaltic andesite clasts appear to be more crystal-rich than andesite clasts, especially in terms of groundmass crystallinity. They also contain a relatively consistent amount of phenocrysts compared to andesite and banded clasts. To further compare the different lithologies, we present their bulk properties determined from the above methodologies (Table 4.2)

4.5.1 Connected vesicularity and bubble texture

In general, andesite clasts have the highest connected vesicularities of the three lithologies, ranging between 44.8 vol.% to 70.4 vol.% (Table 4.2). Andesite clasts (Fig. 4.6-A, B) show a wide variety of bubble textures. Clasts range from having large vesicles with thin bubble walls (Fig. 4.6-A) to sub-spherical and irregular bubble shapes, likely due to interaction with microphenocrysts and groundmass crystals (Fig. 4.6-B). Basaltic andesite clasts have lower connected vesicularities than the andesites, ranging from 30.0 vol.% to 50.7, one sample at 59.7 vol.% (Table 4.2). Basaltic andesite clasts (Fig. 4.6-C) have smaller, irregularly shaped vesicles with thicker walls (Fig. 4.6-C, D). Coalesced bubbles within the samples have finger-like

vol.% (Table 4.2). Basaltic andesite clasts (Fig. 4.6-C) have smaller, irregularly shaped vesicles with thicker walls (Fig. 4.6-C, D). Coalesced bubbles within the samples have finger-like morphologies. The banded clasts have connected vesicularities that fall within the values determined for andesite and basaltic andesite lithologies, ranging from 30.7 vol.% to 64.9 vol.%, although one sample exhibits a very low connected vesicularity of 17.3 vol.% (Table 4.2). The banded clasts display bubble texture observations seen in both andesite and basaltic andesite clasts (Fig. 4.6-E, F).

4.5.2 Permeability

The permeabilities of andesite clasts increase with increasing connected vesicularities, especially > 60 vol.% (Fig. 4.7-A; Table 4.2). The samples range in Darcian permeability from $\log k_1 = -12.92 \pm 0.1$ m^2 to -10.94 ± 0.1 m^2 (Table 4.2). Inertial permeabilities are measured between $\log k_2 = -9.5 \pm 0.1$ to -7.6 ± 0.2 m. The permeabilities of basaltic andesite clasts are low relative to the andesites, with $\log k_1 = -13.46 \pm 0.1$ to -11.72 ± 0.4 m^2 and $\log k_2 = -9.5 \pm 0.4$ to -8.3 m. The basaltic andesite clasts gradually increase in permeability with increasing vesicularity. Banded clasts Darcian permeabilities are between $\log k_1 = -13.10 \pm 0.1$ to -11.93 ± 0.2 m^2 and inertial permeabilities from $\log k_2 = -9.2 \pm 0.1$ to -7.7 ± 0.7 m. There is no obvious increase in permeability as a function of connected veiscularity. Despite some clasts having relatively lower vesicularities (17 – 30 vol.%), permeabilities are similar to clasts with higher vesicularities (Fig. 4.7-A).

4.5.3 Electrical properties

Tortuosity values of all three lithologies do not vary with increasing vesicularity (Fig. 4.7-C; Table 2). However, general relationships are evident and show no dependence on lithology. Overall, tortuosity (τ) decreases as a function of increasing permeability (k_1) (Fig. 4.7-D), Archie's exponent (m) increases as a function of vesicularity, and permeability increases as a function of F^{-1}. Tortuosity measurements of andesites span, $\tau = 9 - 15$, and one sample (14-2) at $\tau = 24.9$ (Fig. 4.7-C, Table 4.2). The formation factors are grouped between $F = 13.2 - 33.9$, although one sample has a higher $F = 52.4$. From our tortuosity measurements, we iteratively solved for Archie's exponent for each of the samples using the relationship in equation 4.3 (Fig. 4.7-E). High values of m indicate large variations in pore sizes, whereas low values suggest pores

are more similar to micro-cracks or fissures (Bernard et al., 2007). Archie's exponent separates the andesite clasts into two groups: the first group, $m = 4.4 - 5.3$ and the second $m = 7.1 - 7.4$. The exponents correspond to differing connected vesicularities of $44.8 - 50.8$ vol.% and $62.0 - 60.4$ vol.%, respectively (Fig. 4.7-E). Basaltic andesite tortuosities are between $\tau = 9.1 - 16.8$ and formation factors between $F = 23.3 - 38$ (Fig. 4.7-C). One sample reaches a relatively high F of 56.6 despite having a similar tortuosity to other samples. Archie's exponents range from $m = 3.3 - 5.1$ (Fig. 4.7-E). Banded tortuosity measurements span, $\tau = 7.5 - 23.3$ (Fig. 4.7-C, Table 2). The formation factors are grouped between $F = 15.3 - 24.2$ and $F = 35.7$ to 53.4. Archie's exponents range from $m = 2.7 - 7.4$ (Fig. 4.7-E). The sample with the lowest connected vesicularity also has the lowest tortuosity of the set at $\tau = 3.05$, and corresponding formation factor and Archie's exponent of $F = 17.63$ and $m = 1.6$, respectively (Table 4.2).

4.5.4 Phenocryst and microlite crystallinities

Microlite crystallinities of the andesite vary from $\Phi \leq 1$ vol.% to as much as 43 ± 3 vol.% (Table 4.3). Errors in crystallinity are due to heterogeneity within the samples. The predominant microlite phase is feldspar ($\Phi \leq 1 - 38.0 \pm 3$ vol.%), followed by clinopyroxene ($\Phi \leq 1 - 8.0 \pm 3$ vol.%) and then iron-oxides ($\Phi \leq 1$ vol.%). Plagioclase crystals display mostly euhedral, tabular shapes with some hopper and rare skeletal morphologies. Clinopyroxene microlites also appear tabular in most of the andesite clasts analyzed (Table 4.3). Phenocryst crystallinities are highly variable within the andesite clasts, from $\Phi = 3.5 - 37$ vol.%. The phenocrysts are dominantly plagioclase ($1.3 - 12.4 \pm 1.1$ vol.%) with $0 - 4 \pm 0.5$ vol.% clinopyroxene, hornblende and iron oxides (Table 4.3). The microlite crystallinities of the basaltic andesite clasts are consistently between $\Phi \approx 27 \pm 5$ vol.% to 45.8 ± 6 vol.%, with the exception of one clast that had $\Phi \leq 1$ vol.% (Table 3). Plagioclase dominates the groundmass ($\Phi = 25.6 \pm 12 - 40.5 \pm 24$ vol.%), however their morphologies are euhedral and more blocky than in the andesite clasts (Table 4.3). Clinopyroxene ($4.2 \pm 1 - 18.2$ vol.%) also displays euhedral, blocky morphology. Phenocrysts are also consistently abundant throughout ($\Phi = 17.9 - 30$ vol.%) with $12.9 - 19.8 \pm 1.6$ vol.% plagioclase, $1 - 9.7 \pm 1.7$ vol.% clinopyroxene, and $0 - 1.2 \pm 1.1$ vol.% hornblende or iron oxides (Table 4.3). Crystal textures within the banded clasts contain a mixture of textures observed in the andesite and basaltic andesite clasts (Table 4.3). Vesicular clasts with few microlites are

Permeability, vesicularity, Archie's exponent, and pore diameter show a dependence on the amount of microlite and/or phenocryst crystals present (Fig. 4.8). Darcian permeability begins to increase from $\log k_1 = -12.7 \pm 0.2$ to $\log k_1 = -12.0 \pm 0.02$ shortly after ~ 20 vol.% microlites are present (Fig. 4.8-A). Permeability appears to increase as a function of phenocryst content, although the data are more scattered (Fig. 4.8-B). A general increase in connected vesicularity corresponding to an increase in microlite content can be seen in the basaltic andesite samples (Fig. 4.8-C). This appears to also be the case with the addition of phenocrysts, best noted by the andesite samples, where at $\Phi = 5.3$ vol.%, bubble vol.% = 50.8 ± 1. At $\Phi = 37$ vol.%, bubble vol.% = 70.4 ± 1.4 (Fig. 4.8-D). There is no obvious relationship between microlite crystallinity and m; however, andesite samples show an overall increase in m with increasing phenocryst content (Fig. 4.8-E, F).

4.6 Discussion

4.6.1 Bulk properties of eruptive products

The permeabilities of the samples follow similar trends seen in previous studies and can be described using the fully penetrable sphere (FPS) model, based on percolation theory of overlapping mono-disperse spheres (Fig. 4.7-A, B; Carman, 1956; Sahimi, 1994, Saar and Manga, 1999 Rust and Cashman, 2004; Wright et al., 2006; Wright et al., 2007; Wright et al., 2009). The FPS model describes the evolution of permeability as a power-law trend:

$$k(\Phi) = C(\Phi - \Phi_{cr})^{\mu} \tag{4.6}$$

where C is the magnitude of permeability, Φ_{cr} is the critical vesicularity at which magma becomes permeable (percolation threshold), and μ is an exponent related to pathway geometry. In trends a and b, we set $\Phi_{cr} = $ to 40 vol.%; similar to the percolation threshold defined from crystal-rich experiments and scoria (Mueller et al., 2005; Chapter 2). We set μ to 3.8 and 3 for trends a and b, respectively (Mueller et al., 2005). Trend c uses a percolation threshold of 30 vol.% defined by Sahimi (1994) and $\mu = 2.5$. The andesites appear to follow trend b, where permeability ($\log k_1$) increases slowly with increasing connected vesicularity until $\Phi = $ to 70 vol.% (Fig. 4.7-B). Basaltic andesites follow trend a, where permeability increases quickly (relative to the andesites) as vesicularity increases. Banded samples follow trend c albeit with

considerable deviations to lower vesicularities. Data from the study of Wright et al. (2009) follow trend c as well, with the exception of tube pumice samples (diamond symbols). The banded samples that drift to lower vesicularities (≤ 30 vol.%) while maintaining similar permeabilities (log $k_1 \approx -12.5$ m^2) are an example of the limitations of percolation theory. Although percolation theory is often used for describing and comparing porous media, the relationship is unable to account for large variations in bubble geometries, shear stress or the influence of crystals (Rust and Cashman, 2011).

Apart from compositional trends seen in vesicularity-permeability relationships, trends in other bulk parameters are independent of lithology. This also appears to be the case in previous studies plotted along with Kasatochi data, with the exception of tube pumice (Fig. 4.7-A, B); Rust and Cashman, 2004; Wright et al., 2006; 2007; 2009). We find a definite correlation between increasing permeability and decreasing tortuosity in all of the samples (Fig. 4.7-D). As pathway geometries simplify within magma (decreasing tortuosity), gas can efficiently move through the system and permeability increases (Bernard et al., 2007; Wright et al., 2009). Interestingly, inertial permeability (k_2), which is thought to describe the complexity of pore pathways, does not show a relationship to tortuosity or other parameters. Archie's exponent (m) increases linearly as a function of vesicularity (Fig. 4.7-E), which implies that although vesicles are becoming more connected, few pathways are actually involved in degassing (Bernard et al., 2007). Furthermore, we see a positive correlation between $1/F$ and increasing permeability (Fig. 4.7-F). The lack of compositional trends in this data echoes the results of decompression experiments that indeed, melt viscosity does not have a control on degassing parameters (Lindoo et al., 2016).

4.6.2 The control of crystals

Microlites exert a profound influence on permeability development in low viscosity magmas. After the addition of approximately 20 vol.% microlites, the percolation threshold decreases (Lindoo et al., 2017). This is primarily due to an overall morphological change in bubble shapes throughout the magma at the onset of apparent yield strength caused by particle-particle interactions (Oppenheimer et al., 2015; Lindoo et al., 2016). Therefore, Kasatochi magmas and those similar (containing >20 vol.% microlites and phenocrysts), should be subject to crystal-controlled degassing regimes. Figure 4.9, modified from Lindoo et al. (2017),

illustrates the development of permeability once magmas contain approximately 20 vol.% microlites. The Kasatochi data are plotted on the graph and represented by black symbols with shapes corresponding to those used to denote different lithologies in previous figures. Unlike the experimental samples, all of the Kasatochi products are permeable, regardless of microlite content (Fig. 4.9). This could be due to many factors such as; the presence of phenocrysts, shear deformation, post—fragmentation processes, etc. We have drawn in diagonal lines to show their potential influence on the potential reduction in permeability.

By separating microlite and phenocryst data and comparing their relative amounts with bulk parameters, we see more distinct trends in how particles affect magma. The addition of microlites and phenocrysts both increase Darcian permeability (Fig. 4.8-A; B). Interestingly, permeability increases at microlite contents > 20 vol.% similar to what has been found in experiments (Lindoo et al., 2017). Samples containing < 20 vol.% phenocrysts, even negligible contents, show an increase in permeability (Fig. 4.8-B). As seen in Fig. 4.8, microlites do not appear to have a large effect on the overall vesicularity of the magma (Fig. 4.8-C). However, phenocrysts may have a slight influence, as seen in the weak trend in increasing vesicularity in figure 4.8-D. A similar trend is seen in m, specifically with the andesites, although there are just more of them. If m does in fact increase with increasing crystal (phenocryst) contents, this would suggest phenocrysts complicate pore pathway geometry by causing wide variations in pore sizes (Le Pennec et al., 2001). The addition of both microlites and phenocrysts increases the overall pore sizes found in the samples. This appears to be the direct cause for increase in permeabilities as similar relationships are found; pore geometries increase after approximately 20 vol.% microlites, yet only ~10 vol.% in phenocryst contents (Fig. 4.8-G, H). The increase in sample permeabilities is due to crystals enhancing the development of large vesicles; a product of crystal-induced bubble deformation promoting coalescence. To summarize, crystal content is the main influence on degassing parameters such as pathway morphology, pore geometry, and pore size. Furthermore, phenocrysts appear to influence these parameters at lower volume fractions than microlites. This would suggest that crystal size and/or pre-eruptive crystallization also play a role in permeability development.

4.6.3 Conditions leading to explosive behavior in magmas

Variations in eruption style are dependent on the ability of bubbles to migrate through crystal suspensions. Decompression and analog experiments provide evidence that the mechanism of bubble migration through magma changes at two rheological thresholds: the onset of yield strength (~20 vol.% crystals) and RCP (~54 vol.% crystals) (Oppenheimer et al., 2015, Lindoo et al., 2016). Andesite samples have a wide range of crystallinities, from ~ <1 to 48 vol.%, while basaltic andesite clasts contain a consistent amount of both microlites (>20 vol.%) and phenocrysts (>18 vol.%) (Table 4.3). Therefore, both magmas experienced a range of rheological conditions that could explain transitions in eruption intensity over the course of the eruption. We propose the pulsatory behavior of the eruption was caused by gas-fracture within highly crystalline magmas that provided efficient degassing pathways through an effectively "locked" magma body or a stratified crystal-poor/ crystal-rich magma.

At crystal contents > 40 vol.%, the Kasatochi magmas were likely above the RCP transition. If particle contents cross this boundary, the magma can become rheologically "locked" (Philpotts et al., 1999; Holtzman et al., 2012). At these conditions, gas bubbles are unable to percolate through the magma because the force of the crystals resisting displacement by the bubbles is greater than the force generated by bubbles undergoing expansion. As overpressure develops, the melt phase can be expelled from the crystalline region via gas-driven filter pressing (Sisson and Bacon, 1999; Pistone et al., 2015). Alternatively, gas may propagate through the mixture by fracturing the melt. The fracture regime is especially effective at gas release, due to the relatively straight pathway morphology of fractures (Oppenheimer et al., 2015). Some combination of the two may also occur, depending on the overpressure relative to inflation of the magma, crystal sizes, and melt volume (Pistone et al., 2015). While evidence of gas-driven filter pressing may be visible in eruption products, gas fractures are rarely observed preserved due to re-healing at the fracture site (Oppenheimer et al., 2015). No obvious textures suggesting gas-driven filter pressing have been found in the Kasatochi pyroclasts. Therefor we predict the fracture regime was the most dominant outgassing pathway, especially considering the small sizes of the microlites, and that this led to episodic gas release over the course of the eruption (Oppenheimer et al., 2015).

Alternatively, numerical models investigating stratification of crystal-free and crystal-rich magmas suggest crystal-free layers trap bubbles that had been previously mobilized by crystal-rich regions (Parmigiani et al., 2016). Stratification of crystal-rich vs. crystal-poor segments of andesite magma may also explain intense eruption pulses. Crystallinities of the basaltic andesite clasts are relatively consistent, promoting a healthy degassing environment throughout the entire parcel of magma. Despite degassing through gas-fracture, heterogeneity of crystals throughout an overlying andesite body may have prevented bubble escape. The high explosivity and fast cessation of each pulse may have been an alternating battle between bubble stagnation between crystal-poor and crystal-rich parcels (Parmigiani et al., 2016). This coupled with the high ascent rate (0.1-0.2 m s^{-1}) of the vesiculating magma may not have allowed the andesite time to release an appreciable amount of overpressure, which resulted in the explosive phases (Neill, 2013).

During later phases, the increase in microlites due to cooling- and decompression-induced crystallization would have also increased the apparent viscosity of the magma, resulting in a decrease in magma ascent rate; further allowing more time for degassing (Houghton et al., 2008). Although the crystals promoted degassing, electrical properties indicate permeable pathways were still complex enough that they may have inhibited rapid degassing. Therefore, this may have resulted in the relatively long period of degassing (~16 hrs) following the main explosive phases. Parcels of the mixed magmas or periods of magma locking may have interrupted this process and caused the lower intensity explosions later in the eruption. Concurrently, the magma was also likely able to release more gas through permeable conduit walls after three significant explosive events (Jaupart, 1996).

4.7 Summary

Bulk parameters investigated in this study, vesicularity, permeability, crystallinity, and tortuosity, provided evidence that variation in eruption intensities of the 2008 Kasatochi volcano eruption were caused by variations in crystal content and gas migration regimes. This was inferred from the comparison of pore diameter sizes calculated using tortuosity measurements with permeability measurements. Overall, total crystallinities of Kasatochi pyroclasts are very high (> 60 vol.%), regardless of the

lithology. Such high crystal contents likely hindered, or even prohibited, permeable outgassing (Pistone et al., 2015). Instead, we argue the magmas degassed via gas-fracture with intermittent episodes of quiescence due to crystal jamming or bubble stagnation (Sisson and Bacon, 1999; Oppenheimer et al., 2015; Pistone et al., 2015; Parmigiani et al., 2016). We suggest the trapping and release of bubbles within a nearly-"locked" magma resulted in pulsatory eruption phases. Later in the eruption, the apparent viscosity of the magma would have slowed ascent as well, allowing more time for degassing. This coupled with permeable wall rocks fractured during the first three explosive phases led to an overall decrease in eruption intensity. As a general application to other magmas, crystal content has a primary control on degassing mechanisms, regardless of magma composition. This finding highlights the importance of including crystallinity data in eruption models and the addition of crystal size, aspect ratio, etc. helpful for future studies.
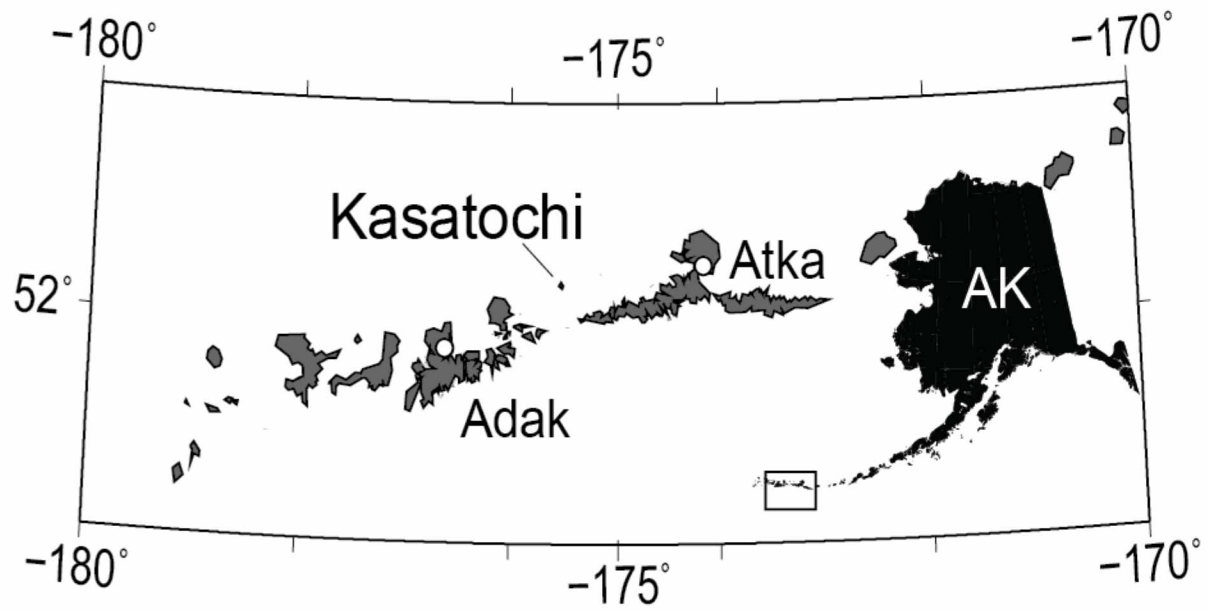
Figure 4.1: Location of Kasatochi Island volcano, Aleutian Islands, Alaska.
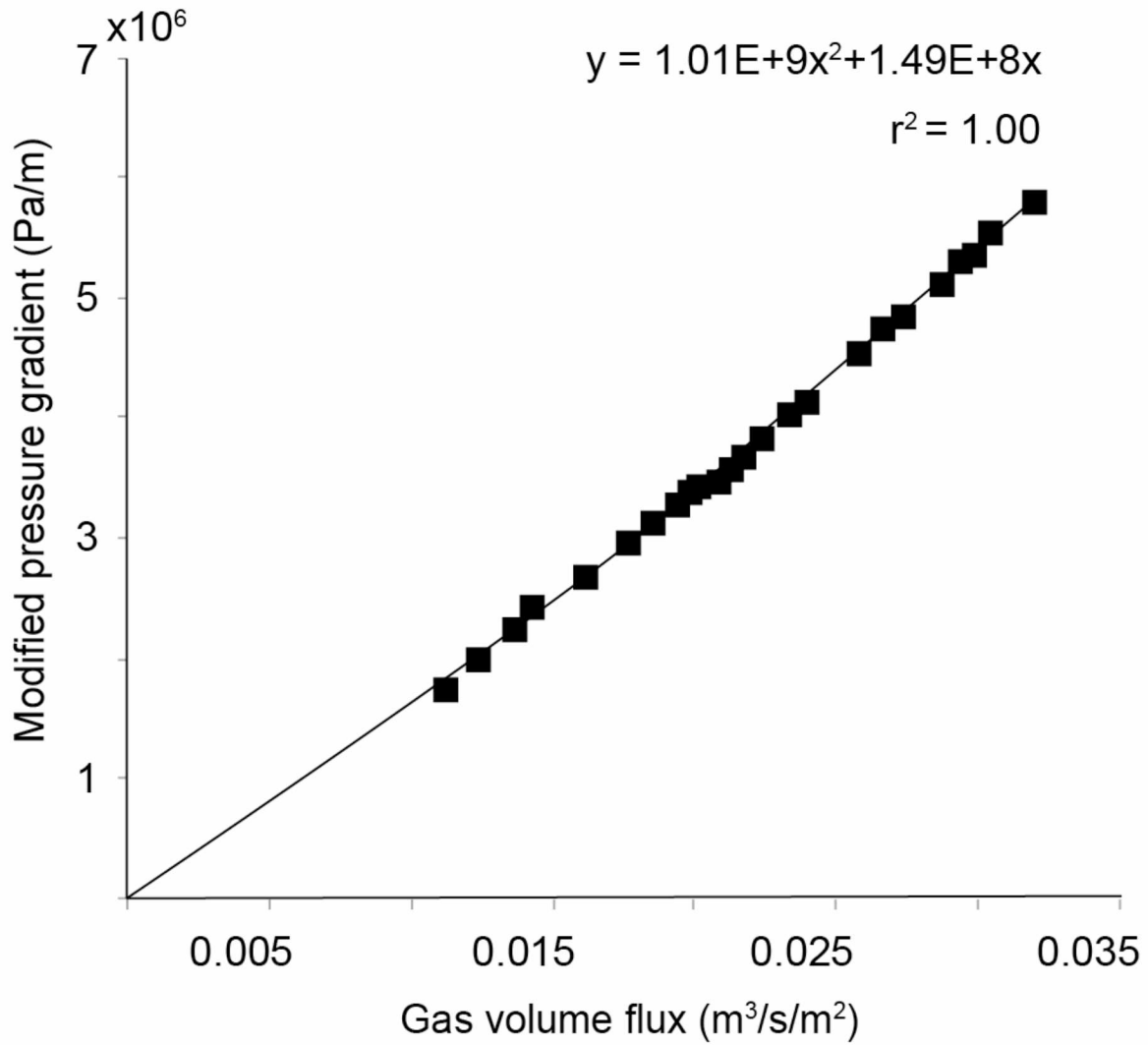
Figure 4.2: Second order polynomial fit to gas volume flux and modified pressure gradient values derived from gas flow and differential pressure measurements.
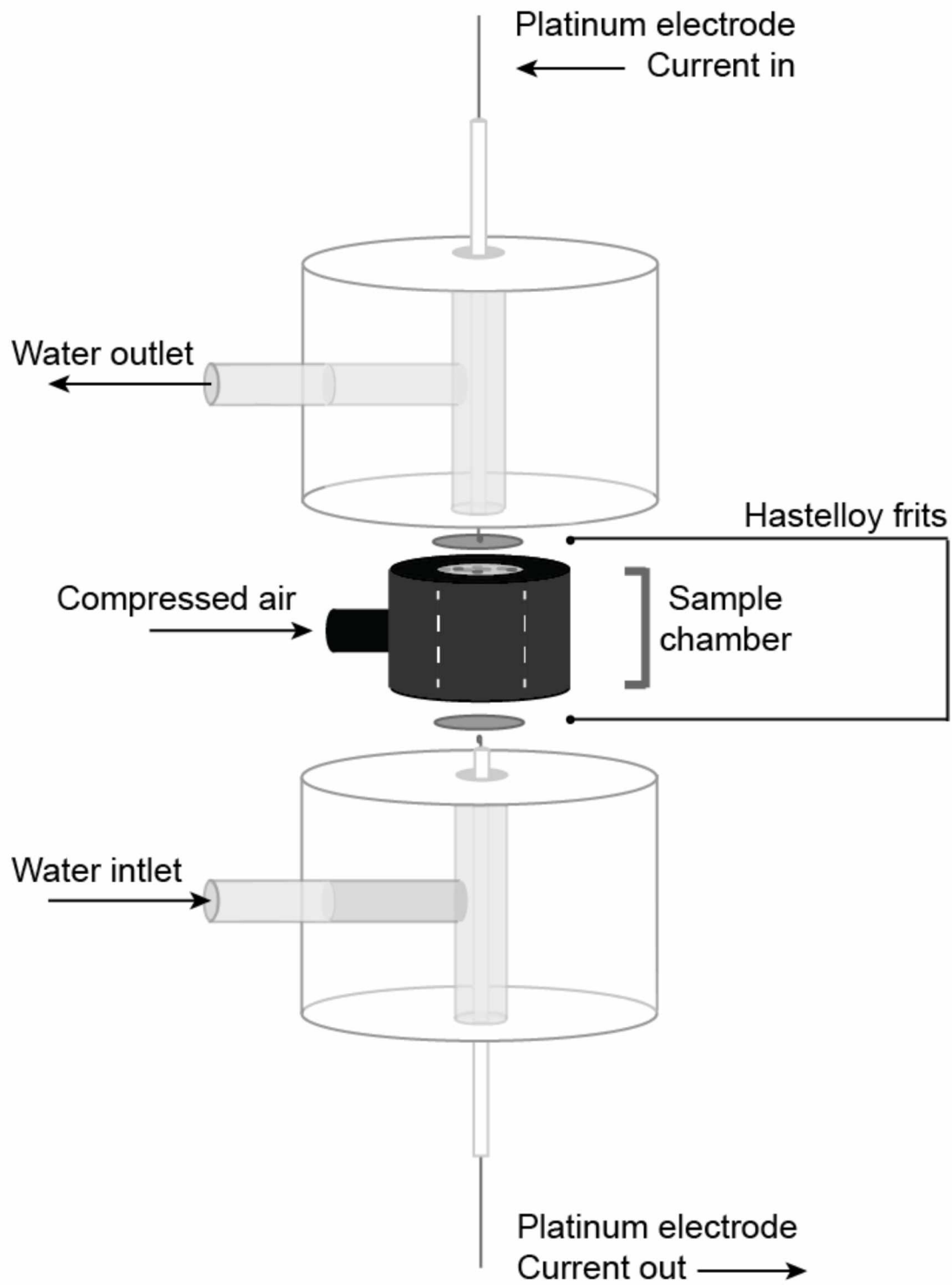
Figure 4.3: Device used to measure tortuosity. Design based off of Wright et al. (2009).
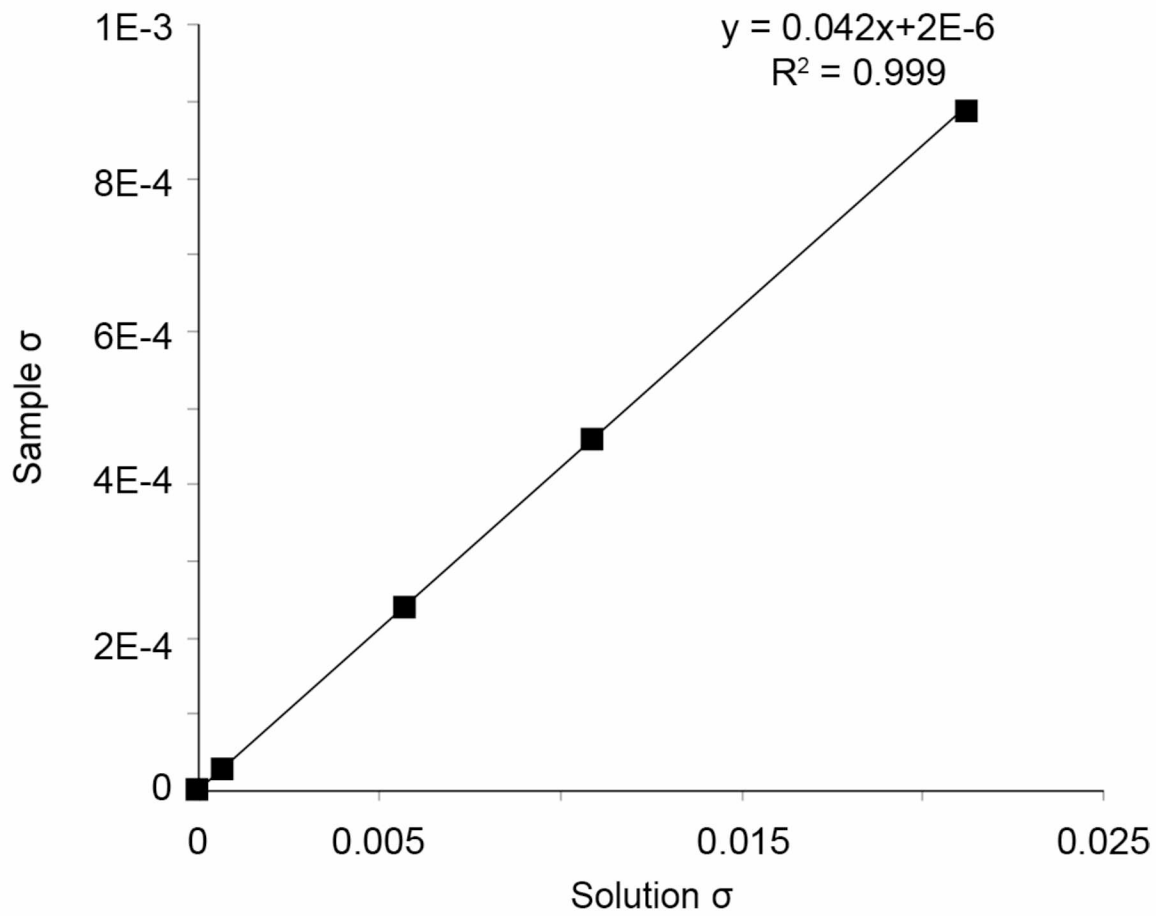
Figure 4.4: Sample conductivity as a function of conductivity of the saturating fluid.
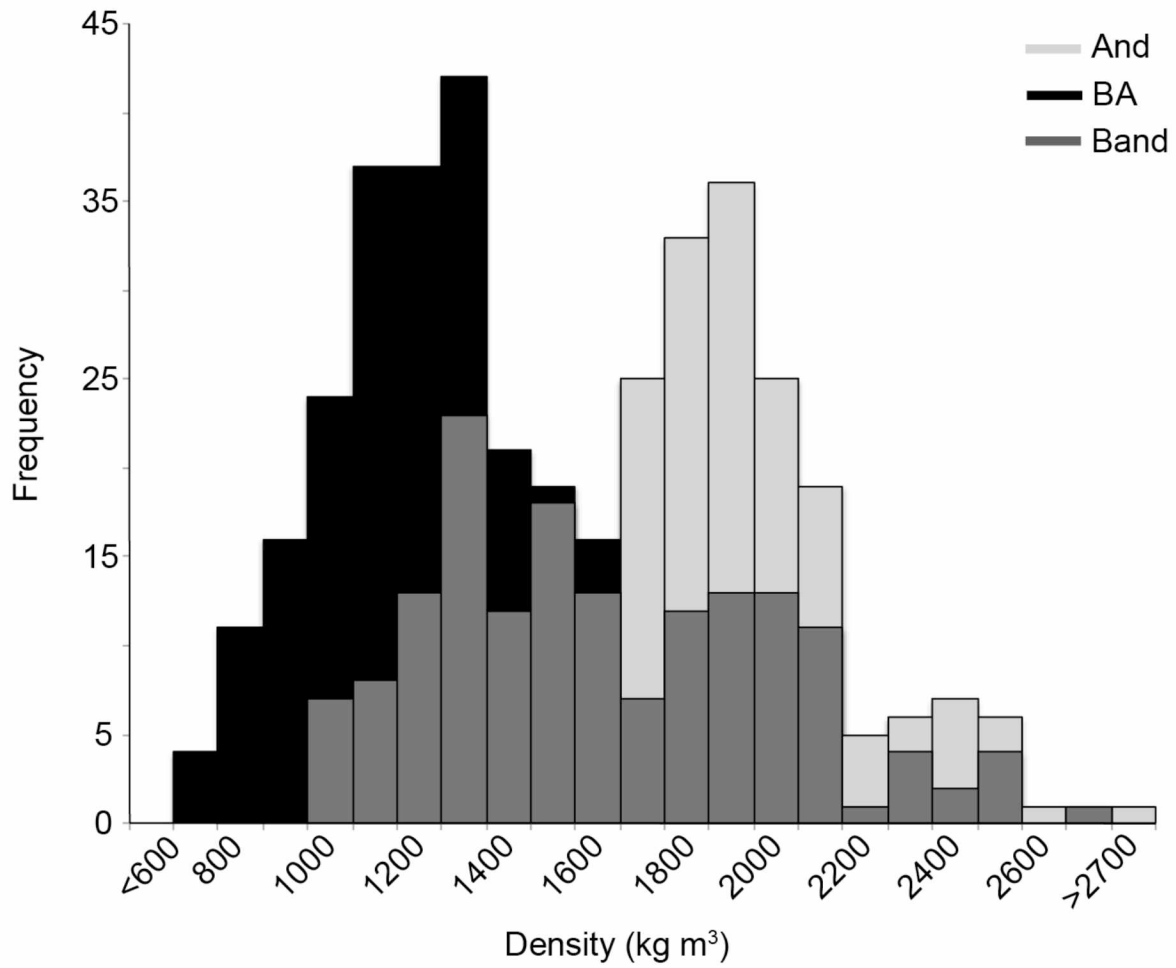
Figure 4.5: Bulk density histogram of andesite (And), basaltic andesite (BA), and banded (Band) clasts.
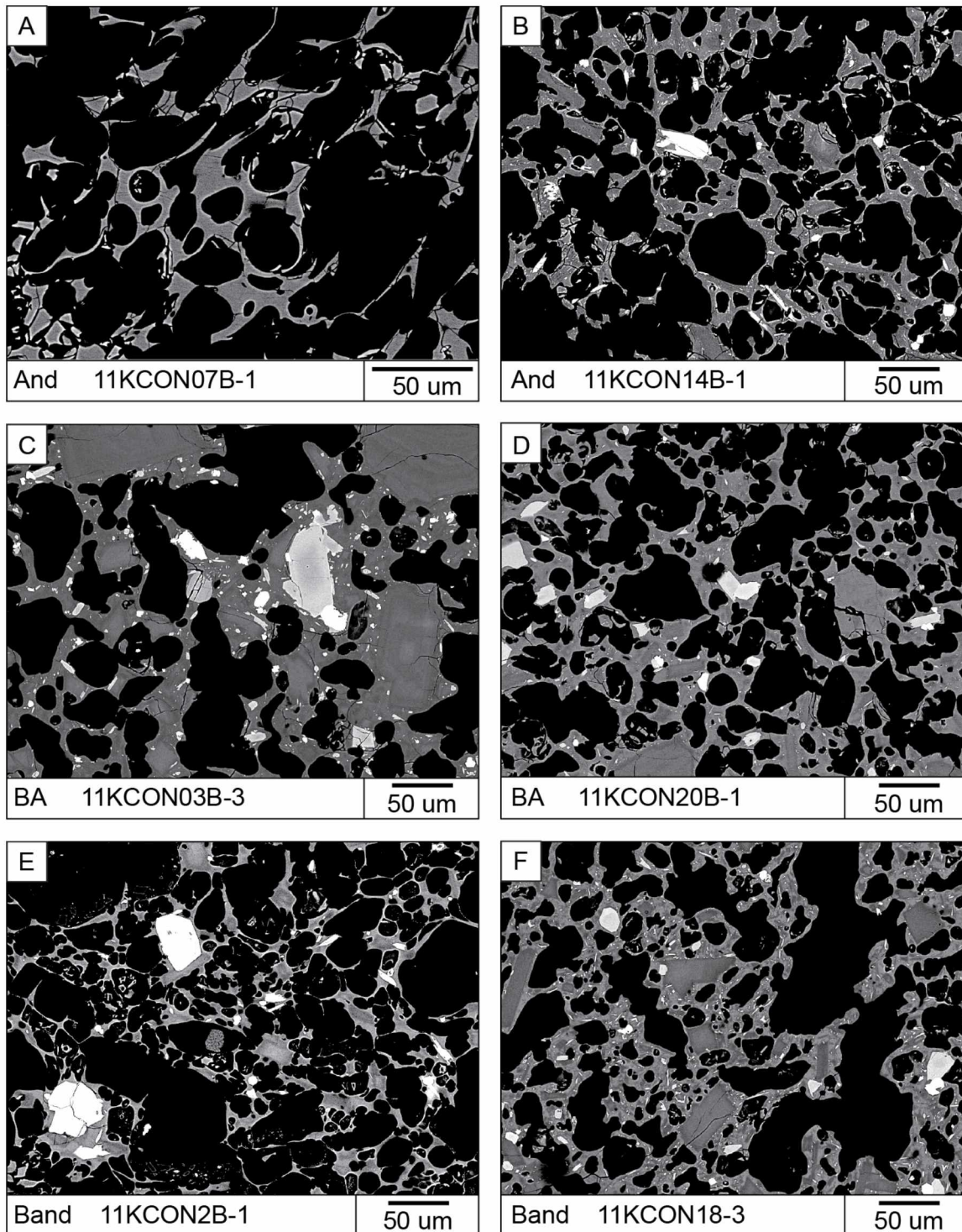
Figure 4.6: BSE images of andesite (row 1), basaltic andesite (row 2), and banded clasts (row 3). The image histograms were stretched to allow better viewing of the plagioclase microlites, therefore some clinopyroxene crystals might appear white similar to iron oxide crystals.
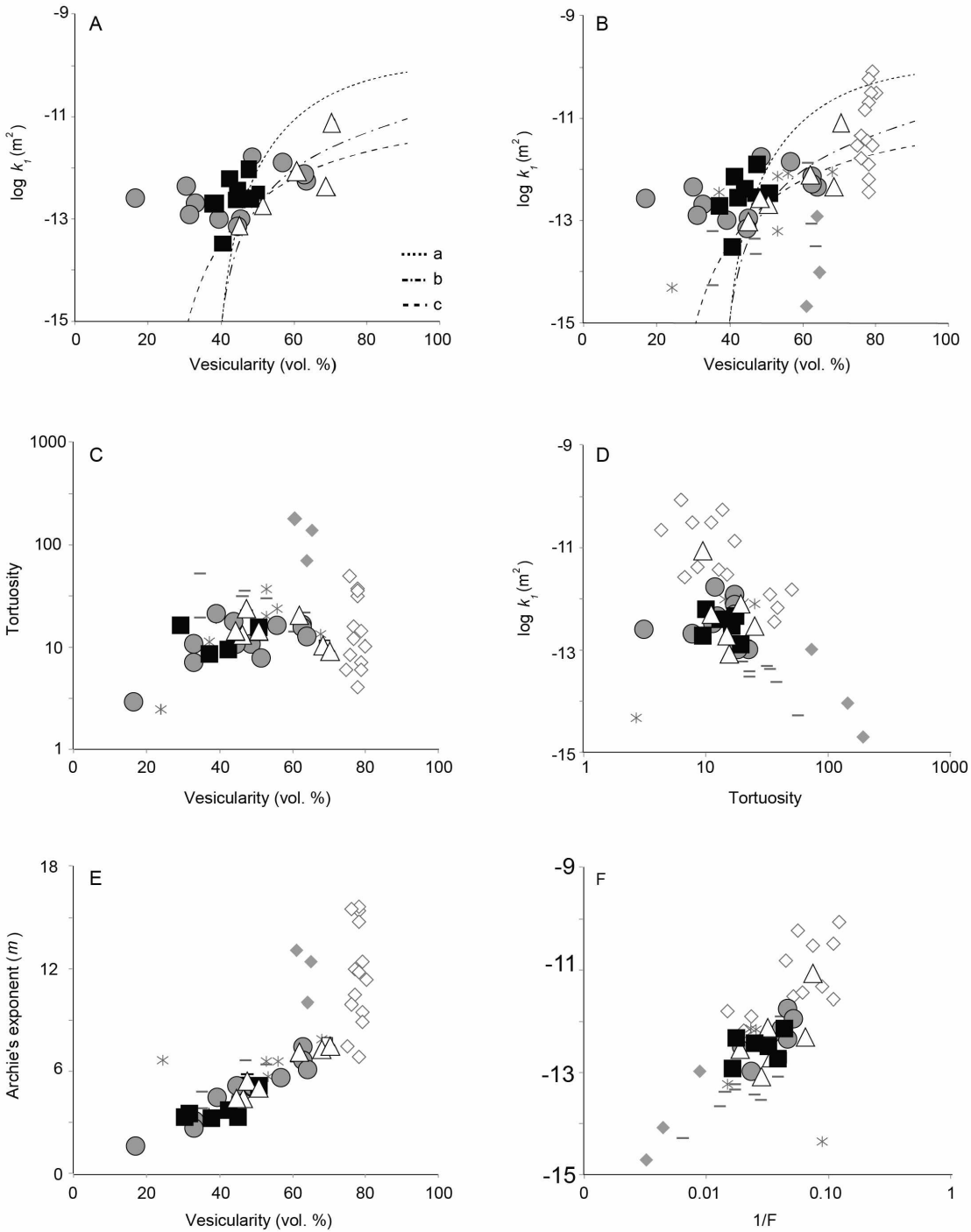
Figure 4.7: Relationships in bulk parameters within andesite (white triangles), basaltic andesite (black squares), and banded (gray circles) from the Kasatochi 2008 eruption products. (A) Log Darcian permeability (k_1) vs. connected porosity (Φ). (B) Log Darcian permeability vs. connected porosity compared with data from Wright et al. (2009), which includes the Tumalo Tuff tube pumice (white diamonds), Monte Pilato tube pumice (grey diamonds), Guagua Pichincha dacite bread crust interiors (black bars), and coarsely vesicular lava from Little and Big Glass Mountain (asterisks). (C) Tortuosity (τ) versus connected porosity. (D) Log Darcian permeability versus tortuosity. (E) Archie's exponent (m) versus connected porosity. (F) Log Darcian permeability versus $1/F$, with F being the formation factor. Error bars for connected porosity, permeability, and tortuosity are smaller than symbols. The data were fit using the Kozeny-Carman equation (Fig. 4.7A,B; trends a and b) and the fully penetrable spheres (FPS) model (Fig. 4.7A,B; trend c) (Carman, 1954; Sahimi, 1994).
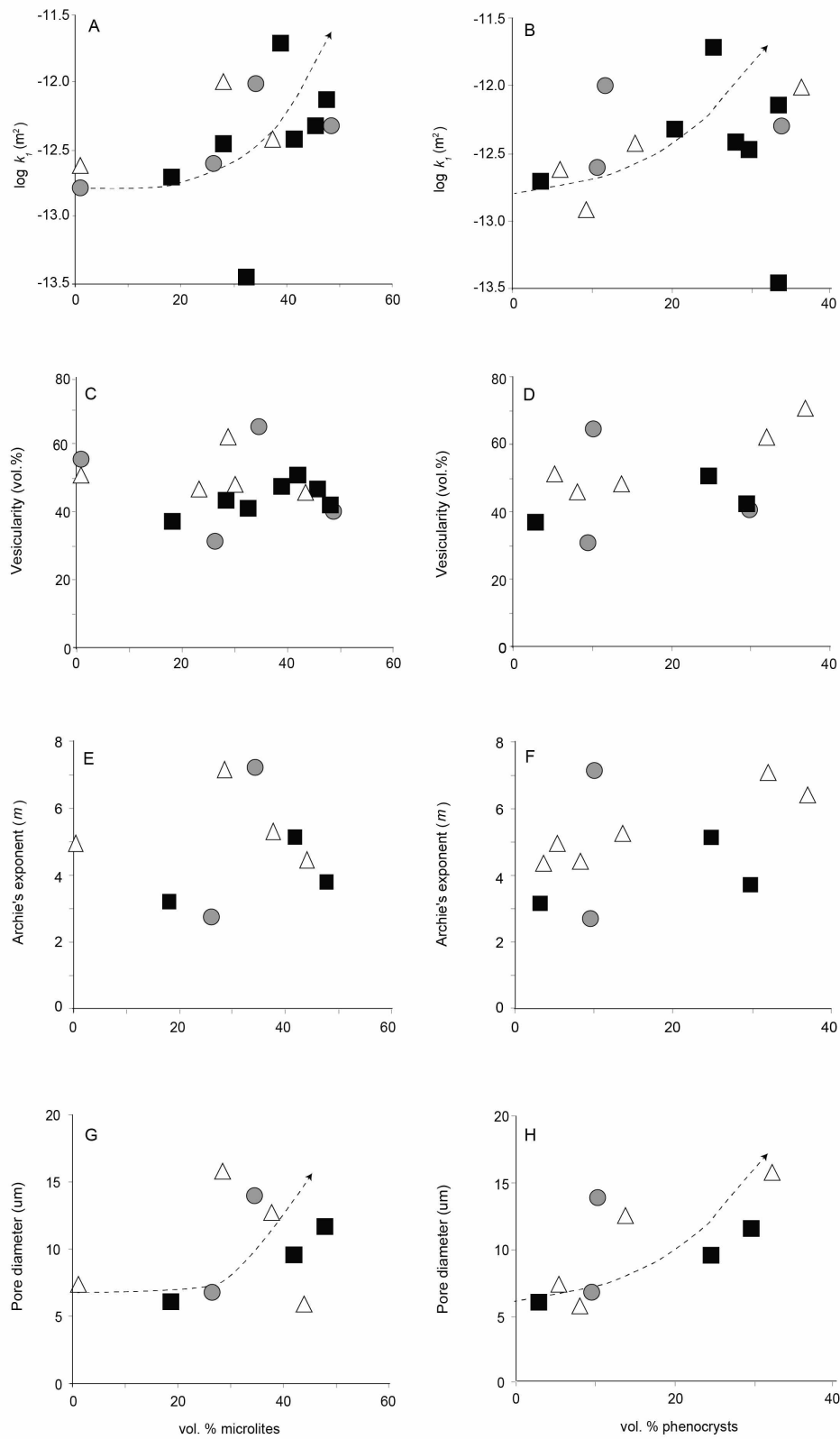
Figure 4.8: Microlite (left) and phenocryst (right) effects on permeability (A, B), vesicularity (C, D), Archie's exponent (E, F) and pore diameter (G, H).
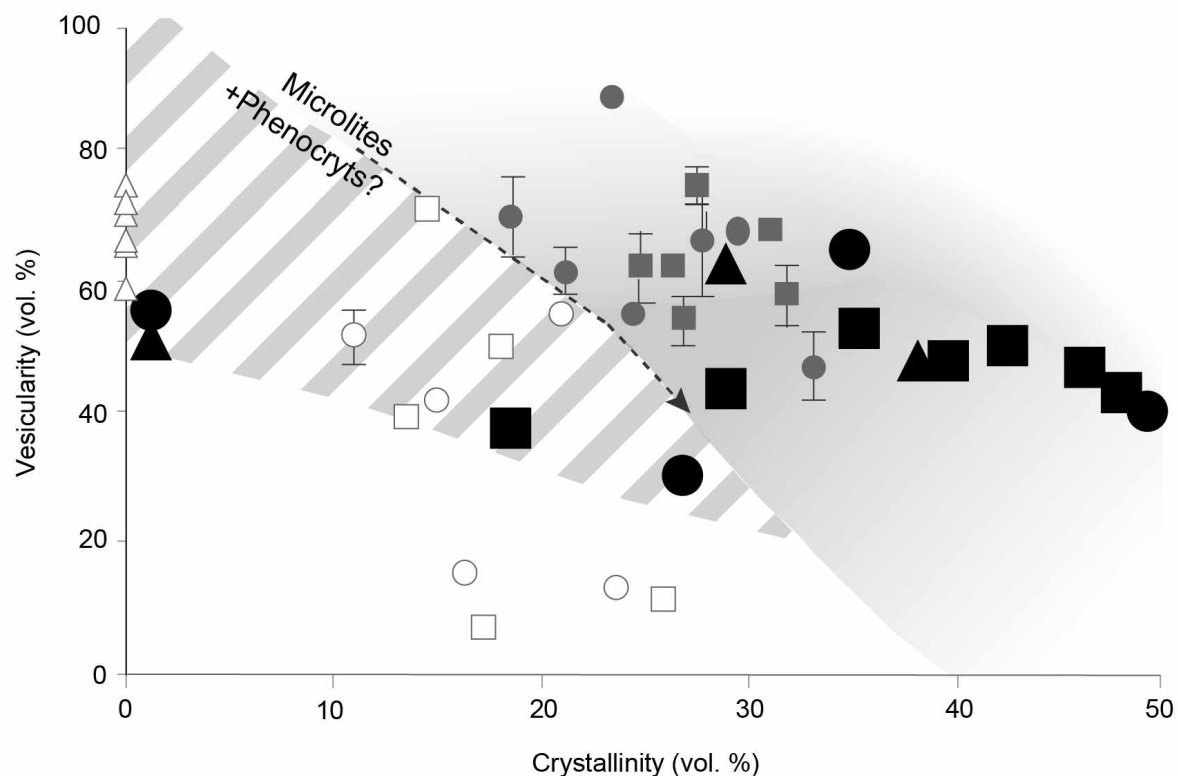
Figure 4.9. Vesicularity as a function of crystallinity modified after Lindoo et al. (2017). black symbols represent andesite (triangles), basaltic andesite (squares), and banded (circles) clasts measured in our study. The data are compared to impermeable crystal-free (white triangles) basaltic andesite decompression experiments of Lindoo et al. (2016) as well as permeable (gray fill) and impermeable (white fill) crystalline decompression experiments performed at decompression rates of 0.125 MPa s^{-1} (squares) and 0.083 MPa s^{-1} (circles) (Lindoo et al., 2017). The shaded gray region highlights the transition between impermeable-permeable fields, which are also denoted by a dark gray dashed line. The diagonal pattern represents the extension of the impermeable-permeable fields to lower vesicularities for a given crystal content.

4.9 Tables

Table 4.1: Samples used for permeability measurements

Sample	Layer[a]	SiO_2	Lithology	Latitude	Longitude
11KCON01	3	54.50	Banded	52.1727	175.5303
11KCON02	3	54.72	Banded	52.1727	175.5303
11KCON03	3	52.97	BA	52.1670	175.4923
11KCON06	3	59.73	Banded	52.1708	175.5303
11KCON07	2	59.23	Andesite	52.1749	175.5293
11KCON08	3	-	Banded	52.1727	175.5303
11KCON09	3	59.30	Andesite	52.1727	175.5303
11KCON10	3	52.15	BA	52.1727	175.5303
11KCON13	3	52.64	BA	52.1677	175.5299
11KCON14	2	59.77	Andesite	52.1749	175.5293
11KCON15	2	-	Banded	52.1749	175.5293
11KCON16	3	-	Banded	52.1672	175.5294
11KCON18	3	53.85	BA	52.1672	175.5294
11KCON19	2	-		52.1692	175.5304
11KCON20	2	55.38	BA	52.1692	175.5304
09KCNYE008A	-	52.02	BA	-	-
09KCNYE008B	-	52.82	Banded	-	-
09KCNYE008C	-	52.87	BA	-	-
09KCNYE005	-	54.99	Banded	-	-
08KCW002-1C	-	58.03	Andesite	-	-
09KCWES002	-	-	Banded	-	-

[a]Layers refer to "major units" denoted by Waythomas et al. (2010).

Table 4.2: Bulk parameter data from Kasatochi 2008 pyroclasts

Sample	$^{a}\Phi_{c}$ (%)	$^{b}\log k_1$ (m^2)	$^{b}\log k_2$ (m)	$^{c}\tau$	^{d}F	^{e}m	^{f}d (um)
Andesite							
07-1	50.8	-12.63(18)	-8.75(15)	14.47	28.48	4.9	7.3
07-2	44.8	-12.92(1)	-9.51(1)	15.16	33.85	4.4	5.7
07-4	46.2	-	-	13.08	28.31	4.3	-
14-2	47.6	-12.43(8)	-8.94(1)	24.94	52.39	5.3	12.5
02-1C	62.0	-12.00(2)	-8.34(12)	18.88	30.45	7.1	15.6
02-1C2	68.5	-12.01(11)	-8.45(4)	10.51	24.66	7.2	8.7
002C	70.4	-10.94(1)	-7.58(2)	9.28	13.21	7.4	46.9
Basaltic Andesite							
03-1	50.7	-12.43(1)	-8.39(3)	15.92	31.22	5.1	9.7
03-2	44.8	-12.37(1)	-8.34(3)	12.45	37.97	3.3	11.3
10-1	46.6	-12.33(7)	-8.90(5)	-	-	-	-
10-2	42.4	-12.14(3)	-8.37(10)	9.87	23.28	3.7	11.6
13-2	40.8	-13.46(1)	-9.45(4)	-	-	-	-
17-1	37.4	-12.71(4)	-9.05(2)	9.06	24.23	3.2	6.1
17-2	30.0	-12.34(6)	-8.80(7)	16.84	56.15	3.3	14.4
18-1	47.6	-11.72(38)	-8.34(47)	-	-	-	-
18-2	44.7	-12.42(9)	-8.87(11)	-	-	-	-
20-1	43.5	-12.46(28)	-8.81(5)	-	-	-	-
Banded							
01-1	55.1	-12.79(1)	-8.57(17)	-	-	-	-
01-2	40.6	-12.32(2)	-8.60(7)	-	-	-	-
02-1	31.0	-12.61(7)	-8.91(5)	7.51	24.24	2.7	6.9
02-2	30.7	-	-	11.05	35.65	3.0	-
02-3	60.3	-12.28(2)	-8.38(2)	12.87	21.34	6.1	9.5
06-1	59.7	-12.21(1)	-8.56(4)	17.45	29.23	6.6	12.0
06-2	31.3	-12.85(1)	-9.03(1)	18.91	60.42	3.5	8.2
08-2	49.7	-11.68(3)	-8.06(5)	11.51	21.46	4.9	18.9
15-1	40.5	-12.96(2)	-8.82(21)	21.61	53.36	4.4	6.9
15-2	17.3	-12.53(1)	-8.65(2)	3.05	17.63	1.6	6.5
16-1	42.5	-12.92(1)	-9.03(1)	18.04	42.45	4.4	6.4
16-2	42.0	-13.10(1)	-9.21(1)	-	-	-	-
19-2	58.7	-11.93(2)	-7.69(7)	11.25	19.17	5.6	13.4
20-2	46.1	-12.44(1)	-8.61(2)	23.31	50.56	5.1	12.2
005	64.9	-12.21(1)	-8.76(4)	15.41	15.34	7.4	13.9

^{a} Connected vesicularity. Error is approximately ± 1% of the listed value.
^{b} Darcian and inertial permeabilities, respectively.
^{c} Electrical tortuosity. A general error of ± 10% is assumed for all samples.
^{d} Formation factor calculated from tortuosity.
^{e} Archie's exponent.
^{f} Pore diameter.

Table 4.3: Microlite crystal textures from representative clasts of andesite, basaltic andesite and banded lithologies

Sample	Groundmass Φ^{ad} (vol.%)		Aspect ratio (i:l)[b]		N_A (mm^{-2})[c]	Phenocrysts Φ (vol.%)	Microlite textures present		
	Plag	Cpx	Plag	Cpx			Swallowtail	Hopper	Euhedral
Andesite									
07-1	≤1	≤1	-	-	-	5.3(0.5)	-	-	-
07-2	38.0(3)	5.8(2)	4:10	1:8	1.4E+05 (3.3E+04)	8.2(0.8)	x	x	x
07-4	23.4(3)	8.0(3)	3:10	1.3:3.6	8.7E+05 (5.5E+04)	3.5(0.3)	-	x	x
07-5	13.4(8)	3.2(1)	1.7:10	1:5.5	7.4E+04 (5.5E+04)	-	-	x	x
14-1	25.1(1)	5.2(1)	4:10	1:10	2.5E+04 (4.0E+03)	13.6(1.1)	-	-	x
Basaltic Andesite									
03-3	25.6(12)	16.4(14)	1.3:2	1.3:2		-			x
10-1	40.5(24)	5.2(1)	1.4:7	1.2:1.7	7.9E+04 (1.1E+04)	17.9(1.2)	-	-	x
10-2	37.7(8)	10.1(4)	1.5:8	1.5:7	6.0E+04 (4.7E+03)	29.5(1.7)	-	-	x
13-1	25.5(6)	7.1(3)	1.7:5.5	1.3:2	5.1E+04 (6.7E+03)	29.3(1.7)	-	x	x
17-1	≤1	≤1	-	-	-	3.0(0.3)	-	-	-
18-3	34.9(5)	4.2(1)	3.2:10	1.2:3.4	1.1E+05 (1.7E+04)	22.1(1.4)	-	x	x
20-1	23.9(8)	4.6(1)	1.3:8	1.3:3.2	3.2E+04 (2.7E+04)	26.2(1.6)	-	x	x
008A	25.0(3)	18.2(3)	1.6:3.2	1.4:2.3	1.1E+05 (6.5E+04)	-	-	-	x
Banded									
01-2	≤1	≤1	-	-	-	-	-	-	-
01-3	34.2(3)	14.5(9)	2.7:9	1.2:5.5	9.4E+04 (2.7E+03)	29.8(1.7)	-	x	x
02-1	21.2(7)	3.7(3)	1.3:8	1.3:10	1.1E+04 (2.8E+03)	9.4(0.9)	-	-	x
005	29.3(3)	5.3(2)	1.5:10	1.2:1.7	5.1E+04 (1.7E+04)	10.1(0.9)	-	-	x
008B	26.9	7.7	1.4:3.6	1.4:1.6	1.4E+04	-	-	-	x

[a] Microlite volume percent
[b] Intermediate: long axis
[c] Microlite area number density
[d] Fe-oxides are also present within the clasts at consistently ≤1 vol.%

Chapter 5 Conclusion

In this dissertation, experimental petrology was employed to constrain degassing mechanisms of mafic magmas. Comparison of this data to bulk parameters (vesicularity, permeability, tortuosity, and crystallinity) of natural pyroclasts has shed light on overall conditions affecting magma degassing. The first study (Chapter 2) focused on permeability development in crystal-free rhyolite, rhyodacite, K-phonolite, and basaltic andesite melts. The primary goal of the study was to investigate how melt composition affects permeability development. In crystal-poor systems, melts must attain vesicularities >63 vol.% in order to be permeable. Mafic magmas, such as basaltic andesite, do not record permeability development, due to vesiculation, because of low melt viscosity.

The second study (Chapter 3) of this thesis expands upon the results from Chapter 2. Decompression experiments developed permeability after the formation of approximately 20 vol.% microlites. The crystals specifically enhance permeability development by encouraging the development of long, finger-like bubbles. This led to the reduction of the percolation threshold due to the experimental magmas approaching the onset of yield strength. Particle-particle actions caused deformation of bubbles, enhanced coalescence, which then assisted in permeability development.

The results of Chapter 2 and Chapter 3 were referenced in the interpretation of findings from Chapter 4. Andesite and basaltic andesite pyroclasts from the 2008 eruption of Kasatochi volcano were quantitatively compared in an effort to understand transitions in eruption intensity. Vesicularity, permeability, electrical properties, and crystallinities were measured and related to understand degassing mechanisms of magmas with large ranges in crystallinity. These parameters varied as a function of crystal content within the magma. In general, Kasatochi products contained higher crystal contents than what were measured in experimental samples. This led the magma to cross another rheological threshold of random closest packing (RCP). This transition occurs ~54 vol.% crystals, depending on crystal aspect ratio. Two degassing regimes have been observed at this transition, gas-driven filter pressing and gas-fracture. Due to the fast ascent of magma, and small size of crystals, it was more likely that magma degassed through gas fracturing. This degassing mechanism caused the pulsatory nature of the Kasatochi explosive eruptions.

6 References

Archie, G. E., 1942, The electrical resistivity log as an aid in determining some reservoir characteristics, Transactions of the American Institute of Mining and Metallurgical Engineers, v.146, p. 54-62.

Bai, L., Baker, D.R., and Hill, R.J., 2010, Permeability of vesicular Stromboli basaltic glass: Lattice Boltzmann simulations and laboratory measurements: Journal of Geophysical Research, v. 115, no. B7, p. 1–16, doi: 10.1029/2009JB007047.

Bai, L., Baker, D.R., Polacci, M., and Hill, R.J., 2011, In-situ degassing study on crystal-bearing Stromboli basaltic magmas: Implications for Stromboli explosions: Geophysical Research Letters, v. 38, no. 17, p. 3–7, doi: 10.1029/2011GL048540.

Bernard, M., Zamora, M., Ge, Y., and Boudon, G., 2007, Transport properties of pyroclastic rocks from Montagne Pele´e volcano (Martinique , Lesser Antilles): v. 112, p. 1–16, doi: 10.1029/2006JB004385.

Blower, J., 2001, Factors controlling permeability–porosity relationships in magma: Bulletin of Volcanology, v. 63, p. 497–504, doi: 10.1007/s004450100172.

Bouvet de Maisonneuve, C., Bachmann, O., and Burgisser, A., 2009, Characterization of juvenile pyroclasts from the Kos Plateau Tuff (Aegean Arc): instights into the eruptive dynamics of a large rhyolitic eruption: Bulletin of Volcanology, v. 71, p. 643–658, doi: 10.1007/s00445-008-0250-x.

Burgisser, A., and Gardner, J.E., 2004, Experimental constraints on degassing and permeability in volcanic conduit flow: Bulletin of Volcanology, v. 67, p.42–56, doi: 10.1007/s00445-004-0359-5.

Cashman, K.V., and Giordano, G., 2014, Calderas and magma reservoirs: Journal of Volcanology and Geothermal Research, v. 288, p. 28–45. doi: 10.1016/j.jvolgeores.2014.09.007.

Castro, J.M., Cordonnier, B., Tuffen, H., Tobin, M.J., Puskar, L., Martin, M.C., and Bechtel, H.A., 2012a, The role of melt-fracture degassing in defusing explosive rhyolite eruptions at volcán Chaitén: Earth and Planetary Science Letters, v. 333, p. 63–69, doi:10.1016/j.epsl.2012.04.024.

Castro, J.M., Burgisser, A., Schipper, C.I., and Mancini, S., 2012b, Mechanisms of bubble coalescence in silicic magmas: Bulletin of Volcanology, v. 74, p. 2339–2352, doi: 10.1007/s00445-012-0666-1.

Degruyter, W., Burgisser, A., Bachmann, O., and Malaspinas, O., 2010, Synchrotron X-ray microtomography and lattice Boltzmann simulations of gas flow through volcanic pumice: Geosphere, v. 6, no. 5, p. 470-481, doi: 10.1130/GES00555.1.

Delaney, G. W., Hilton, J. E., and Cleary, P. W., 2011, Defining random loose packing for nonspherical grains: Physical Review E, v. 83, no. 5, p. 051305, doi: 10.1103/PhysRevE.83.051305.

Dixon, J. E., Stolper, E. M., and Holloway, J. R., 1995, An experimental study of water and carbon dioxide solubilities in mid-ocean ridge basaltic liquids. Part 1: Calibration and solubility models: Journal of Petrology, v. 36, p. 1607–1631.

Eichelberger, J.C., Carrigan, C.R., Westrich, H.R., and Price, R.H., 1986, Non-explosive silicic volcanism: Nature, v. 323, no. 6089, p. 598–602, doi: 10.1038/323598a0.

Gardner, J.E., Hilton, M., and Carroll, M.R., 1999, Experimental constraints on degassing of magma: isothermal bubble growth during continuous decompression from high pressure: Earth and Planetary Science Letters, v. 168, p. 201–218, doi:10.1016/ S0012-821X(99)00051-5.

Ghanbarian, B., Hunt, A.G., Ewing, R.P., and Sahimi, M., 2013, Tortuosity in Porous Media: A Critical Review: Soil Science Society of America Journal, v. 77, no. 5, p. 1461–1477, doi: 10.2136/sssaj2012.0435.

Giordano, D., Russell, J.K., and Dingwell, D.B., 2008, Viscosity of magmatic liquids: a model: Earth and Planetary Science Letters, v. 271, p. 123–134, doi: 10.1016/j.epsl. 2008.03.038.

Gonnermann, H.M., and Manga, M., 2007, The fluid mechanics inside a volcano: Annual Review of Fluid Mechanics, v. 39, p. 321–356, doi: 10.1146/annurev.fluid.39.050905. 110207.

Holtzman, R., Szulczewski, M. L., and Juanes, R., 2012, Capillary fracturing in granular media: Physical review letters, v. 108, no. 26, p. 264504, doi: 10.1103/PhysRevLett.108.264504.

Hoover, S.R., Cashman, K.V. and Manga, M., 2001, The yield strength of subliquidus basalts—experimental results: Journal of Volcanology and Geothermal Research, v. 107, no. 1, p. 1-18, doi: 10.1016/S0377-0273(00)00317-6.

Houghton, B.F., and Gonnermann, H.M., 2008, Basaltic explosive volcanism: Constraints from deposits and models: Chemie der Erde - Geochemistry, v. 68, no. 2, p. 117–140, doi: 10.1016/j.chemer.2008.04.002.

Iacono-Marziano, G., Schmidt, B.C., and Dolfi, D., 2007, Equilibrium and disequilibrium degassing of a phonolitic melt (Vesuvius AD 79 "white pumice") simulated by decompression experiments: Journal of Volcanology and Geothermal Research, v. 161, p. 151–164, doi: 10.1016/j.jvolgeores.2006.12.001.

Ihinger, P. D., Hervig, R. L., and McMillan, P.F., 1994, Analytical methods for volatiles in glasses: Reviews in Mineralogy and Geochemistry, v. 30, p. 67-121.

103

Jaupart, C., and Allègre, C. J., 1991, Gas content, eruption rate and instabilities of eruption
    regime in silicic volcanoes: Earth and Planetary Science Letters, v. 102, no. 3-4, p. 413-429,
    doi: 10.1016/0012-821X(91)90032-D.

Jaupart, C., 1996, Physical models of volcanic eruptions: Chemical Geology, v. 128, no. 95, p.
    217–227, doi: 10.1016/0009-2541(95)00175-1.

Katz, A.J., and Thompson, A.H., 1986, Quantitative prediction of permeability in porous rock:
    Physics Review, v. 34, no. 11, p. 8181-9179.

Kennedy, B.M., Wadsworth, F.B., Vasseur, J., Schipper, C.I., Jellinek, A.M., Aulock, F.W. Von,
    Hess, K., Russell, J.K., Lavallée, Y., Nichols, A.R.L., and Dingwell, D.B., 2016, Surface
    tension driven processes densify and retain permeability in magma and lava: Earth and
    Planetary Science Letters, v. 433, p. 116–124, doi: 10.1016/j.epsl.2015.10.031.

Kerr, R.C. and Lister, J.R., 1991, The effects of shape on crystal settling and on the rheology of
    249 250 magmas: The Journal of Geology, v. 99, no. 3, p.457-467, doi: 10.1086/629506.

Khitarov, N.I., Lebedev, Ye.B., Dorfman, A.M., and Bagdasarov, N.Sh., 1979, Effects of
    temperature, pressure, and volatiles on the surface tension of molten basalt: Geochemistry
    International, v. 16, p. 78–86.

Klug, C., and Cashman, K.V., 1996, Permeability development in vesiculating magmas:
    implications for fragmentation: Bulletin of Volcanology, v. 58, no. 2, p. 87-100.

Klug, C., Cashman, K. V., and Bacon, C.R., 2002, Structure and physical characteristics of
    pumice from the climactic eruption of Mount Mazama (Crater Lake), Oregon: Bulletin of
    Volcanology, no. 64, p. 486–501, doi: 10.1007/s00445-002-0230-5.

Kobayashi, T., Namiki, A., and Sumita, I., 2010, Excitation of airwaves caused by bubble
bursting in a cylindrical conduit: Experiments and a model, Journal of Geophysical
Research: Solid Earth, v. 115, n. 10. doi: 10.1029/2009JB006828.

Krotkov, N. A., Schoeberl, M. R., Morris, G. A., Carn, S., and Yang, K., 2010, Dispersion and
lifetime of the SO_2 cloud from the August 2008 Kasatochi eruption: Journal of Geophysical
Research: Atmospheres, v. 115, n. D2, doi: 10.1029/2010JD013984.

Lange, R. A., and Carmichael, I. S., 1987, Densities of Na_2O-K_2O-MgO-MgO-FeO-Fe_2O_3-
Al_2O_3-TiO_2-SiO_2 liquids: New measurements and derived partial molar properties:
Geochimica et Cosmochimica Acta, v. 51, p. 2931-2946.

Larsen, J.F., 2006, Rhyodacite magma storage conditions prior to the 3430 yBP caldera-forming
eruption of Aniakchak volcano, Alaska: Contributions to Mineralology and Petrology, v.
152, p. 523–540, doi: 10.1007/s00410-006-0121-4.

Larsen, J.F., and Gardner, J.E., 2000, Experimental constraints on bubble interactions in rhyolite
melts: implications for vesicle size distributions: Earth and Planetary Science Letters, v.
180, p. 201–214, doi: 10.1016/S0012-821X(00)00166-7.

Le Pennec, J.L., Hermitte, D., Dana, I., Pezard, P., Coulon, C., Cochemé, J.J., Mulyadi, E.,
Ollagnier, F., and Revest, C., 2001, Electrical conductivity and pore-space topology of
Merapi lavas: Implications for the degassing of porphyritic andesite magmas: Geophysical
Research Letters, v. 28, no. 22, p. 4283–4286, doi: 10.1029/2001GL013401.

Lindoo, A., Larsen, J. F., Cashman, K. V., Dunn, A. L., and Neill, O. K., 2016, An experimental
study of permeability development as a function of crystal-free melt viscosity: Earth and
Planetary Science Letters, v. 435, p. 45-54, doi: 10.1016/j.epsl.2015.11.035.

Lindoo, A., Larsen, J.F., Cashman, K.V., and Oppenheimer, J., 2017, Crystal controls on
permeability development and degassing in basaltic andesite magma: Geology,
doi: 10.1130/G39157.1.

Liu, E. J., Cashman, K. V., and Rust, A. C., 2015, Optimising shape analysis to quantify volcanic ash morphology: GeoResJ, v. 8, p.14-30. doi:10.1016/j.grj.2015.09.001.

Mader, H.M., Llewellin, E.W., and Mueller, S.P., 2013, The rheology of two-phase magmas: A review and analysis: Journal of Volcanology and Geothermal Research, v. 257, p. 135–158, doi: 10.1016/j.jvolgeores.2013.02.014.

Mangan, M., and Sisson, T., 2000, Delayed, disequilibrium degassing in rhyolite magma: decompression experiments and implications for explosive volcanism: Earth and Planetary Science Letters, v. 183, p. 441–455, doi: 10.1016/S0012- 821X(00)00299-5.

Martel, C., and Iacono-Marziano, G., 2015, Timescales of bubble coalescence, outgassing, and foam collapse in decompressed rhyolitic melts: Earth and Planetary Science Letters, v. 412, p. 173–185. doi: 10.1016/j.epsl.2014.12.010.

Marxer, H., Bellucci, P., and Nowak, M., 2015, Degassing of H_2O in a phonolitic melt: A closer look at decompression experiments: Journal of Volcanology and Geothermal Research, v. 297, no. April, p. 109–124, doi: 10.1016/j.jvolgeores.2014.11.017.

Mongrain, J., Larsen, J.F., and King, P.L., 2008, Rapid water exsolution, degassing, and bubble collapse observed experimentally in K-phonolite melts: Journal of Volcanology and Geothermal Research, v. 173, no. 3–4, p. 178–184, doi: 10.1016/j.jvolgeores.2008.01.026.

Mongrain, J., and Larsen, J.F., 2009, Spatial point pattern analysis applied to bubble nucleation in silicate melts: Computers and Geosciences, v. 35, no. 9, p. 1917–1924, doi: 10.1016/j.cageo.2009.01.008.

Morgan, D.J., and Jerram, D.A., 2006, On estimating crystal shape for crystal size distribution analysis On estimating crystal shape for crystal size distribution analysis: no. April, doi: 10.1016/j.jvolgeores.2005.09.016.

Moore, G., Vennemann, T., and Carmichael, I.S.E., 1998, An empirical model for the solubility of H_2O in magmas to 3 kilobars: American Mineralogist, v. 83, p. 36–42.

Mueller, S., Melnik, O., and Spieler, O., 2005, Permeability and degassing of dome lavas undergoing rapid decompression : An experimental determination: p. 526–538, doi: 10.1007/s00445-004-0392-4.

Mueller, S., Scheu, B., Spieler, O., and Dingwell, D.B., 2008, Permeability control on magma fragmentation: Geology, v. 36, no. 5, p. 399–402, doi: 10.1130/G24605A.1.

Mueller, S., Llewellin, E.W., and Mader, H.M., 2009, The Rheology of suspensions of solid particles: Proceedings of the Royal Society A: Mathematical, Physical and Engineering Sciences, p. 1–27, doi: 10.1007/BF01432034.

Mueller, S., Llewellin, E.W., and Mader, H.M., 2011, The effect of particle shape on suspension viscosity and implications for magmatic flows: Geophysical Research Letters, v. 38, n. 13, doi: 10.1029/2011GL047167.

Murase, T., and McBirney, A.R., 1973, Properties of some common igneous rocks and their melts at high temperatures: GSA Bulletin, v. 84, p. 3563–3592, doi: 10.1130/0016-7606(1973)84<3563:POSCIR>2.0.CO;2.

Nakamura, M., Otaki, K., and Takeuchi, S., 2008, Permeability and pore-connectivity variation of pumices from a single pyroclastic flow eruption: implications for partial fragmentation: Journal of Volcanology and Geothermal Research, v. 176, p. 302–314. doi: 10.1016/j.jvolgeores.2008.04.011.

Namiki, A., and Manga, M., 2008, Transition between fragmentation and permeable outgassing of low viscosity magmas: Journal of Volcanology and Geothermal Research, v. 169, no. 1–2, p. 48–60, doi: 10.1016/j.jvolgeores.2007.07.020.

Namiki, A., and Kagoshima, T., 2014, Intermittent and efficient outgassing by the upward propagation of film ruptures in a bubbly magma: Journal of Geophysical Research, v. 119, p. 919–935, doi: 10.1002/2013JB010576.

Neill, O.K., 2013, Petrologic and geochemical tracers of magmatic movement in volcanic arc systems: case studies from the Aleutian Islands and Kamchatka, Russia: University of Alaska Fairbanks Ph.D., p. 188.

Newman, S., Stolper, E. M., and Epstein, S., 1986, Measurement of water in rhyolitic glasses-calibration of an infrared spectroscopic technique: American Mineralogist, v. 71, p. 1527-41.

Nguyen, C. T., Gonnermann, H. M., Chen, Y., Huber, C., Maiorano, A. A., Gouldstone, A., and Dufek, J., 2013, Film drainage and the lifetime of bubbles: Geochemistry, Geophysics, Geosystems, v. 14, no. 9, p. 3616-3631. doi: 10.1002/ggge.20198.

Nichols, A. R. L., and Wysoczanski, R. J., 2007, Using μ-FTIR spectroscopy to measure volatile contents in small and unexposed inclusions hosted in olivine crystals: Chemical Geology, v. 242, p. 371–384, doi: 10.1016/j.chemgeo.2007.04.007.

Ohlhorst, S., Behrens, H., and Holtz, F.,2001, Compositional dependence of molar absorptivities of nea-infrared OH- and H_2O bands in rhyolitic to basaltic glasses: Chemical Geology, v. 174, p. 5-20. doi: 10.1016/S0009-2541(00)00303-X.

Okumura, S., and Nakashima, S., 2005, Molar absorptivities of OH and H_2O in rhyolitic glass at room temperature and at 400 600° C: American Mineralogist, v. 90, no. 2-3, p. 441-447, doi: 10.2138/am.2005.1740.

Okumura, S., Nakamura, M., Takeuchi, S., Tsuchiyama, A., Nakano, T., and Uesugi, K., 2009, Magma deformation may induce non-explosive volcanism via degassing through bubble networks: Earth and Planetary Science Letters, v. 281, no. 3–4, p. 267–274, doi: 10.1016/j.epsl.2009.02.036.

Okumura, S., Nakamura, M., Nakano, T., Uesugi, K., and Tsuchiyama, A., 2012, Experimental constraints on permeable gas transport in crystalline silicic magmas: Contributions to Mineralogy and Petrology, v. 164, p. 493–504, doi: 10.1007/s00410-012-0750-8.

Oppenheimer, J., Rust, A.C., Cashman, K. V., and Sandnes, B., 2015, Gas migration regimes and outgassing in particle-rich suspensions: Frontiers in Physics, v. 3, no. August, p. 1–13, doi: 10.3389/fphy.2015.00060.

Parmigiani, A., Faroughi, S., Huber, C., Bachmann, O., and Su, Y., 2016, Bubble accumulation and its role in the evolution of magma reservoirs in the upper crust: Nature, v.532, doi: 10.1038/nature17401.

Philpotts, A.R., 1998, Nature of a flood-basalt-magma reservoir based on the compositional variation in a single flood-basalt flow and its feeder dike in the Mesozoic Hartford Basin, Connecticut: Contributions to mineralogy and petrology, v.133, no. 1-2, p. 69-82, doi: 10.1007/s004100050438.

Picard, D., Arbaret, L., Pichavant, M., Champallier, R., and Launeau, P., 2013, The rheological transition in plagioclase-bearing magmas: Journal of Geophysical Research: Solid Earth, v.118, no. 4, p. 1363-1377, doi: 10.1002/jgrb.50091.

Pioli, L., Erlund, E., Johnson, E., Cashman, K., Wallace, P., Rosi, M., and Delgado Granados, H., 2008, Explosive dynamics of violent Strombolian eruptions: The eruption of Parícutin Volcano 1943–1952 (Mexico): Earth and Planetary Science Letters, v. 271, no. 1–4, p. 359–368, doi: 10.1016/j.epsl.2008.04.026.

Pioli, L., Azzopardi, B.J., and Cashman, K. V., 2009, Controls on the explosivity of scoria cone eruptions: Magma segregation at conduit junctions: Journal of Volcanology and Geothermal Research, v. 186, no. 3–4, p. 407–415, doi: 10.1016/j.jvolgeores.2009.07.014.

Pistone, M., Arzilli, F., Dobson, K.J., Cordonnier, B., Reusser, E., Ulmer, P., Marone, F., Whittington, A.G., Mancini, L., Fife, J.L., and Blundy, J.D., 2015, Gas-driven filter pressing in magmas: Insights into in-situ melt segregation from crystal mushes: Geology, v. 43, no. 8, p. 699–702, doi: 10.1130/G36766.1.

Polacci, M., Baker, D.R., Bai, L., and Mancini, L., 2008, Large vesicles record pathways of degassing at basaltic volcanoes: Bulletin of Volcanology, v. 70, no. 9, p. 1023–1029, doi: 10.1007/s00445-007-0184-8.

Polacci, M., Baker, D.R., Bai, L., Mancini, L., Favretto, S., and Hill, R.J., 2009, Vesiculation in magmas from Stromboli and implications for normal Strombolian activity and paroxysmal explosions in basaltic systems. Journal of Geophysical Research: Solid Earth, v. 114, n. B1, doi: 10.1029/2008JB005672.

Polacci, M., Baker, D.R., La Rue, A., Mancini, L., and Allard, P., 2012, Degassing behaviour of vesiculated basaltic magmas: an example from Ambrym volcano, Vanuatu Arc, Journal of volcanology and geothermal research, v.233, p.55-64, doi: 10.1016/j.volgeores.2012.04.019.

Proussevitch, A.A., Sahagian, D.L., and Anderson, A.T., 1993, Dynamics of diffusive bubble growth in magmas: Isothermal case: Journal of Geophysical Research, v. 98.

Rader, E.L., and Larsen, J.F., 2013, Experimental phase relations of a low MgO Aleutian basaltic andesite at $XH_2O \leq 0.7 - 1$: , p. 1593–1611, doi: 10.1007/s00410-013-0944-8.

Ruppert, N. A., Prejean, S., and Hansen, R. A., 2011, Seismic swarm associated with the 2008 eruption of Kasatochi Volcano, Alaska: Earthquake locations and source parameters: Journal of Geophysical Research: Solid Earth, v. 116, n. B2, doi: 10.1029/2010JB007435.

Rust, A.C., and Cashman, K. V, 2004, Permeability of vesicular silicic magma : inertial and hysteresis effects: v. 228, p. 93–107, doi: 10.1016/j.epsl.2004.09.025.

Rust, A. C., and Cashman, K. V., 2011, Permeability controls on expansion and size distributions of pyroclasts: Journal of Geophysical Research, v. 116, no. November, p. 1–17, doi: 10.1029/2011JB008494.

Ruth, D., and Ma, H., 1992, On the derivation of the Forchheimer equation by means of the averaging theorem: Transport in Porous Media, v. 7, no. 3, p. 255-264.

Saar, M.O., and Manga, M., 1999, Permeability-porosity relationship in vesicular basalts: Geophysical Research Letters, v. 26, no. 1, p. 111–114, doi: 10.1029/1998GL900256.

Saar, M.O., Manga, M., Cashman, K.V., and Fremouw, S., 2001, Numerical models of the onset of yield strength in crystal-melt suspensions, Earth and Planetary Science Letters, v.187, no. 3, p.367-379, doi: 10.1016/S0012-821X(01)00289-8.

Sable, J.E., Houghton, B.F., Wilson, C.J.N., and Carey, R.J., 2009, Eruption mechanisms during the climax of the Tarawera 1886 basaltic Plinian eruption inferred from microtextural characteristics-of the deposits: Special Publications of IAVCEI, no. 2, p. 129–154.

Sahimi, M., 1994, Long-range correlated percolation and flow and transport in heterogeneous porous media, Journal of Physicas I France, v. 4, p. 1263.

Shea, T., Gurioli, L., Larsen, J.F., Houghton, B.F., Hammer, J.E., and Cashman, K.V., 2010a, Linking experimental and natural vesicle textures in Vesuvius 79AD white pumice: Journal of Volcanology and Geothermal Research, v. 192, p. 69–84, doi: 10.1016/j.jvolgeores.2010.02.013.

Shea, T., Houghton, B.F., Gurioli, L., Cashman, K.V., Hammer, J.E., and Hobden, B.J., 2010b, Textural studies of vesicles in volcanic rocks: an integrated methodology: Journal of Volcanology and Geothermal Research, v. 190, p. 271–289, doi: 10.1016/j.jvolgeores.2009.12.003.

Sisson, T.W., and Bacon, C.R., 1999, Gas-driven filter pressing in magmas: Geology, v. 27, p. 613–616.

Sparks, R.S.J., 1978, The dynamics of bubble formation and growth in magmas: A review and analysis: Journal of Volcanology and Geothermal Research, v. 3, no. 1–2, p. 1–37, doi: 10.1016/0377-0273(78)90002-1.

Spina, L., Cimarelli, C., Scheu, B., Genova, D. Di, Dingwell, D.B., Di Genova, D., and Dingwell, D.B., 2016, On the slow decompressive response of volatile- and crystal-bearing magmas: An analogue experimental investigation: Earth and Planetary Science Letters, v. 433, no. April, p. 44–53, doi: 10.1016/j.epsl.2015.10.029.

Stolper, E., 1982, The speciation of water in silicate melts: Geochimica et Cosmochimica Acta, v. 46, p. 2609–2620.

Szramek, L., Gardner, J.E., and Larsen, J., 2006, Degassing and microlite crystallization of basaltic andesite magma erupting at Arenal Volcano, Costa Rica: Journal of Volcanology and Geothermal Research, v. 157, p. 182–201. doi: 10.1016/j.jvolgeores.2006.03.039.

Szramek, L., Gardner, J.E., and Hort, M., 2010, Cooling-induced crystallization of microlite crystals in two basaltic pumice clasts: American Mineralogist, v. 95, p. 503–509, doi: 10.2138/am.2010.3270.

Takeuchi, S., Nakashima, S., and Tomiya, A., 2008, Permeability measurements of natural and experimental volcanic materials with a simple permeameter: toward an understanding of magmatic degassing processes: Journal of Volcanolgy and Geothermal Research, v. 177, p. 329–339, doi: 10.1016/j.jvolgeores.2008.05.010.

Takeuchi, S., Tomiya, A., and Shinohara, H., 2009, Degassing conditions for permeable silicic magmas: Implications from decompression experiments with constant rates: Earth and Planetary Science Letters, v. 283, no. 1–4, p. 101–110, doi: 10.1016/j.epsl.2009.04.001.

Tamic, N., Behrens, H., and Holtz, F., 2001, The solubility of H_2O and CO_2 in rhyolitic melts in equilibrium with a mixed CO_2–H_2O fluid phase: Chemical Geology, v. 174, p. 333-347, doi: 10.1016/S0009-2541(00)00324-7.

Toramaru, A., 1988, Formation of propagation pattern in two-phase flow systems with application to volcanic eruptions: Journal of Geophysics, v. 95, p. 613–623.

Van der Plas, L., and Tobi, A.C., 1965, A chart for judging the reliability of point counting results: American Journal of Science, v. 263, no. 1, p. 87-90.

Vinkler, A.P., Cashman, K., Giordano, G., and Groppelli, G., 2012. Evolution of the mafic Villa Senni caldera-forming eruption at Colli Albani volcano, Italy, indicated by textural analysis of juvenile fragments: Journal of Volcanological and Geothermal Research, v. 235, p. 37–54, doi: 10.1016/j.jvolgeores.2012.03.006.

Underwood, E.E., 1970, Quantitative Stereology: Addison-Wesley, Reading, Massachusetts.

Walsh, J.B., and Brace, W.F., 1984. The effect of pressure on porosity and the transport properties of rock: Journal of Geophysical Research, v. 89, no. B11, p. 9425–9431.

Walsh, S.D., and Saar, M.O., 2008, Magma yield stress and permeability: Insights from
multiphase percolation theory: Journal of Volcanology and Geothermal Research, v.177,
no.4, p.1011-1019, doi: 10.1016/j.jvolgeores.2008.07.009.

Waythomas, C. F., Scott, W. E., Prejean, S. G., Schneider, D. J., Izbekov, P., and Nye, C. J.,
2010, The 7–8 August 2008 eruption of Kasatochi Volcano, central Aleutian Islands,
Alaska: Journal of Geophysical Research: Solid Earth, v. 115, n. B12, doi:
10.1029/2010JB007437.

Westrich, H.R., and Eichelberger, J.C., 1994, Gas transport and bubble collapse in rhyolitic
magma: an experimental approach: Bulletin of Volcanology, v. 56, p. 447–458, doi:
10.1007/BF00302826.

Wong, L.J., and Larsen, J.F., 2009, The Middle Scoria sequence: a Holocene violent
strombolian, subplinian and phreatomagmatic eruption of Okmok volcano, Alaska: Bulletin
of Volcanology, v. 72, p. 17–31, doi: 10.1007/s00445-009-0301-y.

Wright, H., Roberts, J.J., and Cashman, K.V., 2006, Permeability of anisotropic tube pumice:
model calculations and measurements: Geophysical research letters, v. 33, n. 17, doi:
10.1029/2006GL027224.

Wright, H. M., Cashman, K. V., Rosi, M., and Cioni, R., 2007, Breadcrust bombs as indicators
of Vulcanian eruption dynamics at Guagua Pichincha volcano, Ecuador: Bulletin of
Volcanology, v. 69, n. 3, p. 281-300, doi: 10.1007/s00445-006-0073-6.

Wright, H.M.N., Cashman, K.V., Gottesfeld, E.H., and Roberts, J.J., 2009, Pore structure of
volcanic clasts: measurements of permeability and electrical conductivity: Earth and
Planetary Science Letters, v. 280, p. 93–104, doi: 10.1016/j.epsl.2009.01.023.

Wright, H.M., Cashman, K.V., Mothes, P.A., Hall, M.L., Ruiz, A.G., and Le Pennec, J.L., 2012,
Estimating rates of decompression from textures of erupted ash particles produced by 1999–
2006 eruptions of Tungurahua volcano, Ecuador: Geology, v. 40, p. 619–622, doi:
10.1130/G32948.1.

Wysoczanski, R. J., and Tani, K., 2006, Spectroscopic FTIR imaging of water species in silicic
volcanic glasses and melt inclusions: an example from the Izu-Bonin arc: Journal of
Volcanology and Geothermal Research. v. 156, p. 302–314, doi:
10.1016/j.jvolgeores.2005.04.021.

Zhang, Y., 1999, H_2O in rhyolitic glasses and melts: measurement, speciation, solubility, and
diffusion, Reviews of Geophysics, v. 37, n. 4, p. 493-516. doi: 10.1029/1999RG900012.